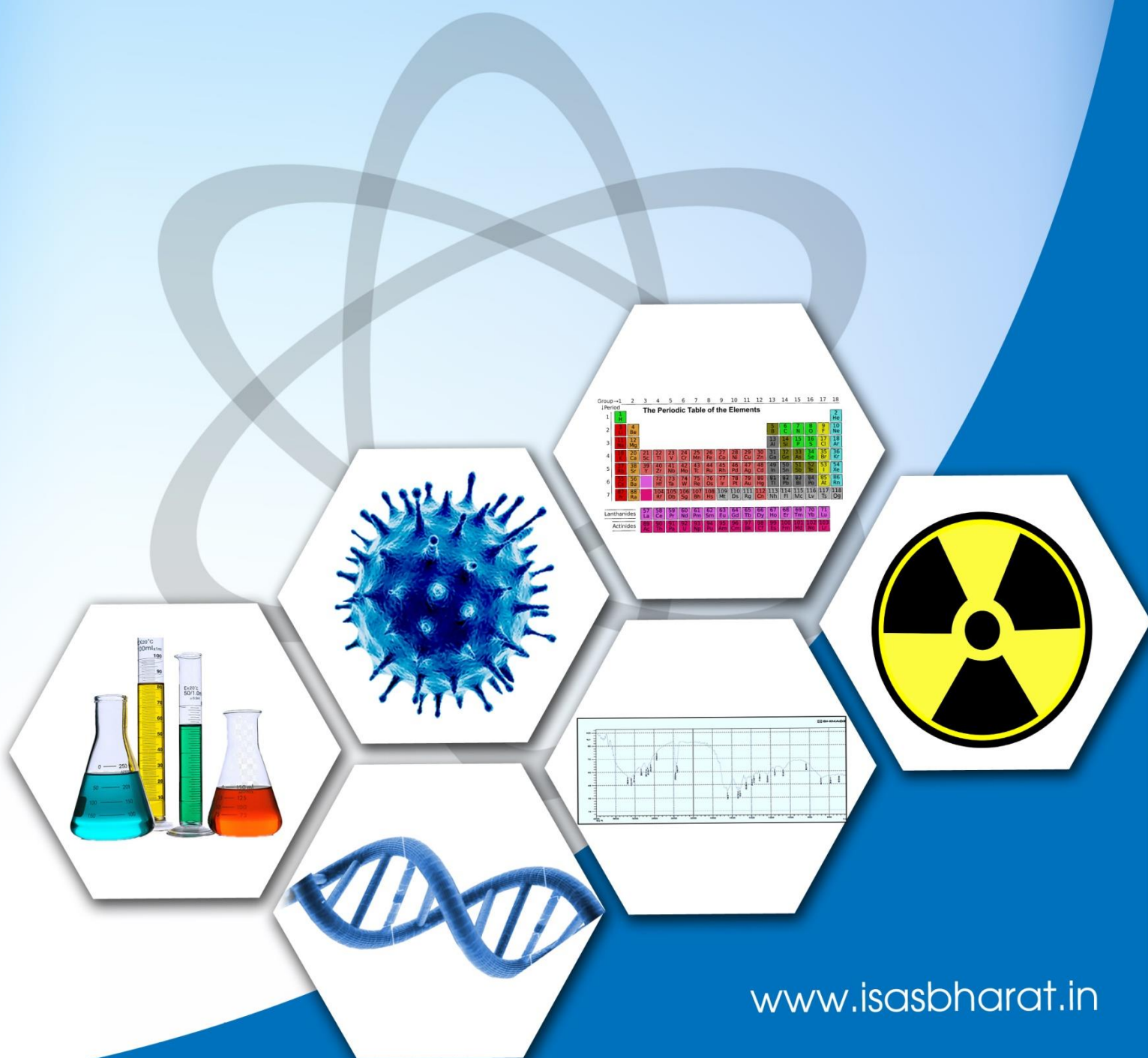




ISSN: 2583-5459
Volume 2 Issue 4
April, 2024

Journal of ISAS

An open access peer reviewed quarterly e-journal by
Indian Society of Analytical Scientists





Journal of ISAS

An open access peer reviewed quarterly e-journal published by Indian Society of Analytical Scientists

Published by: Indian Society of Analytical Scientists (ISAS)

Address: C/o REDS, BARC, Mumbai 400085

Email: isasjournal@isasbharat.in

President ISAS: Dr. Raghaw Saran

J. ISAS

Editorial Board

Editor in Chief

Dr. Nilima Rajurkar, Pune

Members

Dr. Vijayalaxmi C. Adya, Mumbai

Dr. A. K. Basu, Pune

Dr. Vinay Bhandari, Pune

Dr. Avinash Bharati, Nagpur

Dr. Anu Gopinath, Kochi

Dr. Ravin Jugade, Nagpur

Dr. Padmaja S. Vadodara

Dr. Pradeep Kumar, Mumbai

Dr. Prakash Samnani, Vadodara

Dr. Sridhar T. M , Chennai

Dr. S. K. Yadav, Vadodara

Dr. A. N. Garg, New Delhi

Advisory Board

Chairman

Dr. Raghaw Saran, Nagpur

Members

Dr. V. Sivanandan Achari, Kochi

Dr. V. Balaram, Hyderabad

Dr. J. Manjanna, Belgavi

Dr. V. R.Nair, Kollam

Dr. Amrit Prakash, Mumbai

Dr. S. Sriman Narayanan, Vellur

Dr. Shivaramu Prasanna, Bengaluru

Dr. K.P. Vijayalakshmi, Trivandrum

Dr. Mohammed Yusuff K.K., Kochi

Dr. Rajeev Raghavan, Trivandrum

Instruction to Authors

- The Manuscript should be typed in **MS word** (times new roman) with **1.5 spacings** and **font size 12**
- The **title** of the paper should be clear and concise(**font size 14 and bold**), the first letter of each noun and adjective in the title must be in capital letter. It will be followed by names of authors(initials followed by surname) with their affiliation (**font size 12**)
- Corresponding author should be indicated by * with email ID
- The text should be divided into following sections:
 - **Abstract : up to 300 words**
 - **Key words: 5-6**
 - **Introduction**
 - **Experimental**
 - **Results and Discussion**
 - **Conclusions**
 - **Acknowledgement**
- Figures and Tables should be before references with a caption **Figures:** Followed by **Tables:**
- **References**
 - Divisions within the section should be indicated as subheadings
 - The figures and tables should be numbered with Roman numerals and must be mentioned in the text at appropriate places
 - Standard abbreviations for technical terms and journals should be used
 - All constants should be expressed in **SI units**
 - References should be numbered consecutively and should appear in the text as superscript at appropriate places.
 - References should be in following pattern
 - For research paper:**
Authors' initials and surname, Journal abbreviation, Volume, Page, Year.
 - For book:**
Authors' initials and surname, Book name, Publisher, Place, Year.
 - For proceedings:**
Authors' initials and surname Proceedings' of the conference name, place, Page, Month and Year.
- The paper is to be submitted in word file and PDF file to isasjournal@isasbharat.in
- After getting the acceptance of the paper, authors have to submit **signed copyright form and undertaking** before publishing the article



Indian Society of Analytical Scientists.



Editorial

Welcome to the 8th issue of the Journal of Indian Society of Analytical Scientists (J.ISAS), which is quarterly open access e-journal with ISSN and Doi number. In this issue, we delve into cutting-edge research that promises to transform the landscape of environmental sustainability and we are proud to present a diverse range of manuscripts that highlight the innovative approaches being adopted in the field of analytical science to tackle pressing environmental challenges.

Waste water management is crucial for maintaining environmental health, as it prevents pollutants from entering ecosystems. Now a days, bio-adsorbents are emerging as a sustainable solution in wastewater treatment due to their eco-friendly nature and cost-effectiveness. Derived from natural or waste biomass, they effectively remove contaminants like heavy metals, dyes, and organic pollutants through adsorption processes. Their high surface area and functional groups facilitate the binding and sequestration of pollutants, making them easily recoverable and reusable. The use of bio-adsorbents not only aligns with green chemistry principles but also reduces reliance on more expensive and environmentally harsh treatments, promoting a cleaner and more sustainable approach to managing waste water. In the present issue, researchers demonstrated the effective use of bio-adsorbents prepared from coconut shells and wood apple pulp in removing different dyes. Another manuscript the issue delves into catalytic chemistry for green synthesis applications. Through the comparison of different metal organic frameworks, this study contributes to the development of efficient catalysts for organic transformations, promoting greener and more

sustainable chemical processes. The research paper on atmospheric pollution sheds light on the alarming levels of tropospheric ozone, a key component of air pollution. With a focus on a major urban center, this research underscores the urgent need for effective air quality management strategies to safeguard public health and environmental well-being.

The manuscripts featured in this issue exemplify the interdisciplinary nature of analytical science and its pivotal role in advancing sustainable development goals. As we navigate complex environmental challenges, it is imperative to continue fostering collaboration between academia, industry, and policymakers to implement evidence-based solutions for a cleaner and healthier planet.

I extend my gratitude to the authors, reviewers, readers, editorial and advisory committee members for their contributions and support in advancing the frontiers of analytical science for sustainable environmental solutions. I sincerely thank ISAS president and J.ISAS Advisor, Dr. Raghav Saran, as well as Dr. Vijayalaxmi Adya and Dr. Vinay Bhandari for their continuous cooperation in bringing this issue.. Technical support from Shivani Kantak and Vaibhav Parse is highly appreciated



Dr. Nilima Rajurkar
Editor in Chief
Journal of ISAS

Journal of ISAS

ISSN : 2583-5459 2(4), Pages 1 to 90, (2024)

(An open access Peer reviewed quarterly e- journal by Indian Society of Analytical Scientists)

Contents

S.No.	Title and Authors	Page no.
1	Research Paper: Sustainable Development in Dye Waste Management: A Comparative Study on the Effectiveness of Adsorption and γ -Radiolysis Anupama Prabhala*, Naina Raje, Sanjay Sethi, Sangita Pal, Beena G Singh Email*: anuvivek@barc.gov.in DOI: 10.59143/isas.jisas.2.4.KZBG4323	1-22
2	Research Paper: Development of Biomass Derived Adsorbents using Wood Apple Pulp for the Removal of Contaminants Surabhi S. Raj, Pooja Thanekar, Kshama Balapure, Vinay M. Bhandari* Email*: ym.bhandari@ncl.res.in DOI:10.59143/isas.jisas.2.4.DNLJ2831	23-43
3	Research Paper: Comparing The Catalytic Activity of Mg-BTC Metal Organic Framework and Post Synthetically Modified (TiO ₂ @ Mg-BTC) Metal Organic Framework for Cyanosilylation of Aldehydes S. Santhana Laxmi and K. Usha Nandhini* Email*: kusha.chem@gmail.com DOI:10.59143/isas.jisas.2.4.WLLN4213	44-59
4	Research Paper: Tropospheric Ozone levels in and around southern city Bengaluru, India P. Anukrishna, Aditya D. Chate* and G. Dhanya Email*: admin@smitenvirosolutions.in DOI: 10.59143/isas.jisas.2.4.CBYD6947	60-73
5	Research Paper: Removal of crystal violet, an emerging pollutant from aqueous solution using biochar prepared from coconut shell Jonty Rodrigues, Sugandha Shetye*, Sheba Raju Email*: sugandha@somaiya.edu DOI : 10.59143/isas.jisas.2.4.HFXO7613	74-90

Sustainable Development in Dye Waste Management: A Comparative Study on the Effectiveness of Adsorption and γ -Radiolysis

Anupama Prabhala^{1,2*}, Naina Raje³, Sanjay Sethi², Sangita Pal^{1,4}, Beena G Singh^{1,5}

¹Homi Bhabha National Institute, Anushakti Nagar, Mumbai - 400094

²Advanced Tuneable Laser Applications Division, BARC, Mumbai

³Analytical Chemistry Division, BARC, Mumbai

⁴Board of Research in Nuclear Sciences, DAE, Mumbai

⁵Radiation & Photochemistry Division, BARC (Bhabha Atomic Research Centre), Mumbai, India - 400085

Email: *anuvivek@barc.gov.in

Received: 13.3.2024, Revised: 5.4.2024, 14.4.2024, Accepted: 15.4.24

ABSTRACT

Pyromethene 567 (PM567), a BODIPY class of dye; is widely used in medicine, chemistry, material science, and high-power dye lasers. During its use, PM567 dye waste is generated in ethanol solvent which needs to be treated before its disposal. In our study, we aim to compare the effectiveness of two methods for PM567 liquid waste treatment: γ -radiolysis, an advanced oxidation process (AOP), and adsorption, a simple and easy option. Interestingly, we observed that AOPs like γ -radiolysis were not efficient for dye effluent treatment in organic solvents. This inefficiency was attributed to competing reactions leading to the scavenging of dye-degrading radicals. At the highest γ -dose rate (3.5 kGy) feasible in the system; 62% is the maximum removal efficiency achieved by this method. For a comparison, we also investigated the adsorption efficiency of PM567 dye from ethanol solvent using commercially available adsorbents. Among these, powdered activated carbon (PAC) demonstrated the highest removal efficiency, reaching 95%, much higher than that of γ -radiolysis method. In line with the pursuit of sustainable development, we synthesized granular activated carbons (AC1, AC2, AC3) from coconut shells, a lignocellulosic bio-waste. The characterization of these carbons revealed that AC3, with a higher iodine value and CCl_4 activity, possessed a systematic pore structure (SEM analysis), a larger specific surface area ($1708 \text{ m}^2 \cdot \text{g}^{-1}$), and a higher micro-pore volume ($0.61 \text{ cc} \cdot \text{g}^{-1}$). AC3 hence, emerged as the most effective adsorbent, achieving 95% efficiency comparable to PAC.

These findings highlight the significant potential of AC3 for liquid dye waste treatment, emphasizing its role in addressing environmental challenges and contributing to the promotion of sustainable development.

Keywords: Adsorption, Advanced oxidation processes (AOPs), BODIPY dye, Activated carbon, ethanol solvent, waste treatment

Introduction

The BODIPY class of dyes stand out as a versatile group with applications spanning diverse fields, from medicine to material sciences. These dyes, including Pyrromethene 567 (PM567), have proven invaluable in drug delivery, fluorescent probes, switches, electroluminescent films, solar cell sensitizers, and more, owing to their exceptional physicochemical properties¹. However, industrial processes utilizing BODIPY fluorescent dyes, such as PM567 in high-power liquid dye lasers, face challenges due to photochemical degradation during operation, leading to decreased laser efficiency and hence a need for periodic dye solution replacement arises^{2, 3, 4}. This replacement generates liquid waste containing dye in ethanol solvent, a concern also prevalent in industries using alcohol dyeing. The disposal of this liquid waste is typically managed through incineration^{5, 6}.

In response to the environmental impact of dye effluent treatment, different studies have pioneered an eco-friendly approach for treating the dye effluent, prioritizing sustainable methods over conventional practices. The literature available reveals a number of aqueous dye effluent treatment methods, which include physical separation, chemical treatment, advanced oxidation processes (AOPs), adsorption and biological methods⁷. AOPs, specifically gamma radiolysis, have demonstrated effectiveness in degrading aqueous dye effluent by utilizing ionizing radiation to generate oxidizing and reducing agents derived from radiolysis of the solvent⁸.

Adsorption known for its simplicity, and versatility in treating various effluent streams, emerges as another important method. Adsorbents such as silica gel, alumina, mesoporous carbon microbeads (MCMB), powdered activated carbon (PAC), Poly (2-hydroxyethyl methacrylate), (PHEMA) and Polymethyl methacrylate (PMMA) resin, have been found to be effective adsorbents for dyes due to their large surface area and pore volume^{9, 10, 11, 12, 13}. The commercially available adsorbents are however costly because of their synthetic origin¹⁴. Moreover, natural waste-derived activated carbons (ACs) have gained attention due to their cost effectiveness and environmental sustainability¹⁵.

A comparative analysis between γ -radiolysis and adsorption, assessing their efficacy as dye treatment methods for PM567 in ethanol is carried out in this study. Also, motivated by the abundant availability of coconut shells, a bio-waste product available in tropical countries like India, this study focuses on synthesizing ACs from coconut shell¹⁶. The comparative performance evaluation for PM567 dye adsorption in ethanol by the coconut shell-derived ACs with that of the most efficient commercial adsorbent is carried out. Furthermore, through these investigations, a step has been taken towards the development of sustainable and effective solutions for treatment of liquid waste containing dye in non-aqueous systems like ethanol.

Experimental

Chemicals and reagents

PM567 was synthesized at BARC and ethanol of > 99% purity was purchased from Advent Chembio, India respectively. The properties of PM567 are given in Table 1. Silica gel, alumina, PHEMA, PMMA resins and PAC (M/s. Merck make) were procured from M/s. VRS Enterprises, Mumbai, India. Mesocarbon microbeads (MCMB) of carbon were supplied by M/s. Nanoshel, India. In this study, ACs (AC1, AC2 and AC3) were prepared by physical method in which carbonization was followed by steam activation.

Instrumental techniques

The γ -radiolysis was carried out using a GC-5000 (M/s. BRIT make) γ - irradiator with ⁶⁰Co source with capacity of 14,000 Ci and maximum dose rate of ~ 4.4 kGy/hr as measured by Fricke dosimetry¹⁷. Pulsed radiolysis coupled with absorption detection was carried out using LINAC Facility (7 MeV, 2 μ s) available at RPCD, BARC¹⁸. Absorption spectra were recorded on a UV-visible spectrophotometer (Lab India -UV-3000+) in an optical quartz cell of 10 mm path-length at 25 °C for all the experiments. IR spectra were recorded using diamond single reflectance ATR in MIRacle™ ATR spectrometer. The samples were analysed over the range of 400–4000 cm^{-1} with a 4 cm^{-1} resolution. Netzsch thermo-balance (Model No.: STA 409 PC Luxx) was used for the TG-DTA studies. For the TGA studies, Pt vs. Pt-10% Rh thermocouple was used as a temperature sensor. Simultaneous TG–DTA data analysis was done using Proteus software from Netzsch. In the TG-DTA analysis, accurately weighed AC samples (5 to 10 mg quantity) were taken and heated in air/inert atmosphere in re-crystallized alumina crucibles from room temperature to 1000 °C at a heating rate of 10°C min^{-1} . High purity nitrogen flow was maintained at 100 mL min^{-1} for transport of the volatile

products. SEM images were generated by an electron microscope using an SEM of SEC Co. Ltd., South Korea. The surface area of the ACs was obtained using Brunauer–Emmer–Teller (BET) method with nitrogen adsorption at $-196\text{ }^{\circ}\text{C}$. Analysis was conducted using a Thermo Fisher Scientific S.p.A (model: SURFER ANALYZER) nitrogen adsorption–desorption analyser and the associated software. AC of $\sim 0.5\text{ g}$ was taken and vacuum degassed at $250\text{ }^{\circ}\text{C}$ overnight to remove any previously adsorbed vapours from the adsorbent. The sample cell was cooled to liquid N_2 temperature to obtain detectable amounts of N_2 gas adsorption. The N_2 gas was then fed in to the sample cell, maintained under partial vacuum condition and a number of data points were collected using highly accurate pressure transducers until saturation pressure was reached. After the adsorption cycle, the desorption cycle of the sample was obtained by heating the sample and recording the data.

γ -radiolysis of PM567

The γ -radiolysis experiments of PM567 dye in ethanol were carried out in batch mode. The PM567 dye solution of a fixed feed concentration, (C_0 , $200\text{ }\mu\text{M}$) was radiolysed with a Co-60 γ -source. The radiolysis was carried out in the dose range of 0.25 kGy to 3.5 kGy . The initial concentration of the dye, C_0 and the concentration C_D , after radiolysis at a particular dose were measured by UV-absorption spectrometry. An absorption spectrum was recorded in the wave-length range $300 - 600\text{ nm}$, the peak absorption was found to be at 518 nm (extinction coefficient of $65170\text{ M}^{-1}\text{cm}^{-1}$ in ethanol, Fig. 1). The G value, the radiation chemical yield, (i.e., the number of moles of PM567 dye degraded. J^{-1} of absorbed energy) is a measure of the degradation efficiency. G-value of the dye degraded in ethanol was estimated by equation (1).

$$G = \frac{(C_0 - C_D) * 0.789}{D * 10^6} \quad (1)$$

Where, C_0 and C_D are the molar dye concentrations (μM) initially and after gamma radiolysis at a given dose, D is dose in Gy and 0.789 is the ethanol density in kg.litre^{-1} at room temperature.

Activated carbon synthesis

The process of activating coconut shell consists of two-steps, i.e., carbonization and activation. In the first step of carbonization, the raw and cleaned ligno-cellulosic coconut shell is thermally treated to increase the carbon composition in the shell¹⁹. This is done by heating the shells in underground covered pits at around 500°C . After the carbonization the

material was cooled to room temperature and crushed. Further, the crushed charcoal was activated by physical steam activation method¹⁹. For this, the crushed shells along with saturated steam were fed into a rotary kiln. The temperature in the reaction zone was around 800°C. The contact time in the central reaction zone of the carbon material varied approximately from 20min, 40 min and 120 min for the three different activated carbons AC1, AC2 and AC3 respectively. The air-cooled product was removed after the required contact time, washed, dried, sieved and tested for physico-chemical properties before adsorption studies. A BSS mesh size of 60/30 mesh (250 - 500 µm) range was chosen for all the three prepared ACs.

Physico-chemical characterization

The physico-chemical properties of the prepared ACs i.e., the bulk density, moisture content, ash content, hardness, pH, CCl₄ value (IS 877: 1989) and Iodine number (IS 2752: 1995) were estimated and the procedure has been discussed in brief^{20, 21}. The apparent bulk density of ACs was calculated by recording the tapped volume occupied by 40 g of AC in a 100 mL graduated cylinder. For estimating the hardness of the ACs, a pre-weighed sample of AC was contacted with 12.7 mm and 9.5 mm diameter steel balls in a sieve shaker (15 numbers each) for 30 minutes. The sample was then sieved using 600-micron IS sieve. The weight of carbon retained above the mesh as a percentage of the total initial weight is the ball-pan hardness of the given AC. The moisture percentage of the AC was calculated from the weight loss of the pre-weighed activated carbon after heating at 110 °C ± 5 °C for 4 h in an oven and subsequently cooling it in a desiccator. Similarly, the ash content was obtained from the percentage weight loss in the initial weight on heating in a muffle furnace for 1000 °C ± 5 °C for 4 h. The carbon tetrachloride (CCl₄) activity of AC was estimated by passing CCl₄ gas over dried AC taken in an adsorption tube and measuring the final steady weight gained due to its adsorption as a percentage of the initial carbon weight. AC was dried, ground to pass through 75 micron IS sieve and then weighed accurately. The iodine number (IV) was estimated by treating 0.2 g of this dried AC with 40 mL of freshly prepared 0.1 N iodine solution for 4 minutes. The iodine solution after contacting with the AC was filtered and 10 mL of the filtrate was titrated against standard sodium thiosulphate solution. The iodine number is reported as iodine adsorbed per g of the dried AC (mg. g⁻¹). The zeta (ζ) potential of the three ACs was measured in water using Zetasizer instrument, M/s. Malvern Panalytical after sonicating the AC samples for 15 min.

Comparative batch adsorption study

All the batch studies were carried out in a M/s. Scigenic Biotech, OrbitechLTmodel, orbital shaker equipped with temperature controller incubator system. For comparing adsorption efficiency of the different ACs and commercial adsorbents, 20 mL of 200 μM PM567 prepared in ethanol was treated with a fixed amount of adsorbents (0.115g). The contact time was 4 h. The speed of orbital shaker and temperature was 150 ± 3 rpm and 25 ± 0.5 $^{\circ}\text{C}$, respectively. After 4 h of contact, the clear supernatant was analysed for PM567 concentration by monitoring the absorbance at 518 nm. The adsorption efficiency (%) was calculated by following equation (2), where C_0 is the initial dye concentration, C_t is the dye concentration at time t (4 h), post adsorption.

$$\text{Adsorption efficiency \%} = \frac{(C_0 - C_t) \times 100}{C_0} \quad (2)$$

Results & Discussion

γ -radiolysis of PM567:

Radiolysis of deaerated ethanol by γ - photon leads to the generation of primary species, namely the hydroxyethyl radical (R^{\bullet}), solvated electron, (e^-_{sol}), and solvent radical cation ($(\text{CH}_3\text{CH}_2\text{OH}^+)^{22}$). However, during spur expansion, the predominant radicals are R^{\bullet} and e^-_{sol} . These radicals exhibit reducing properties, and in the presence of oxygen they undergo a reaction to produce peroxy radical, which possesses oxidising characteristics. The G-value, representing the yield of R^{\bullet} and the peroxy radical, is estimated to be $0.31 \mu\text{mol}\cdot\text{J}^{-1}$ ²². Assuming the initial concentration of oxygen in the aerated ethanol is 1 mM, and from the reported G-value of the R^{\bullet} and the peroxy radical, it is reasonable to expect the presence of oxygen until the absorbed dose of 3.5 kGy. As peroxy radicals are known to have higher degradation ability and to avoid the cost of usage of inert gas like nitrogen and argon, the study was restricted mainly under aerated condition and in the absorbed dose range of 0.25 kGy to 3.5 kGy.

The effect of γ - irradiation on the degradation of PM567 in ethanol at different absorbed doses (Figure 2), shows that the dye concentration decreased from 195 μM to 158 μM (19%) at an absorbed dose of 0.25 kGy and from 195 μM to 77 μM (60.5%) at 3.3 kGy. Even on further increasing the dose to 3.5 kGy the dye degradation increase was only marginal (1.5%) (Figure 3). Additionally, the temperature of the dye solution in ethanol increased by nearly 10 $^{\circ}\text{C}$ while irradiating over the entire dose range of 0.25 kGy to 3.5

kGy. This led to ethanol vaporization, which condensed into the dye solution in the bottle after natural cooling outside the gamma chamber at the end of experiment (Figure 4). The experiment was not carried out at higher absorbed doses (max. 3.5 kGy) due to the vaporization of ethanol, potentially leading to a safety hazard and also due to the flattening of the degradation efficiency at 3.3 kGy. The average G-value of the degraded dye was estimated by plotting the decrease in concentration as a function of the absorbed dose (Figure 5). The resulting graph was linear and the slope equated to the average ($G_{\text{-PM567}}$) value (dye degraded /joule of energy) which was estimated to be 21nmol.J^{-1} . This value is lower by orders of magnitude than that observed in aqueous medium²³. The presence of an intercept value of $29.6\ \mu\text{mol/l}$ (Figure 5) indicates the presence of competing reactions like geminate recombination of the primary radicals produced during oxidation of PM567 by peroxy radicals. Such reactions are prevalent in the organic solvent with lower dielectric constant which results in lower $G_{\text{-PM567}}$ as compared to aqueous solution. Further, the reaction between the radicals produced by radiolysis of ethanol with PM567 in real time scale was studied by employing pulse radiolysis studies using a LINAC²⁴. The transient absorption spectra produced during the oxidation of PM567 by peroxy radical under ambient air saturated condition showed formation of transient absorption maxima at 340 nm, 430 nm and 580 nm (Figure 6a). In analogy to the transient spectrum obtained from photolysis experiments, these species have been attributed to the formation of BODIPY radical cation formed by initially charge separated species²⁵. The degradation of PM567 on oxidation is expected to be initiated by radical cation formation followed by ring opening²⁶. The radiolysis under argon saturated condition, which is expected to remove oxygen and form a reducing species, generated transient absorption spectrum with maximum at 550 nm (Figure 6b). In analogy to previous report, this species was attributed to formation of BODIPY radical anion²⁷. Unlike in aqueous medium, the lower G-value of the radical derived from ethanol reduces the dye degradation efficiency. It could thus be concluded that direct radiolysis of ethanolic dye solutions is not very effective in dye degradation.

Comparison of Adsorption efficiency of commercial adsorbents:

The comparison of adsorption of PM567 dye in ethanol for the various chosen commercial adsorbents after 4 h (contact time) is presented in Figure 7. PHEMA, MCMB had a very low efficiency of around 2%. Alumina and PMMA had 6% and silica gel 26%. The highest adsorption efficiency was observed with PAC at 95%. It is possible that lower specific surface area of MCMB, PHEMA, PMMA and alumina resulted in low dye adsorption

efficiency^{28, 11}. The PAC in its powdered form was likely to have high adsorption efficiency due to the high specific surface area. It was thus concluded that among the adsorbents tested, PAC was the most efficient adsorbent. In general, for scale-up of adsorption process, packed adsorber columns are employed. The very small particle size of PAC (≤ 0.18 mm ϕ) makes it difficult to use in a packed adsorption column due to a high pressure drop²⁹. However, as granular AC adsorbent (≥ 0.2 mm ϕ) is suitable for packed beds, synthesis of granular activated carbon from coconut shell, a biowaste was taken up.

Characterization of synthesized activated carbons:

The coconut shell (CS) mainly consists of C, O, H as elemental constituents which in turn constitute the principle lignocellulosic polymers of cellulose, hemicellulose and lignin³⁰. The composition of the three fractions in a carbon source mainly depend on the particular species, age, weather and the season when the product is reaped¹⁹. The cellulose and hemicellulose are reported to typically contain around 65% in the CS, while lignin is found to be slightly less than 30% in composition³¹.

The CS is generally carbonized using kiln or pit methods to convert them into carbon. The carbonization was carried out at 500⁰C by the pit method as it is less energy intensive. The temperature chosen was above 600⁰C; as a decrease in the yield of the char was reported above this temperature¹⁹. Carbonization resulted in the formation of carbon, after the moisture, volatiles, followed by aromatics of low molecular weight and hydrogen gas were evolved resulting in a fixed carbon skeleton filled with tar-like products. Further activation was required to produce AC with the required surface and textural properties. The AC from CS could be prepared by either physical or chemical activation process. In the chemical activation method, alkaline and acidic reagents like NaOH, KOH, ZnCl₂, and H₃PO₄ induce porosity in the carbon³². But chemical methods have their own intrinsic limitations as they generate additional chemical waste. In this work, the carbonized CS was physically activated in a rotary kiln using steam by an optimized method to prepare AC having higher surface area. The rotation of the kiln improved the heat transfer and provided good contact between the carbon particles and the steam. The water gas evolved due to the reaction between carbon and steam in the kiln led to the activation of the carbon³³.

The evidence of successful carbonization and activation was confirmed by monitoring the surface functional groups before carbonization and after activation by using FTIR (Figure 8). Non-carbonized coconut shell-based material showed stretching at 3350 cm⁻¹, 2920 cm⁻¹,

1728 cm^{-1} , 1240 cm^{-1} and 1031 cm^{-1} . The bands at 3350 cm^{-1} and 2920 cm^{-1} corresponds to O-H and C-H stretching vibration, respectively. The bands at 1728 cm^{-1} , 1240 cm^{-1} and 1031 cm^{-1} correspond to vibrations due to carbonyl group, which was due to C=O stretching, C-O stretching in aromatic ester and C-O stretching respectively. A band of weak intensity in the region 1680-1620 cm^{-1} corresponds to aromatic C=C stretching. The FTIR spectrum of AC was devoid of the aforementioned functional group except that the peaks at 1735 cm^{-1} , 1370 cm^{-1} and 1220 cm^{-1} , which can be attributed to respective -C=O, O-H stretching in phenol and C-O stretching vibration from carbonyl group confirming the removal of non-carbon component and complete carbonization³⁴.

The physico-chemical properties of ACs tabulated in Table 2 show that most of the properties like the bulk density, moisture content, ash content (%) and hardness were not significantly different for the three ACs. However, the iodine value and CCl_4 activity were found to increase in the order AC3 > AC2 > AC1, indicative of change in adsorption behaviour (Table 2). AC3 exhibited the highest ζ - potential among the three ACs in aqueous medium. The ζ -potential could not be measured in ethanolic medium as agglomeration of the AC was higher in ethanol preventing its suspension in ethanol.

The organic content in the ACs was derived from the thermogravimetric analysis (TGA) of the ACs³⁰. The TGA profiles of the synthesized ACs in air showed similar thermal properties, with two step decomposition reaction (Figure 9a). The first step of mass reduction was observed in the temperature region of room temperature to 125 °C and is well below 10 % which could be attributed to the loss of surface adsorbed moisture. This initial mass loss in the ACs may be related to the presence of oxygenated surface groups, responsible for hydrogen bonding developed between the ACs and the entrapped moisture. The onset of the second step decomposition irrespective of the ACs, started at 300°C, however the amount of residual formed was dependent on the nature of ACs³⁵. The second degradation step was attributed to the degradation of the lignocellulosic structures. The TGA results indicated that the carbonization condition in the AC obtained from the coconut shell should be established at higher temperatures (400–700 °C) to obtain a carbon-rich product. Also, it should be emphasized that the low level of ashes found in ACs (Table 2), is an important property in choosing a good precursor like coconut shell for the AC production. The presence of ashes can affect the chemical characteristics and the adsorptive behaviour of AC, hence the low ash level found in the studied AC is desirable. TG studies in nitrogen atmosphere showed higher mass loss in AC1. This was indicative of the presence of an oxygen rich functional group which supports combustion in an inert atmosphere and that the

oxygen rich organic content in the ACs followed the order $AC1 > AC2 > AC3$ (Plot (a) of Figure 10). As the TGA is comparatively broad, for clear thermal degradation pattern, DTA of AC1, AC2 and AC3 in air and nitrogen atmosphere were performed (Figure 9b and Figure 10b). The DTA of the ACs under aerated condition exhibited broad exothermic peak in the temperature range from 400 to 800 °C which are attributed to combustion of the organic content in the ACs. Further, DTA thermogram under nitrogen atmosphere exhibited exothermic peak centred at ~ 555°C for AC1 and AC2. The exothermic peak in presence of N₂ confirmed the presence of oxygen organic content, which may be due to lignocellulosic decomposition. The higher exothermic peak for AC1 is an indicator of higher oxygen organic content compared to the other ACs³⁵.

SEM was carried out to find the surface morphology of the ACs. The SEM image shows that the surface morphology of the ACs strongly depend on the treatment condition (Figure 9c, Figure 10c & 10d)³⁶. The SEM micrographs of AC1 and AC2 showed pores of irregular sizes with cracks observed at the edges of carbon surface. However, the pore density was higher in AC2 as compared to AC1. Contrary to this, the SEM image of AC3 carbon showed a systematic pattern of oval pores with smooth surface structures. These SEM images clearly indicated that AC3 has more regular porous structure, which results in its higher CCl₄ and iodine values.

The Raman spectra of ACs (Figure 9d) are characterized by presence of two bands centred at 1600 cm⁻¹ and 1350 cm⁻¹, generally termed as G-band and the D-band respectively³⁷. The D-band induced by sp³ electronic states is caused by the defects in the planar sp² graphitic structure. The G band, which is related to the graphite E_{2g} symmetry of the interlayer mode reflects the structural integrity of sp² –hybridised carbon atoms in carbon samples. In material characterization, these bands are used to estimate the extent of defects present in any carbon material. The intensity ratios of the D to the G band (I_D/I_G) irrespective of the nature of ACs remained nearly one. The result indicated that the physical activation of the ACs did not alter the ratio of defects but changed only the extent of pore formation.

The adsorption isotherm showing the volume of N₂ gas adsorbed/ desorbed with respect to the relative pressure ratio for the ACs is presented in Figure 11. The volume of the gas adsorbed on the ACs as a function of relative pressure increased exponentially and reached a plateau at relatively lower pressure of approximately 0.4, which is an indicative of a microporous structure. The N₂ adsorption/ desorption isotherms were used to calculate the

monolayer volume (ncc/g), specific surface area (m^2/g) and micro-pore volume by means of the Dubinin method³⁸. The micropore volume, monolayer volume and specific surface area of AC3 were higher than that of AC2 and AC1 (Table 3).

Adsorption efficiency comparison:

Adsorption of PM567 dye in ethanol medium was determined for all the ACs. The comparative adsorption of PM567 on AC1, AC2 and AC3 and the adsorption efficiency in the order of $\text{AC1} < \text{AC2} \leq \text{AC3}$ (Figure 12), corroborate the effect of higher porosity and specific surface area on increased dye adsorption.

Conclusions

In conclusion, a comparison of the PM567 dye removal efficiency in ethanol by γ -radiolysis and adsorption showed that adsorption by activated carbon synthesized from bio-waste was 95% efficient while it was limited to 62% by γ -radiolysis at 3.5 kGy. This low efficiency ethanol solvent by γ -radiolysis was due to geminate recombinant reactions of the dye degrading radicals formed leading to a very low radiochemical yield of 21 nmol.J^{-1} . The present investigation also revealed that powdered activated carbon demonstrated the highest efficiency in PM567 dye adsorption from ethanol among the examined adsorbents. To further optimize its utility in a packed bed configuration, a simple method for synthesizing granular activated carbon (AC1, AC2, and AC3) through time-dependent steam activation of coconut shell bio-waste was optimized. Notably, granular AC3 exhibited comparable adsorption efficiency ($95 \pm 4\%$) to powdered activated carbon, attributed to its higher surface area ($1708 \text{ m}^2.\text{g}^{-1}$) and pore volume (0.61 cc.g^{-1}). This initial comparison highlights the superior performance of activated carbon in adsorption compared to radiation-induced degradation. Moving forward, the future studies will focus on understanding batch adsorption mechanism in non-aqueous effluents, and exploring the feasibility of transitioning from batch processes to a packed adsorption column configuration.

Acknowledgements:

The authors would like to express their gratitude to Dr. Archana Sharma, Director, BTDG, BARC, Shri Soumitra Kundu, Head, ATLAD, BARC and Dr. Awadhesh Kumar, Associate Director, CG, BARC for supporting this work. Dr. K. Dasgupta, G& AMD, BARC is acknowledged for the Raman spectra and surface area analysis. Dr. Sunita Kedia, L& PTD

is acknowledged for the SEM analysis. Dr. Gautam S., Head, FTD, BARC is acknowledged for permitting to use the orbital incubator shaker. Shri Sunil Dehade is acknowledged for his assistance in the experimental work. M/s. Industrial Chemicals, Gujarat, India is acknowledged for use of their facility to synthesize the activated carbons.

Figures:

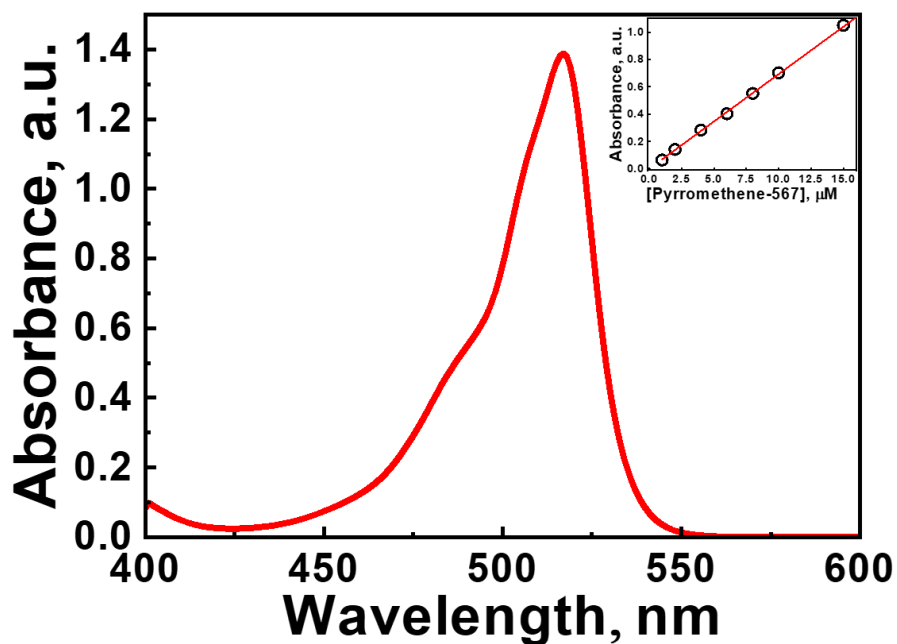


Fig. 1: Absorption spectrum of PM567 in ethanol. Inset shows the plot to estimate extinction coefficient of PM567 in ethanol

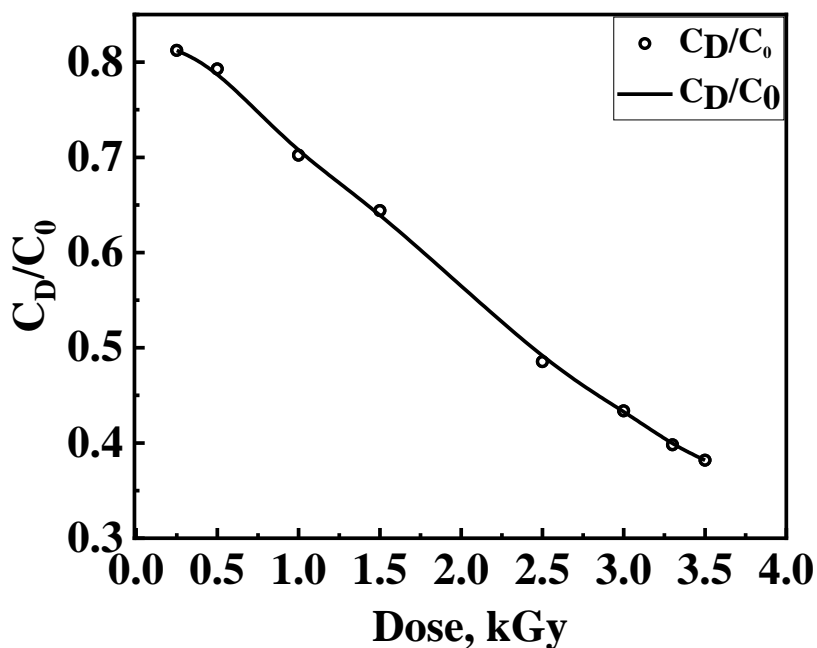


Fig. 2: PM567 dye degradation ratio (C_D/C_0) as a function of absorbed dose after gamma radiolysis in ethanol solvent

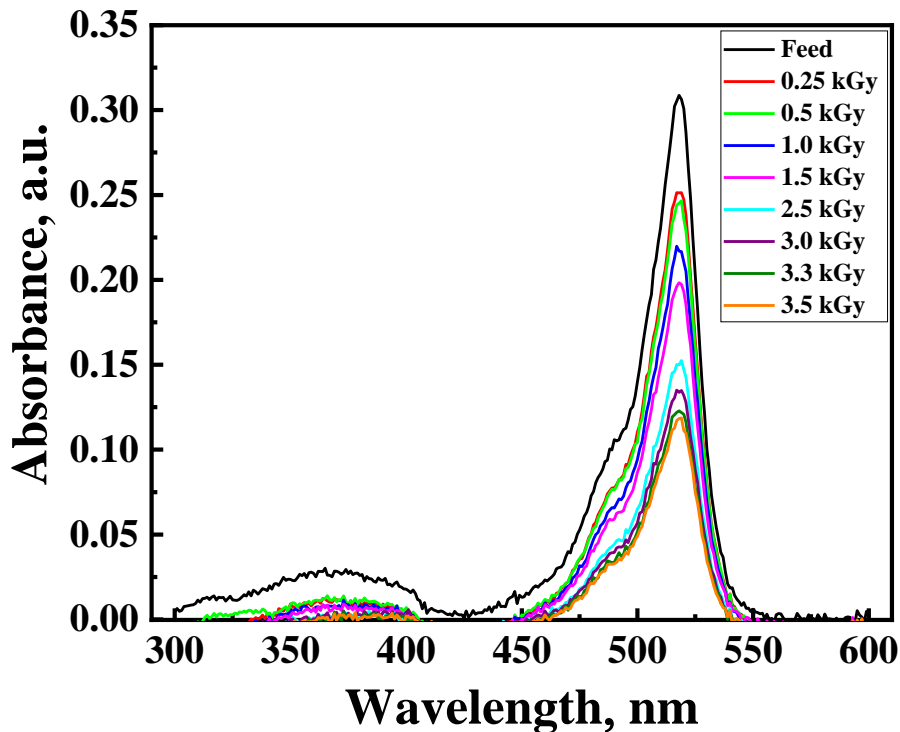


Fig. 3: Dose dependent absorbance spectra of feed and γ -radiolysed PM567 dye in ethanol

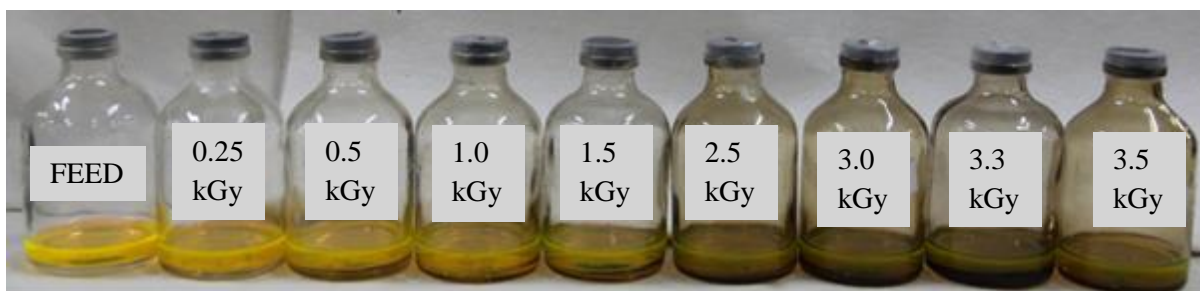


Fig. 4: PM567 feed and gamma radiolysed degraded dye at different absorbed doses (in ethanol)

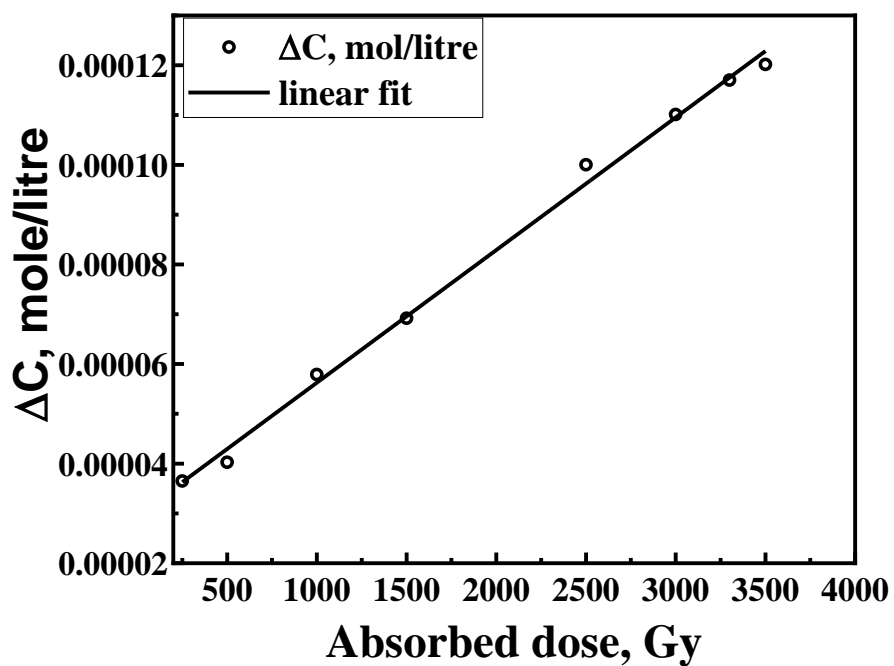


Fig. 5: G-value estimation for PM567 dye degradation by gamma radiolysis in ethanol

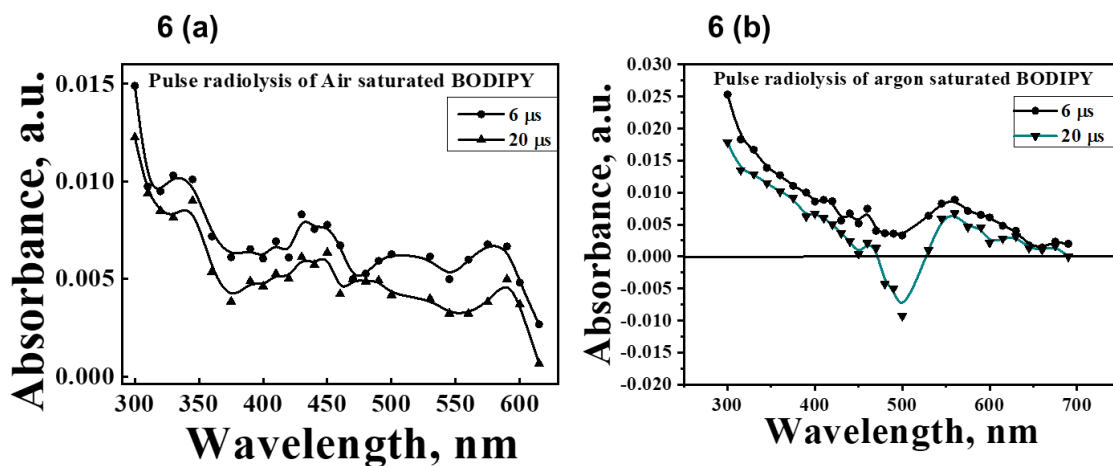


Fig. 6: Pulse radiolysis of (a) air saturated PM567, (b) Argon saturated PM567 in ethanol

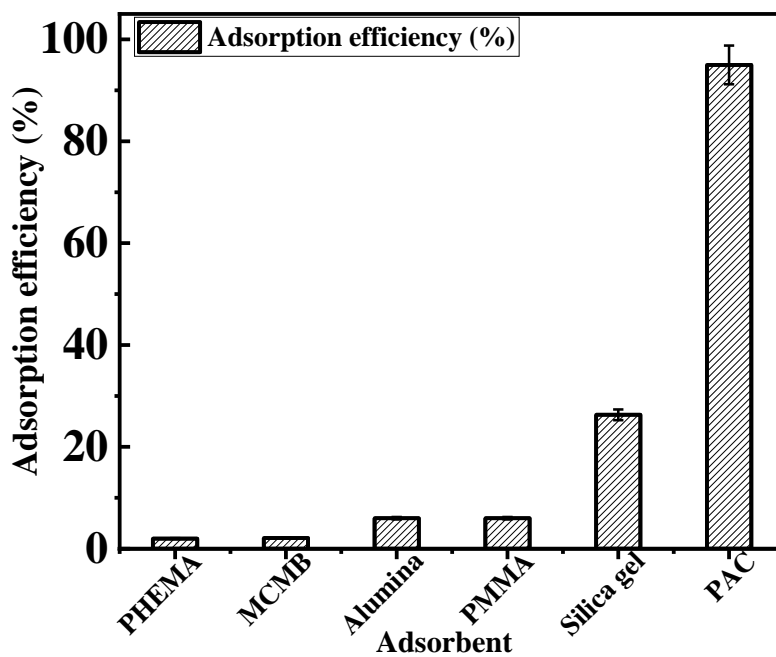


Fig. 7: Adsorption efficiency (%) for PM567 in ethanol solvent on commercial adsorbents

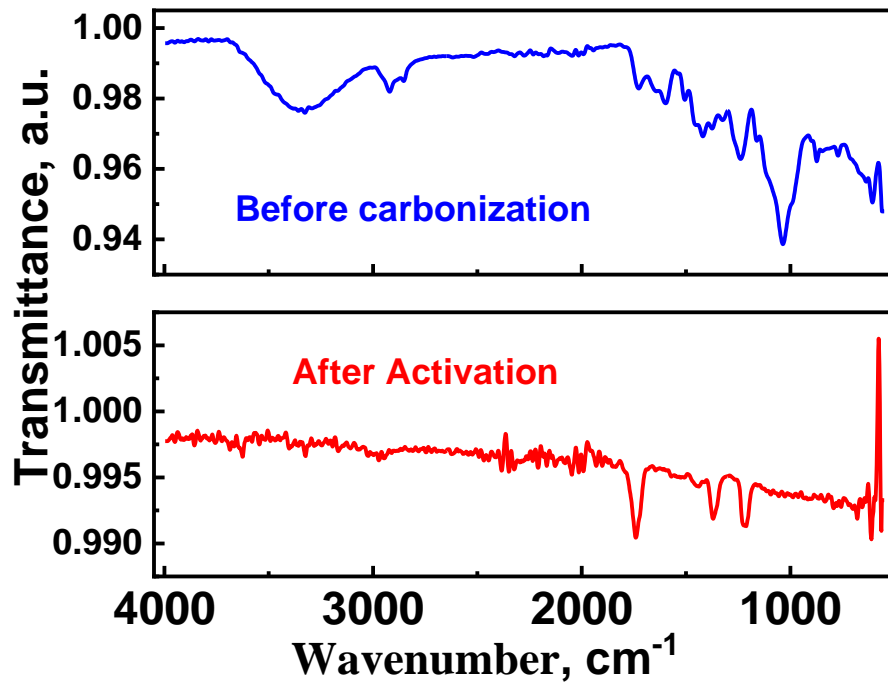


Fig. 8: FT-IR spectrum obtained from coconut shell before carbonization (blue) and after steam activation (red)

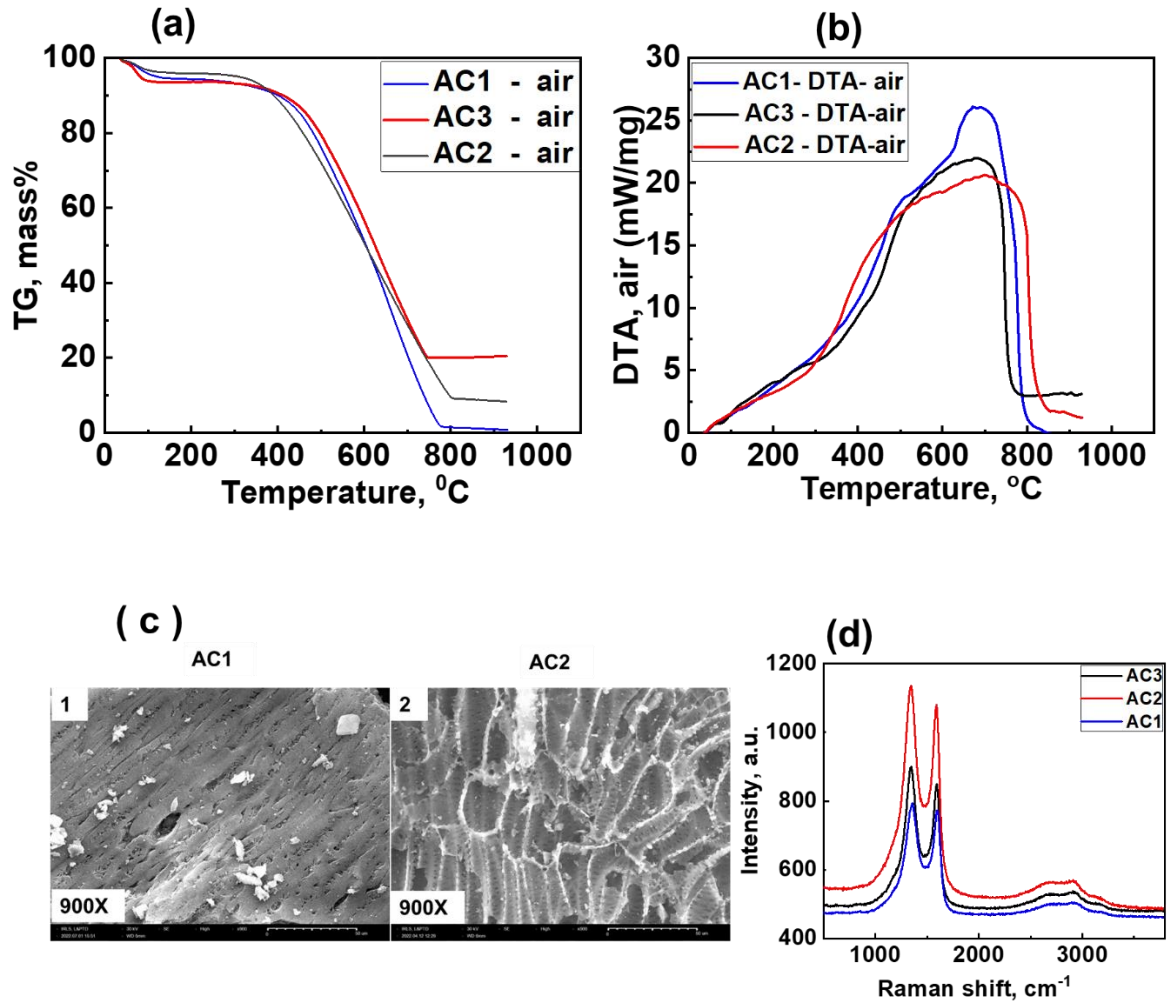


Fig. 9: (a) Thermogram of ACs in air (b) DTA of ACs in air (c) SEM of AC1 and AC2, (d) Raman spectra of ACs

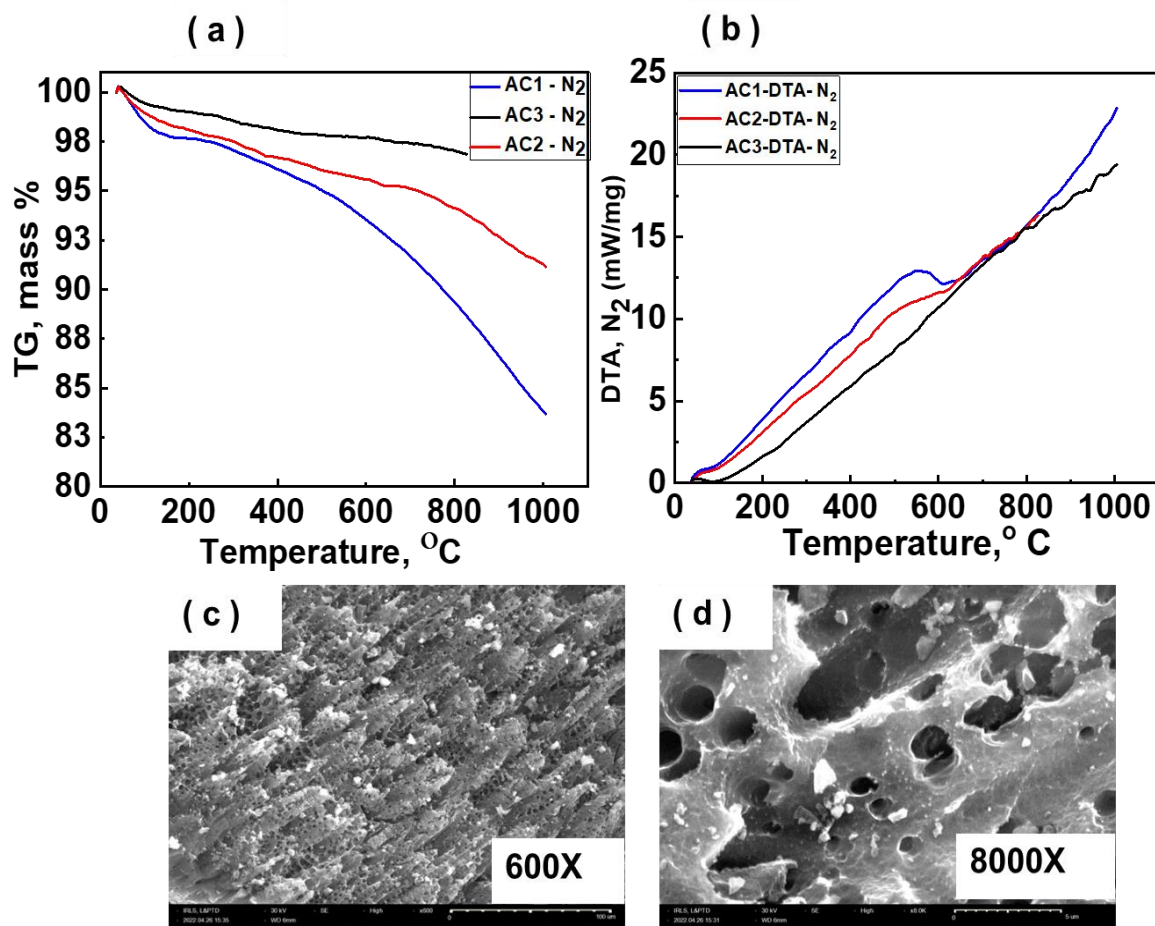


Fig. 10: Plot (a) The respective thermogram of different ACs in presence of inert condition. Plot (b) The DTA plot of the different ACs obtained on heating under N₂ condition. Plot (c) and Plot (d) are the SEM images of the AC3 at two different resolutions.

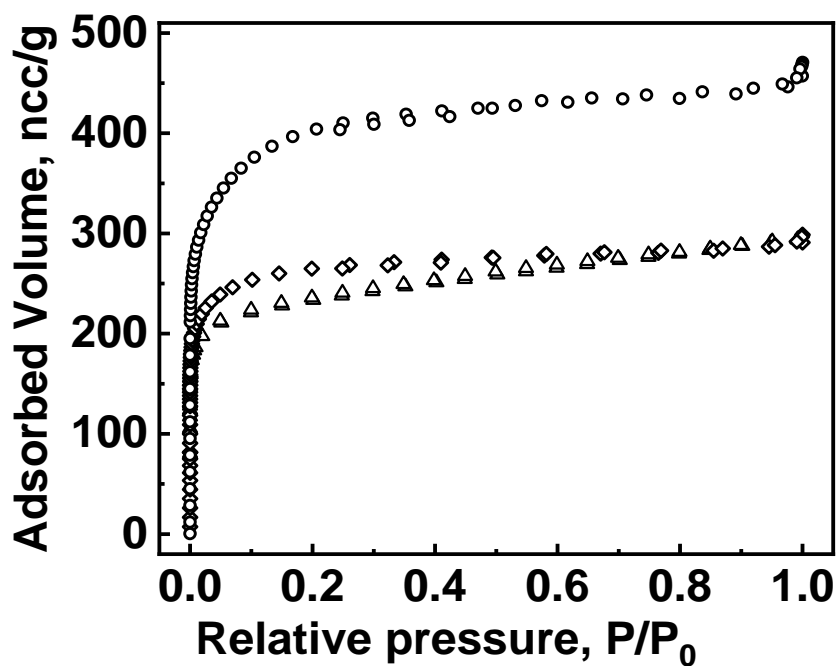


Fig. 11: Isotherm (BET) for AC1 (Δ) AC2 (◇) and AC3 (○)

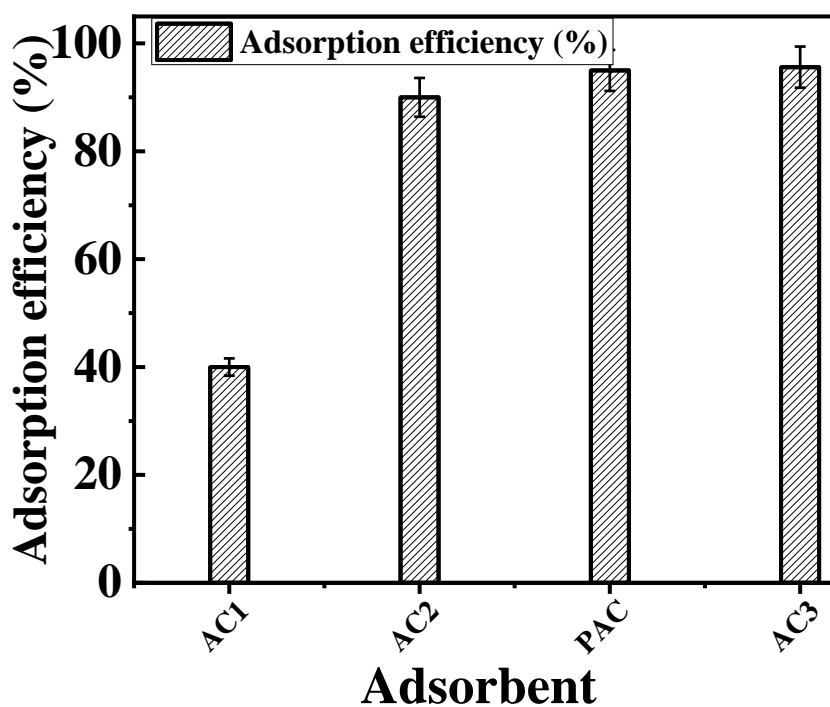


Fig. 12: Comparison of Adsorption efficiency (%) of ACs

Tables:

Table 1: Properties of PM567 dye

Molecular formula	$C_{18}H_{25}BF_2N_2$
Molecular weight	318.22
λ_{max} (nm) for UV Visible absorption	518
Molecular volume	273.373 \AA^3

Table 2: Physico-chemical properties of the ACs

Parameter	AC1	AC2	AC3
Bulk density (gcm^{-3})	0.5	0.5	0.4
Moisture Content (%)	2%	2%	2%
Ash content (%)	2.9 %	2.7%	2.7%
Hardness	99.2	96.1	96.1
pH	7	7	7
Iodine number (mg/g)	1017	1245	1340
CCl_4 activity	43	53	>85
ζ - potential in water, mV	-31.4	-34.7	-38.5

Table 3: N_2 adsorption/desorption isotherm data of the ACs

Parameter	AC1	AC2	AC3
Monolayer volume (ncc/g)	202.3	260.1	392.4
Specific surface area (m^2/g)	880	1132	1708
μ -pore volume (cc/g)	0.27	0.40	0.61
Average pore radius (\AA)	< 20	21.2	20.7
Correlation factor	0.975	0.982	0.974

References

1. Lakshmi Vellanki, Ritambhara Sharma & Ravikanth Mangalampalli, Reports Org Chem., Taylor & Francis, London, 1, 2016.
2. K K Jagtap, D K Maity, A K Ray, K Dasgupta, S K Ghosh., *Pramana - J Phys.* 75(5), 985, 2010.
3. V S Rawat, J Mukherjee, L M Gantayet, *Prog Quantum Electronics*, 43, 31, 2015.
4. S Sinha, S Sasikumar, A K Ray, Dasgupta K, *Appl Phys B Lasers Opt.*;78(3-4), 401, 2004.
5. Ferrero F, Periolatto M, Rovero G, Giansetti M, *J Clean Prod.* 19 (12), 1377, 2011.
6. A L Lotts, M L Spaeth, J I Davis, *AVLIS Production Plant Waste Management Plan*, UCID-20197, Lawrence Livermore National Laboratory, Oak Ridge, USA, 1984.
7. S Mondal, M K Purkait, S De, *Advances in Dye Removal Technologies*, Springer, Singapore, 2018.
8. J P Guin, Y K Bhardwaj, D B Naik, L Varshney., *RSC Adv.*, 4(96), 53921, 2014.
9. F S Wahshi, M D Alqahtani, M Abdulla, T Ramachandran, F Hamed, T Thiemann, 48, 10, 2020.
10. S K Parida, S Dash, S Patel, B K Mishra, *Adv Colloid Interface Sci.*, 121(1-3):77, 2006.
11. E P Fernandes, T S Silva, C M Carvalho, et al., *J Environ Chem Eng.*,9(5), 106198, 2021.
12. R S Dassanayake, S Acharya, N Abidi, *Molecules.* 26(15), 4697, 2021.
13. A G Rios, L C Matos, Y A Manrique, J M Loureiro, A Mendes, A F P Ferreira., *Adsorption*, 26(1), 75, 2020.
14. G Mezohegyi, F P Van der Zee, J Font, A Fortuny, A Fabregat, *J Environ Manage.* 102, 148, 2012.
15. M M Hassan, C M Carr, *Chemosphere*, 265, 129087, 2021.
16. R Kabir Ahmad, S Anwar Sulaiman, S Yusup, Sham Dol S, Inayat M, Aminu Umar H., *Ain Shams Eng J.*, 13(1), 101499, 2022.
17. *Standard Practice for Using the Fricke Dosimetry System*, ASTM ISO/ASTME1026-15, ISO, Geneva, 2015.
18. S.N.Guha, P.N.Moorthy, K. Kishore DBN and KNR, *Chem Sci.* 99(4), 261, 1987.
19. P González-García, *Renew Sustain Energy Rev.*, 82, 1393, 2018.
20. *Indian Standard, IS 877(2)*, Bureau Indian Standards, New Delhi, 1990.

21. Indian Standard, IS 2752, Bureau of Indian Standards, New Delhi, 1995.
22. D Jore, N Champion, N Kaouadji, J P Jay-Gerin, & C Ferradini, International Journal of Radiation Applications and Instrumentation. Part C. Radiation Physics and Chemistry 32(3), 443, 1988.
23. R Changotra, J P Guin, S A Khader, A Dhir, J Environ Chem Eng., 8(5), 104423, 2020
24. S.N.Guha, P.N.Moorthy, K. Kishore DBN and KNR, Chem Sci. 99(4), 261, 1987.
25. Shigeki Hattori, Kei Ohkubo, Yasuteru Urano, Hisato Sunahara, Tetsuo Nagano, Yuji Wada, Nikolai V. Tkachenko, Helge Lemmetyinen, and Shunichi Fukuzumi, J Phys Chem B., 109(32), 15368, 2005.
26. Y Qi, T Geib, A M Huynh, G Jung, DA Volmer, Rapid Commun Mass Spectrom., 29(9), 885, 2015.
27. Victoria J. Richards, Alexandra L. Gower, Jasper E. H. B. Smith, E. Stephen Davies, Dorothe'e Lahaye, Anna G. Slater (ne'e Phillips), William Lewis, Alexander J. Blake, Neil R. Champness and Deborah L. Kays, Chem Commun.; 48(12):1751, 2012.
28. M T Yagub, T K Sen, S Afroze, H M Ang., A review. Adv Colloid Interface Sci., 209, 172, 2014.
29. H Patel, Int J Environ Sci Technol., 19(10), 10409, 2022.
30. Q Wang, J Sarkar, Int J Energy Prod Manag. 3(1), 34, 2018.
31. R Krishnan, L Hauchhum, R Gupta, S Pattanayak., 2nd International Conference on Energy, Power and Environment : Theme: Towards Smart Technology : ICEPE-2018, NIT, Meghalaya, PP 1, June, 2018.
32. A Rehman, M Park, S J Park., Coatings.:9(2), 1, 2019.
33. S Zhao, L Chen, Biomass Convers Biorefinery. 12(9), 3943, 2022.
34. H Madzaki, Wawab Karimghani, Nurzalikharebitanim, Azilbaharialias., Procedia Eng., 148, 718, 2016.
35. A Bazan, P Nowicki, P Półrołniczak, R Pietrzak, J Therm Anal Calorim., 25(3), 1199, 2016.
36. Tsai WT, Jiang TJ., Biomass Convers Biorefinery, 8(3), 711, 2018.
37. N M Keppetipola, M Dissanayake, P Dissanayake, et al., RSC Adv., 11(5), 2854, 2021.
38. C Bläker, J Muthmann, C Pasel, D Bathen, Chem BioEng Rev., 6(4), 119, 2019.

Development of Biomass Derived Adsorbents using Wood Apple Pulp for the Removal of Contaminants

Surabhi S. Raj^{1,2}, Pooja Thanekar¹, Kshama Balapure¹, Vinay M. Bhandari^{*1,2}

¹Chemical Engineering and Process Development Division
CSIR-National Chemical Laboratory, Pune-411008, India

²Academy of Scientific and Innovative Research (AcSIR), Ghaziabad- 201002, India

*Email: vm.bhandari@ncl.res.in

Received: 15.3.2024, Revised: 20.4.2024, Accepted: 22.4.2024

Abstract

This study involves the development of biomass derived adsorbents from wood apple pulp for water and wastewater treatment. This biomass was modified by the addition of commercially available activated charcoal and copper nanoparticles. Adsorbent characterization was performed for understanding the surface morphology and surface area. These new adsorbents were further evaluated for their potentiality in removing dyes and API pollutants (Active Pharmaceutical Ingredient). All the adsorbents were highly effective in the removal of these contaminants, 96% of Malachite Green and 72% of Congo Red was removed with a high adsorption capacity of 45 mg/g. API pollutant (Ciprofloxacin) removal showed 52% removal, which is greater when compared to several modified adsorbents. Adsorption equilibrium models (Langmuir and Freundlich) and kinetic models (pseudo first order and pseudo second order) were evaluated for fit of the experimental data. In general, the isotherm studies indicated multilayer adsorption.

Keywords: *Adsorption, API pollutant, Characterization, Dye removal, Wood Apple*

1. Introduction

Water plays an essential role in human life and it is necessary to fulfil the everyday requirements of every living being on this planet¹. Several textile industries release toxic dyes and other organic pollutants into water and have known to be one of the most polluting industries of all. Growth of pharmaceutical industries, has led to the release of various antibiotics into natural water resources, and since their rate of entry into the environment is higher than their rate of elimination, they often tend to stay in water for long periods of time, hence referred to as pseudo-persistent. This persistence poses toxic effects on all living beings from microorganisms to humans². Different treatment technologies, e.g. coagulation, adsorption, advanced oxidation processes, biological treatment, membrane separation etc. are practiced for the removal of various pollutants³. Adsorption process is noted to be one of the most promising methodologies for the removal of organic pollutants existing in extremely low concentrations.

Large quantities of water and toxic chemicals are released from textile industries which are ultimately discharged into the water bodies in the form of effluents. Even the smallest quantity of dye can be clearly identified by their colour in the water streams⁴. Amongst various dyes, azo dyes like Malachite Green and Congo Red cause serious problems when released into water streams⁵. They exhibit carcinogenic and allergic properties which can cause adverse effects on aquatic and human lives^{6,7}. Large scale production of antibiotics has led to migration of them into the environment causing pathogenic resistance, and extensive usage has led to the accumulation of these antibiotics in sediment, surface and groundwater⁸. Amongst several antibiotics Ciprofloxacin (CIP) was frequently identified in surface and wastewater with a concentration of $150 \mu\text{g L}^{-1}$ in hospital effluents⁹.

Several methods have been reported to remove dyes and low concentrations of API pollutants from water, out of which adsorption, membrane separation and coagulation are the most frequently used methods. Owing to its efficiency, availability, ease of operation and less cost, adsorption process using activated carbon materials is frequently used. It can be directly implemented into the treatment process, does not require any special design or condition and is capable of removing colour imparted from the toxic dyes at very low concentrations¹⁰. Usually in industries, commercially available activated carbon is used in treatment processes, but manufacturing and regeneration of it contributes to high costs. Significant research is being conducted on developing environmentally friendly low-cost biomass derived adsorbents which can replace the chemically synthesised activated carbon¹¹.

Several studies have been reported that show bio-based activated carbon materials are versatile in nature and can be used for various applications. Activated carbon derived from coffee waste and banana peel was used to remove Congo Red¹². Recent studies involving modified adsorbents such as prickly fruit pear and conductive polymer matrix have effectively removed Congo Red from water¹³. Different low-cost adsorbents derived from biomass prepared from *Borassus Flabellifer* (palm), *Lupinus Albus* seed peel, avocado fruit peel have been reported to remove Malachite Green dye from aqueous solutions¹⁴. Dao et al.¹⁵ used several agricultural wastes such as straw, wood apple shell, banana peels, tea waste and avocado shells to remove Ciprofloxacin from water. Technological advances have allowed researchers to study biomass composites like methyl polysiloxane with avocado biochar and zinc oxide impregnated activated carbon prepared from jack fruit peel and their efficiency in removing Ciprofloxacin from aqueous solutions¹⁶.

The present study was undertaken to evaluate the performance of biomass-derived adsorbents from ripened wood apple biomass for water and wastewater treatment. Adsorbent modifications were achieved by combining biomass with commercially available activated carbon to evaluate the efficiency when compared to pure biomass. Copper modified adsorbent was prepared by doping copper nanoparticles into a carbon matrix. The characterization of the adsorbents and efficacy was investigated with two case studies on the removal of dyes namely Malachite Green (MG) and Congo Red (CR) and one API pollutant Ciprofloxacin (CIP). The experimental data was fitted using the adsorption equilibrium models (Langmuir and Freundlich) and kinetic models (pseudo first order and pseudo second order). The present study reveals strategy for devising biomass-derived adsorbents for the utilization of easily available biomass which is a renewable material and can be sustainable/cost-effective alternative.

2. Materials and Methods

2.1 Materials

Ripened fruits of wood apple, were obtained locally from Pune, Maharashtra, India. The chemicals used were of analytical grade. Copper nanoparticles (Cu, 99.9%) were procured from the Nano Research Lab, India. Model dye pollutants used for adsorption studies were Malachite Green (MG) ($C_{52}H_{54}N_4O_{12}$; CAS No. 2437-29-8, MW:927.03, $\lambda_{max}=617$ nm, Thomas baker) and Congo Red (CR) ($C_{32}H_{22}N_6Na_2O_6S_2$; CAS No. 573-58-0, MW:696.65, $\lambda_{max}=496$ nm, Loba Chemie). For API pollutant removal studies, Ciprofloxacin

Hydrochloride Hydrate (CIP) ($C_{17}H_{18}FN_3O_3 \cdot HCl$, CAS No. 86393-32-0, MW:367.8, $\lambda_{max}=275-282$ nm, >98% purity, Sisco Research Laboratories Pvt. Ltd.) was used as a model pollutant. The commercial activated charcoal (powder form) was procured from Fluka. Spectroquant® Pharo 100 spectrophotometer (MERCK, India) was used for the measurement of Chemical oxygen demand (COD)/dye concentration. The samples were digested using Spectroquant® TR 320 (2 h at 148 °C). The Ciprofloxacin concentration was analysed using Agilent Technologies Cary 8454 (UV-Vis of wavelength range 200-800 nm).

2.2 Preparation of activated carbon from biomass

Ripened wood apple fruits were washed with distilled water and dried at room temperature. The inner pulp was scooped out from the outer hard shell for the preparation of different adsorbents. Different material modifications were performed as listed below:

- a) Wood apple biomass (WA200): Fruit pulp was collected and coarsely ground using a regular mixer grinder. It was then dried at 60 °C in a hot air oven for 24 – 48 h to remove the moisture content. The biomass was then activated in a tube furnace employing inert gas atmosphere (nitrogen, flow rate 100 LPH) at 200 °C for 4 hours. The sample was then collected, weighed and ground into a fine powder for further studies.
- b) Wood apple biomass converted into activated carbon (WA350): Fruit pulp was collected and the previous steps were repeated. The dried biomass was then subjected to thermal treatment in a tube furnace in an inert atmosphere with nitrogen flow of 100 LPH at 350 °C for 4 hours.
- c) Wood apple biomass with activated charcoal (WAC200): The wood apple pulp was mixed appropriately with commercially available activated charcoal in 1:2 (activated charcoal: pulp) weight ratio. This step was performed to stabilise and preserve the natural compounds present in the pulp. The mixture was then dried at 60 °C for 24 – 48 h, activated in a tube furnace employing inert gas atmosphere (nitrogen, flow rate 100 LPH) at 200 °C for 4 hours.
- d) Wood apple biomass with activated charcoal converted into activated carbon (WAC350): This biomass was prepared using steps similar to WAC200. The dried mixture was then converted to activated carbon in a tube furnace in inert atmosphere at 350 °C for 4 hours.

2.3 Preparation of copper bio nanocomposite

Wood apple ripened fruits were washed and dried at room temperature. The hard shell was then broken to collect the inner pulp which was ground coarsely in a mixer grinder. To this mixture 1% of copper nanoparticles were added. To partially remove the moisture content, the mixture was dried at 60 °C. This dried material was subjected to thermal activation in an inert atmosphere at 350 °C for 4 hours. Finally, the adsorbent, was named as WA-Cu for further convenience (Fig. 1).

2.4 Details of instrumentation for characterizing adsorbents

The adsorbent morphology was studied using field emission scanning electron microscope, FESEM (FEI Quanta 200, Netherlands; 3D dual beam with a resolution of 3nm at 30kV, tungsten filament as the electron source under high vacuum mode). Energy dispersive X-ray spectrometer, EDS (EDAX, AMETEK, Netherlands) was used for elemental analysis. Brunauer-Emmett-Teller (BET) (Quanta Chrome® ASiQwin™ Autosorb, USA) was used for the surface area and pore size analysis. The pyrolysis process and the carbonisation temperatures were investigated by thermogravimetric analysis (TGA) (PerkinElmer STA 6000 simultaneous thermal analyser, USA). The identification of functional groups was done by Fourier transform infrared spectroscopy (FTIR) (FTIR-2000, PerkinElmer, Germany). Powder X-ray diffraction studies were carried out using X'Pert Pro PANalytical XRD (Netherlands) with Cu K α radiation ($\lambda = 1.542 \text{ \AA}$) in 2θ range of 10–80°.

2.5 Experimental

2.5.1 Removal of Dyes and API pollutant

Batch experiments were performed to check the efficiency of the prepared adsorbents in removal of organic pollutants from water. Malachite Green and Congo Red were used as model dye systems and Ciprofloxacin Hydrochloride Hydrate was used as an API system for adsorption studies. An initial dye concentration of 50 ppm and API concentration of 20 ppm was used to perform experiments. Adsorbent dosage was fixed to be 0.1% in 20 ml of synthetic solutions of dye and API. Batch studies were conducted in an orbital shaker at a speed of 120 rpm for 16 h at pH ~6.5 and at the ambient temperature, 30 \pm 1 °C. After filtering

out the adsorbents, the concentration of dye and API pollutants were determined from the absorbance values at wavelengths corresponding to wavelength of the dye/API which was pre-determined with the help of a UV-visible spectrophotometer. A similar procedure was followed for adsorption isotherm studies, but with different initial concentrations varying in the range of 10 – 100 ppm. COD analysis of the samples was performed before and after treatment to determine the amount of organic carbon present in the samples. Known amount of solutions A and B were added to the samples and digested for 2 hours at 148 °C in a digester. After cooling, the samples were analysed in a previously programmed UV- visible spectrophotometer. The COD values were noted and % COD removal was calculated. Percentage removal and the amount of dye or API adsorbed per gram of adsorbent q_e (mg/g) was calculated as below:

$$\% \text{ removal} = \frac{(C_0 - C_e)}{C_0} \times 100 \quad (1)$$

$$q_e = \frac{(C_0 - C_e) \times V}{m} \quad (2)$$

Where C_0 (mg/L) is the initial concentration of dye or API, C_e is the equilibrium concentration of dye or API, V is the volume (L) and m (g) is weight of the adsorbent.

3. Results and Discussion

3.1 Characterization of the adsorbents

Thermogravimetric analysis was performed to understand the stability of the samples at high temperatures and to understand the optimum temperature for thermal treatment. Fig. 2 represents TGA profiles of the samples. Mass of the sample was measured at corresponding temperatures up to 900 °C in an inert atmosphere of nitrogen. From the thermogram it was observed that all the synthesised adsorbents have different degrees of stability. On an average, about 2% of moisture content was lost in the range of 50 to 100 °C for all the samples and mostly all the volatile compounds get evaporated in this temperature range¹⁷. The disintegration of organic compounds like carbohydrates and proteins can be confirmed by the abrupt weight loss in all the samples¹⁸. The mass of WA-Cu remained constant upon increasing the temperature, this may be due to copper nanoparticles present in the material

that stabilise the carbon lattice structures. The weight loss has almost been halved in the case of all other adsorbents when compared to WA200. Thermal treatment and activated charcoal modifications might be the reason for higher stability. Above 250 °C maximum weight loss of 64.61% for WA200 was observed. WAC200 undergoes degradation and observed slight ash formation above 260 °C owing to 34.17% weight loss. These observations confirm that 200 °C is optimum for activation of WA200 and WAC200. WA350, WAC350 and WA-Cu undergo modifications after a temperature 400 °C. Hence, it can be concluded that a carbonisation temperature of 350 °C is desirable for the biomass derived activated carbon.

FE-SEM analysis provided a brief idea about the surface morphologies of different adsorbents. Surface of WA200 is moderately porous in nature and also consists of various porous cavities (Fig. 3a). This might be due to the activation of the material at 200 °C. It was confirmed that after carbonisation at 350 °C the pore size and shape of WA350 have been slightly modified (Fig. 3b). In case of biomass treated with activated charcoal, pores that were almost circular in shape, undergo slight modifications due to the presence of activated charcoal resulting in the formation of cylindrical pores (Fig. 3c). The surface of WAC200 is even when compared to raw biomass. This indicated that the number of pores has reduced, which in turn may decrease the adsorption capacities. Similar observations can be made in the case of WAC350 which consists of cylindrical pores, but due to carbonisation at 350 °C the pores are a lot more defined (Fig. 3d). Heterogeneous nature and random pore size distribution of the adsorbent can be observed in the case of WA-Cu (Fig. 3e). This is a reflection of copper nanoparticles present in the material. The presence of metal ions and irregular arrangement of the pores on the surface of the adsorbent might have led to better adsorption rates.

To find the elemental composition in the samples, EDAX analysis was performed. From the results obtained, it can be confirmed that carbon composition is higher in all the adsorbents compared to other elements like oxygen, calcium, phosphorous and potassium (Table 1). At the temperature of 200 °C carbon content in WA200 is 76.20%. Later on, increasing the temperature by 150 °C, it was observed that fixed carbon content in the samples have increased by 7%, and the composition of other elements like oxygen, phosphorous and potassium have drastically reduced. This is due to the evaporation of moisture content from the samples that remove almost all the volatile compounds leaving behind high carbon content¹⁹. In case of biomass treated with activated charcoal (WAC200 and WAC350), the

carbon content is much greater when compared to WA200 due to the presence of carbon moieties in charcoal. This might be the reason for drastic reduction in the oxygen content leading to lesser adsorption capacities. Copper-modified activated carbon can be distinguished clearly from other samples containing 2.24% copper, which indicates that copper has been adhered firmly to the raw material.

Brunauer-Emmett-Teller (BET) surface area analysis is a most essential technique to understand the surface characteristics of the adsorbents. Various parameters like surface area, pore volume and pore radius which are essential for adsorption studies can be deduced (Table 2). Clearly, it is observed that WA-Cu has higher pore size when compared to all other adsorbents and might be the reason for higher decolourisation. WA200, WA350 and WAC350 adsorbents have similar surface area which result in similar adsorption capacity and removal. Copper nanoparticles have enhanced the surface area and which is an important aspect for the removal of pollutants from water.

The FTIR spectrum presented a wide range of information on surface chemistry of the adsorbents. According to the data obtained, very few peaks are observed for all the adsorbents. This can be attributed to carbonisation, during which the carbon entities are eliminated in the form of CO₂. Due to this phenomenon, the available -OH and -COOH groups are typically broken down, resulting in only trace amounts being detected.

Different XRD patterns of the adsorbents are illustrated in Fig. 4. The combination of broad and sharp peaks represents the crystalline and amorphous nature of the adsorbents. A broad peak around 20° correspond to lattice planes of amorphous carbon²⁰. Three sharp peaks around C (012), C (213) and C (241) planes attribute to crystalline graphitic carbon at 44° and 77°. The crystalline nature alone manifests high purity and efficiency in material formation²¹. Weak bands around C (200) and C (231) at 38° and 64° contribute to the orthorhombic graphitic nature of carbon (JCPDS card No. 89-8490). Small peak at (122) plane confirms the presence of copper in WA-Cu which prevails in the form of copper oxide (JCPDS card No. 49-18).

3.2 Removal of contaminants by the newer adsorbents

3.2.1 Removal of Dyes

Fig. 5 represents the % of colour removal by two different dyes, Malachite Green and Congo Red. Almost similar removal, approximately equal to 90% can be observed by all adsorbents. However, copper-modified adsorbent demonstrated a maximum dye removal of 96% for

Malachite Green and 72% for Congo Red due to its high surface area and copper content. Moreover, absorption capacity of the WA-Cu is also quite higher 48 mg/g as compared to other adsorbents (~45 mg/g). The present study showed significantly higher adsorption capacity when compared to other reported adsorbents such as *Ricinus communis* based activated carbon, having an adsorption capacity of 27.78 mg/g²², potato plant based activated carbon with an adsorption capacity of 27.0 mg/g²³ and *Pleurotus ostreatus* based activated carbon with 32.33 mg/g adsorption capacity²⁴. The adsorption capacity for WA200, WA350, WAC200, WAC350 and WA-Cu for Congo Red removal is 29.9, 33.4, 34.7, 34.1 and 36.4 mg/g respectively. Dawood et al.²⁵ reported 19.18 mg/g adsorption capacity, Namasivayam et al.²⁶ reported an adsorption capacity of 22.44 mg/g from orange peel waste, while Nunes et al.²⁷ reported 14 mg/g adsorption capacity for coffee press cake based activated carbon, which is less than the adsorption capacity of developed adsorbents. Accordingly, the adsorption capacities for the newly developed materials from wood apple pulp is higher compared to many adsorbents reported earlier (Table 3). Differences in the adsorption behaviour can be attributed to nature of the dyes and varying pore size. It is clearly observed that adsorbents modified with activated charcoal showed almost similar removal capacities and adsorption rates when compared WA200. COD removal was noteworthy in both the dyes (Fig. 7). Approximately 60% COD removal was observed in the case of Malachite Green dye and around 50% COD removal was observed in the case of Congo Red for all the adsorbents, WA-Cu being an exception owing to high COD removal of 65% and 60% in both dyes respectively.

3.2.2 API pollutant (Ciprofloxacin) removal

Fig. 7 shows CIP removal using different synthesised adsorbents. WA-Cu showed 52% removal of CIP which is greater when compared to other modified adsorbents. The adsorption capacity for CIP was found to be 8.30, 7.77, 9.93, 8.36 and 10.50 mg/g for WA200, WA350, WAC200, WAC350 and WA-Cu respectively. They are significantly higher than other reported studies such as modified coal fly ash based activated carbon which showed an adsorption capacity of 1.58 mg/g²⁸, kaolinite with 6.3 mg/g capacity²⁹ and MgO nanoparticles with an adsorption capacity of 3.46 mg/g³⁰. Presence of Cu nanoparticles on the surface of the adsorbent have enhanced the rate of adsorption in the case of copper modified adsorbent.

Owing to their efficiency, the exceptional functionalities of the developed adsorbents can be exploited in the polishing/tertiary treatment stage specifically suitable for low concentrations.

These biomass-derived adsorbents with their high adsorption capacity and excellent removal rates at their low costs, can be used for a limited number of cycles or even can be possibly utilised one time. Due to these reasons, regeneration which is employed in the case of expensive commercial adsorbents may not be required for these low-cost biomass derived adsorbents.

3.3 Adsorption isotherm study

To assess the adsorption performance, adsorption isotherm studies were performed, and Langmuir (Eq. 3) and Freundlich (Eq. 4) models were incorporated.

$$\frac{C_e}{q_e} = \frac{1}{q_{max}K_L} + \frac{C_e}{q_{max}} \quad (3)$$

$$\ln(q_e) = \ln K_F + \frac{1}{n} \ln C_e \quad (4)$$

Where, C_e (mg/L) and q_e (mg/g) are equilibrium concentration and capacity respectively, q_{max} (mg/g) is maximum adsorption capacity, K_L (L/mg) is Langmuir constant, K_F (mg/g)(L/mg)^{1/n} is Freundlich constant and n is heterogeneity factor.

Langmuir adsorption isotherm (Eq. 3) assumes monolayer adsorption on finite number of active sites for a homogeneous surface with q_{max} (mg/g) as the maximum monolayer adsorption capacity. Freundlich isotherm model (Eq. 4) accounts for multilayer adsorption on the surface. The data and the analysis on the fit of the models is given in Table 4 for all the different cases, on the removal of the dyes and CIP.

In the case of Malachite Green dye, all the adsorbents showed best fitting with Langmuir model with high linearization coefficient (R^2) values almost tending to unity. This indicates that homogeneous adsorption takes place on the surface of the material. The value of R_L for all the adsorbents lies in the range of 0-1 as per the calculations. This clearly indicates that adsorption is favourable³¹. The maximum theoretical adsorption capacity was 54.34 mg/g, which was comparable to that of experimental values (45 mg/g). Congo Red dye and Ciprofloxacin showed best fitting with Freundlich adsorption isotherm, which assumes multilayer adsorption on a heterogeneous surface. Freundlich adsorption constant K_F values are positive and high, which indicate a higher adsorption capacity³². A favourable adsorption

process requires $n > 1$ or $0 > 1/n > 1$ ³³. These findings are also supported by experimental results.

3.4 Adsorption kinetics study

The rate of uptake was determined by performing pseudo first order and pseudo second order studies. Pseudo second order data show high correlation coefficient values almost close to unity ($R^2=0.99$) and confirm that the adsorption process follows a chemisorption process³⁴. Furthermore, the maximum adsorption capacity values obtained from second order model are almost comparable to that of the experimental values (Table. 5).

3.5 Plausible mechanism of adsorption

The adsorption mechanism may be a combination of physical and chemical sorption modes. Incorporation of copper nanoparticles with biomass increased the surface area and pore size of the adsorbent leading to increase in the number of viable active sites contributing to better removal rates of the pollutant. The order of adsorption is as follows: MG > CR > CIP. The less complex structure of Malachite Green, less than the pore size in all the adsorbents owes to the higher adsorption rates when compared to other pollutant molecules like Congo Red and Ciprofloxacin which have higher degrees of complexities. FTIR analysis of the adsorbents confirmed the presence of functional groups like -OH and -COOH. Hydroxyl moieties in these groups covalently bond with the aromatic rings present in Malachite Green, which behave like H-acceptors. C=O groups present on the adsorbent surface act like e^- donors to the readily available Malachite Green molecules that act as e^- acceptors, ultimately aiding in the diffusion of the dye molecules. On the other hand, anionic dyes like Congo Red contain negatively charged ($R-SO_3^-$) groups that are electrostatically attracted to copper ions (Cu^{2+}) present on the surface of the adsorbent³⁵. Hydrogen bonding between the oxygen atoms of the biomass with cationic amine groups of CIP might have led to adsorption of these molecules from the aqueous solution³⁶. Altogether, the adsorption of the dye and API molecules might include various mechanisms like: (i) pore filling (ii) hydrogen bonding (iii) electrostatic interactions.

Conclusions

Newer modified biomass-derived adsorbents prepared from wood apple pulp biomass demonstrate versatility and potential in the removal of organic dyes and API pollutants. These adsorbents exhibit high efficacy even at a very low adsorbent dosage of 0.1%. All the adsorbents including modified activated carbons, copper modified adsorbents and raw biomass showed high efficiency in the removal of Malachite Green and Congo Red dyes, with impressive adsorption capacities of 48 mg/g and 36 mg/g respectively, is higher than several reported adsorbents. The equilibrium data reveals a good fit with Langmuir isotherm for Malachite Green and Freundlich isotherm in the case of Congo Red and Ciprofloxacin. Furthermore, pseudo second order kinetic model was utilised successfully to predict rates of the reaction. The results clearly highlight the potential for the use of biomass derived adsorbents in wastewater treatment, for the removal of organic pollutants from water.

Acknowledgement

VMB would like to acknowledge the funding for the research from Department of Science and technology, The Ministry of Science and Technology India, (DST/TM/WTI/WIC/2K17/100(G)) and also Council of Scientific and Industrial Research (CSIR), Government of India (MLP102326).

Figures:

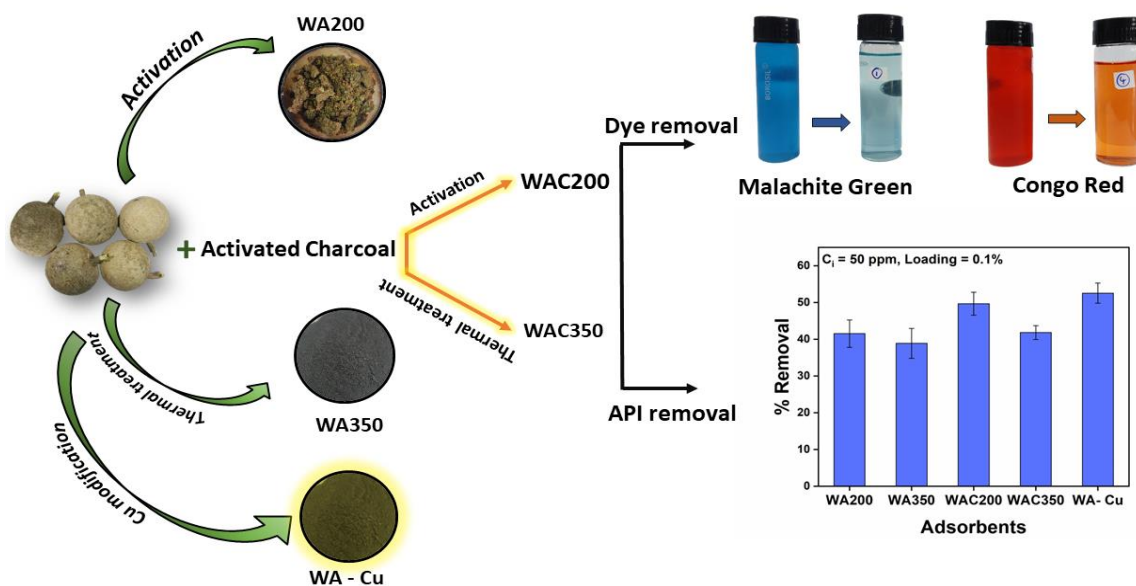


Fig. 1 Steps involved in the preparation of adsorbents

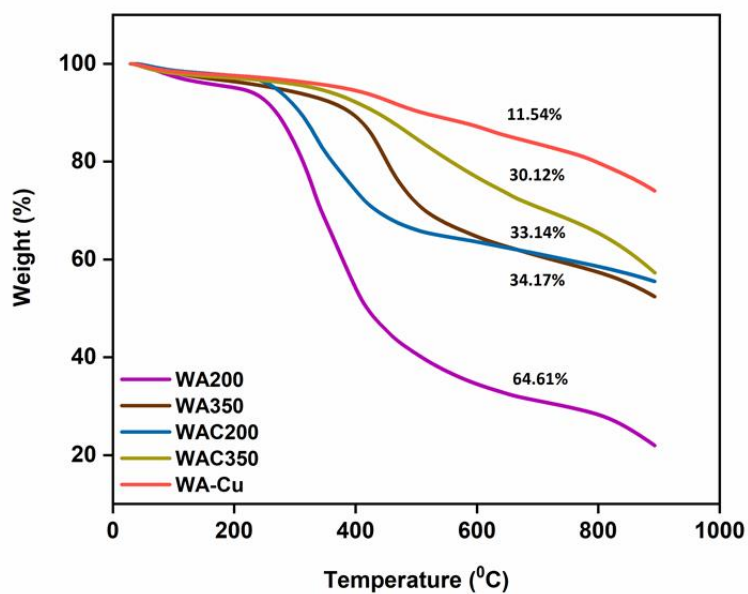


Fig. 2 TGA profiles of the adsorbents

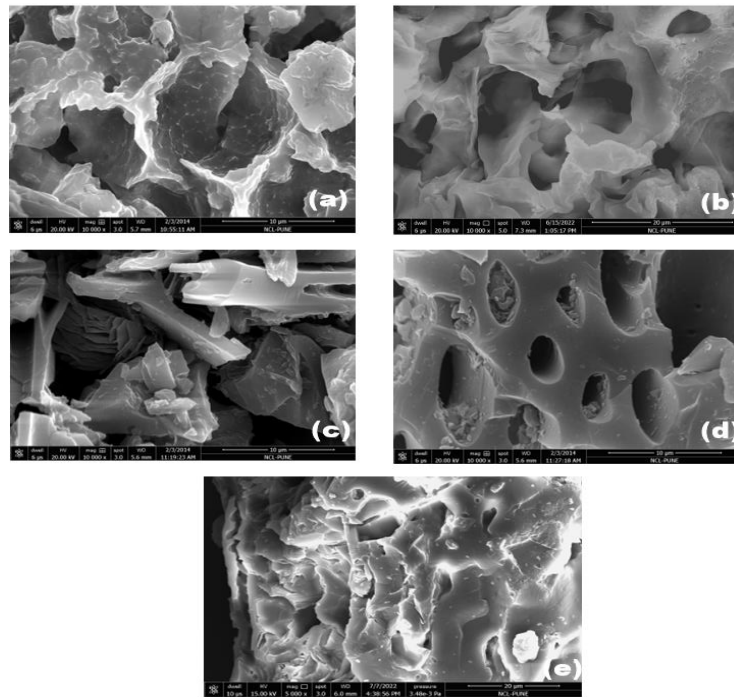


Fig. 3 FESEM images of different adsorbents, surface morphology of (a) WA200 (b) WA350 (c) WAC200 (d) WAC350 (e) WA-Cu

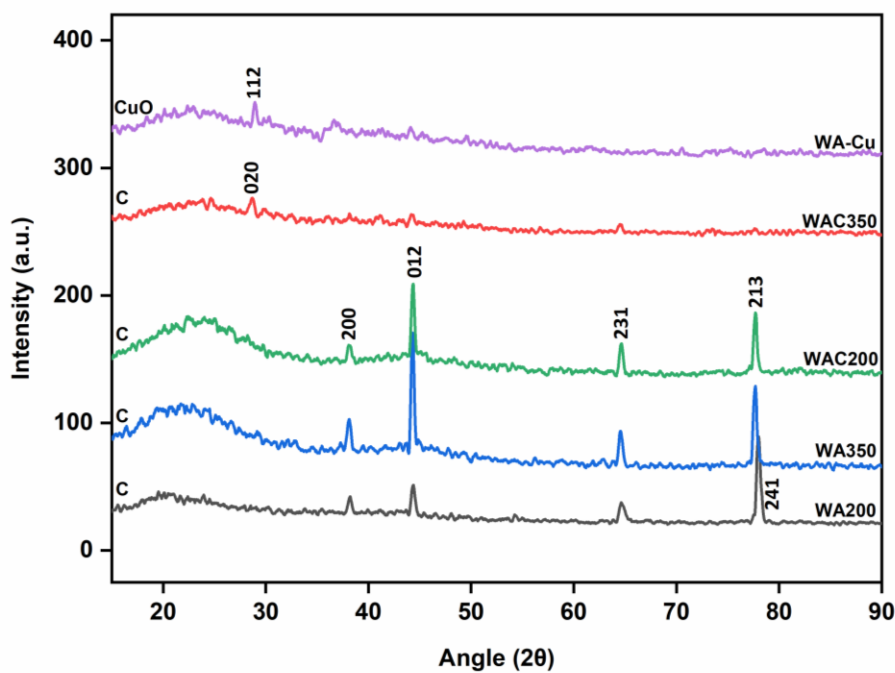


Fig. 4 XRD patterns of the adsorbents

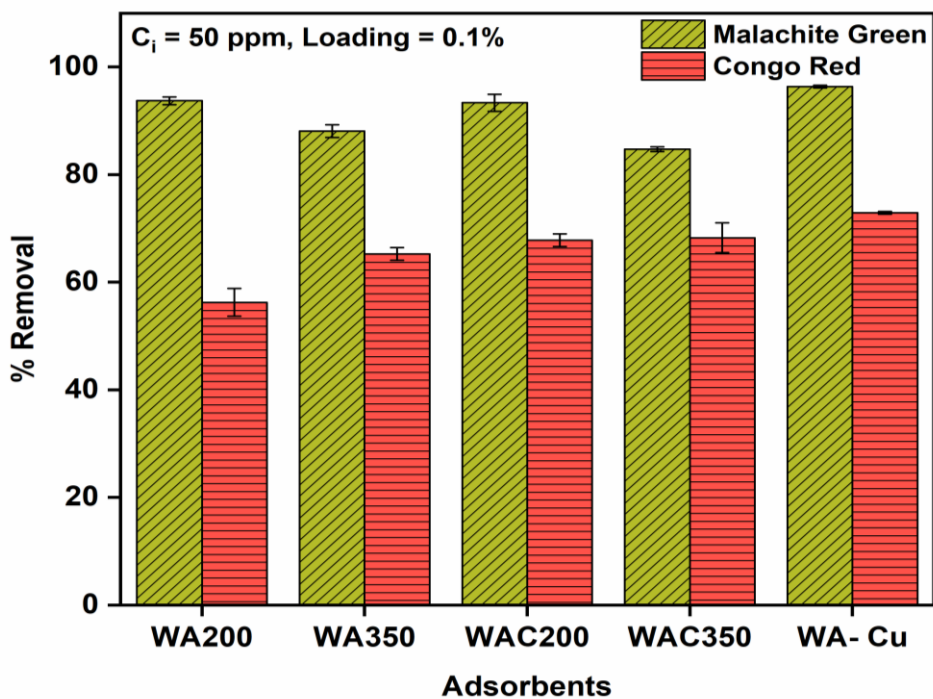


Fig. 5 Comparison of % Color removal for dyes

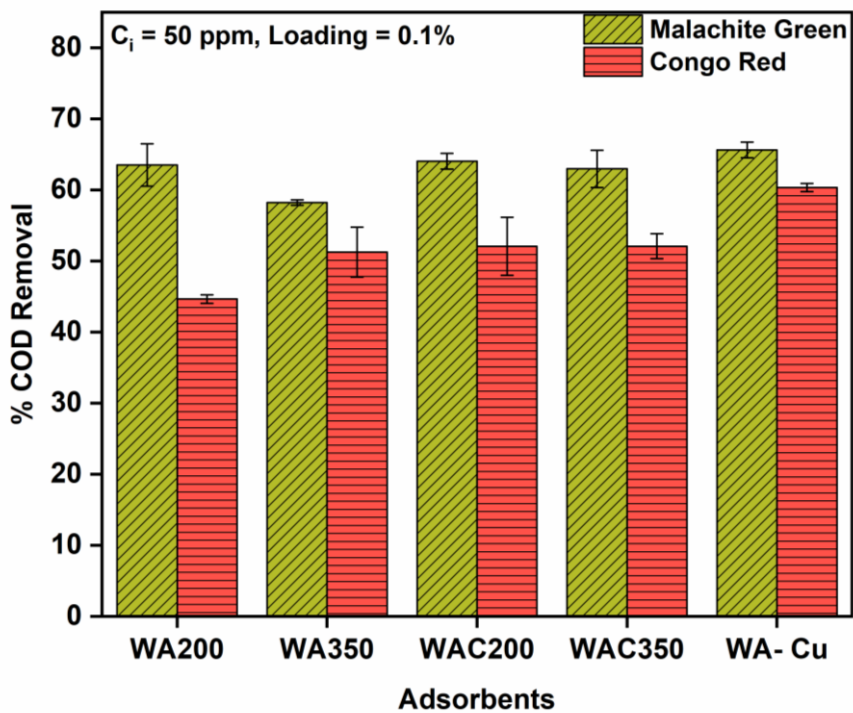


Fig. 6: Comparison of % COD removal for dyes

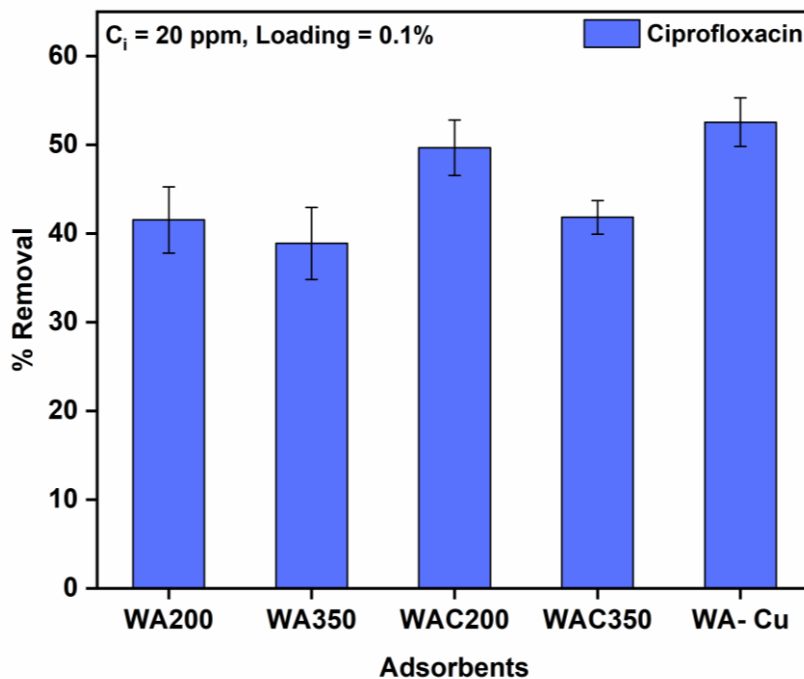


Fig. 7: % Removal of Ciprofloxacin

Tables:

Table 1: Elemental composition of the adsorbents

Element	Composition (at%)				
	WA200	WA350	WAC200	WAC350	WA-Cu
C	76.20	87.69	94.26	82.02	82.41
O	22.37	12.05	05.10	13.79	15.92
Ca	0.16	0.28	0.27	2.67	-
P	0.30	0.09	0.12	0.20	-
K	0.78	0.17	0.10	0.74	1.02
Cu	-	-	-	-	2.24

Table 2: Surface characteristics of adsorbents: Surface area and Pore size

Adsorbent	Surface area (m ² /g)	Pore volume (cc/g)	Pore radius (Å)
WA200	17.95	0.032	16.5
WA350	15.07	0.024	18.5
WAC200	23.30	0.055	16.6
WAC350	13.92	0.020	17.5
WA-Cu	33.31	0.022	15.6

Table 3: Comparison of adsorption capacity with different adsorbents

Material	Pollutant (Dye/CIP)	Adsorption Capacity (mg/g)	References
Ricinus communis based activated carbon	MG	27.78	²²
Potato plant waste	MG	27.0	²³
<i>Pleurotus ostreatus</i>	MG	32.33	²⁴
Tamarind fruit shell	MG	1.95	³⁷
Raw pine cone	CR	19.18	²⁵
Waste orange peel	CR	22.44	²⁶
Coffee press cake	CR	14	²⁷
<i>Aspergillus Niger</i>	CR	14.16	³⁸
Modified coal fly ash	CIP	1.58	²⁸
Kaolinite	CIP	6.3	²⁹
MgO nanoparticles	CIP	3.46	³⁰
WA-Cu	MG	48	This work
WA-Cu	CR	36.4	This work
WA-Cu	CIP	10.5	This work

Table 4: Adsorption isotherm parameters and fit of the model

		Isotherms					
		Langmuir			Freundlich		
Adsorbent	Dye/ API	q_{max} (mg/g)	K_L (L/mg)	R^2	K_F (mg/g) (L.mg) ^{1/n}	n	R^2
WA200	MG	51.54	0.89	0.97	18.51	3.04	0.95
	CR	2.30	26.48	0.98	3.15	1.45	0.99
	CIP	1.69	9.25	0.85	1.66	1.52	0.93
WA350	MG	53.19	0.86	0.97	18.45	3.01	0.96
	CR	2.56	16.37	0.85	2.56	1.37	0.94
	CIP	1.95	6.94	0.77	1.77	1.61	0.90
WAC200	MG	40.81	1.18	0.96	17.90	2.98	0.93
	CR	3.58	10.68	0.93	4.13	1.72	0.98
	CIP	1.57	9.88	0.83	1.56	1.49	0.90
WAC350	MG	54.34	0.88	0.97	19.36	3.15	0.94
	CR	3.54	11.20	0.91	3.88	1.63	0.97
	CIP	1.96	6.82	0.77	1.76	1.61	0.90
WA-Cu	MG	33.33	2.27	0.92	21.85	2.54	0.73
	CR	2.92	14.40	0.90	3.19	1.49	0.96
	CIP	1.74	8.55	0.82	1.69	1.55	0.92

Table 5: Kinetic model parameters and fit of the model

		pseudo first order				pseudo second order		
Adsorbent	Dye/CIP	q_{exp} (mg/ g)	q_{thr} (mg/g)	k_1 (min ⁻¹)	R^2	q_{thr} (mg/g)	k_2 (g/mg/min)	R^2
WA200	MG	46.8	25.73	0.001	0.89	48.30	0.005	0.99
	CR	29.9	1.88	0.001	0.36	42.73	0.003	0.99
	CIP	8.30	0.92	-1.72E-05	0.58	13.17	0.008	0.99
WA350	MG	44.0	15.42	0.0006	0.39	47.16	0.003	0.99

	CR	33.4	12.05	0.0005	0.70	38.46	0.002	0.99
	CIP	7.77	1.47	8.82E-05	0.28	13.44	0.074	0.98
WAC200	MG	46.6	9.09	0.0009	0.79	50.00	0.004	0.99
	CR	34.7	13.00	0.0005	0.85	39.52	0.002	0.98
	CIP	9.93	0.93	0.0013	0.82	13.17	0.008	0.99
WAC350	MG	42.3	12.84	0.0006	0.42	48.54	0.005	0.99
	CR	34.1	242.08	0.0012	0.81	38.02	0.008	0.99
	CIP	8.36	2.17	0.0004	0.62	14.74	0.004	0.97
WA-Cu	MG	48.1	20.28	0.0058	0.95	49.01	0.004	0.99
	CR	36.4	4.70	0.0004	0.78	37.45	0.011	0.99
	CIP	10.5	5.38	0.0003	0.92	10.26	0.009	0.98

References

1. K. Balapure, V.M. Bhandari, J. of ISAS 2,3, 2023.
2. R. Gothwal, T. Shashidhar, Clean Soil Air Water 43, 479, 2015.
3. V. V. Ranade V.M. Bhandari, Industrial Wastewater Treatment, Recycling and Reuse. Elsevier, 06975, 2014.
4. O.A.A, Eletta, S.I. Mustapha, O.A. Ajayi, A.T. Ahmed, Niger. J. Technol. Dev. 15, 26, 2018.
5. K. Sharma, M. Chethana, V.M. Bhandari, Sorokhaibam, Laxmi Gayatri, V.V. Ranade, D.J. Killedar, J. ISAS 1, 3, 2023.
6. O.S. Bello, M.A. Ahmad, Sep Sci Technol 47, 903, 2012.
7. A. Sharma, Z.M. Siddiqui, S. Dhar, P. Mehta, D. Pathania, . Sep. Sci. Technol. 54, 916, 2019.
8. T.A. Gad-Allah, M.E.M, Ali, M.I. Badawy, J. Hazard. Mater. 186, 751, 2011.
9. S. Shi, Y. Fan, Y. Huang, Ind. Eng. Chem. Res. 52, 2604, 2013.
10. L.G. Sorokhaibam, V. M. Bhandari, M.S. Salvi, J. S. jain, S.D. Hadawale, V.V. Ranade Ind. Eng. Chem. Res. 54, 11844, 2015.
11. A.A. Ahmad, A.T.M, N.K.E. Din Yahaya, M.A., A. Khasri, M.A. Ahmad, Arab. J. Chem.13, 6887, 2020.
12. N.K. Mondal, S. Kar, Appl. Water Sci. 8, 157, 2018.
13. S. Lahreche, I. Moulefera, A. El Kebir, L. Sabantina, M. Kaid, Benyoucef, A. Fibers,

- 10, 7, 2022.
14. P.E. Jagadeesh Babu, V. Kumar, R. Visvanathan, *J. Chem. Eng.* 5, 465, 2009.
 15. T.T. Dao, T. Hong-tham T. Nguyen, C.N. Duyen Thi, T.N. Hanh , H. T.T. Nguyen, S.Y. Trung Do, L.O.C, Huu, T.T. Nguyen, T.D. Nguyen, L.G.bach, *Cellul. Chem. Technol.* 54, 811, 2020.
 16. R.A. Teixeira, E.C. Lima, A.D. Benetti,P. Thue, R. N, Mohamed, A. aved. *Environ. Sci. Pollut. Res.*2022.
 17. N.S. Kumar, H. M. Shaikh, M. Asif, E.H. Al-Ghurabi, *Sci. Rep.* 11, 2586, 2021.
 18. S. Prashanth, C. Subramaniam, Bharatwaj, N. R. Akshykumar, K. Nithya, *Int. J. Environ. Sci. Technol.* 19,1247, 2022.
 19. M.F. Mohamad Yusop, M.A. Ahmad, N.A. Rosli, N. Gonawan, Abdullah, S.J. *Malaysian J. Fundam. Appl. Sci.* 17, 95, 2021.
 20. A.H. Wazir, I.U. Wazir, A.M. Wazir, *Energy Sources, Part A: Recovery Utility Environ. Effects*, 1, 2020.
 21. M. Shahrashoub, S. Bakhtiari, *Microporous Mesoporous Mater.* 311, 110692, 2021.
 22. T. Santhi, S. Manonmani, T. Smitha, *J. Hazard. Mater.* 179, 178, 2010.
 23. N. Gupta, A. K. Kushwaha, M.C. Chattopadhyaya, *Arab. J. Chem.* 9, 707, 2016.
 24. Z. Chen, H. Deng, C, Chen, Y. Yang, Xu, H.J. *Environ. Heal. Sci. Eng.* 12, 1, 2014.
 25. S. Dawood, T.K. Sen, *Water Res.* 46, 1933, 2012.
 26. C. Namasivayam, N. Muniasamy, K. Gayatri, M. Rani, K. Rangnathan *Bioresour. Technol.* 57, 37, 1996.
 27. A.A. Nunes, A.S. Franca, L.S. Oliveira, *Bioresour. Technol.* 100, 1786, 2009.
 28. C.L. Zhang, G.L. Qiao, F. Zhao, Y. Wang, *J. Mol. Liq.* 163, 53, 2011.
 29. Z. Li, H. Hong, L. Liao, Ackley, C.J., Schulz, C.J, schulz, L.A, MacDonald, R. Mihelich, A.L, Emard, S. M. *Colloids Surfaces B Biointerfaces* 88, 339, 2011.
 30. N. Khoshnamvand, S. Ahmadi, F.K. Mostafapour, *J. Appl. Pharm. Sci.* 7,79, 2017.
 31. G.M. Yalvaç, B. Bayrak, *Desalin Water Treat* 177, 176, 2020.
 32. O. Tunç, H. Tanac, Z. Aksu, *J. Hazard. Mater.* 163, 187, 2009.
 33. W. Konicki, M. Aleksandrak, D. Moszyński, E. Mijowska, *J. Colloid Interface Sci.* 496,188, 2017.
 34. S.A. Patil, U.P. Suryawanshi, N.S. Harale, S.K. Patil, Vadiyar, S.K, Luwang, M.N, Anuse, Kim, J.H., S.S. Kolekar, . *Int. J. Environ. Anal. Chem.* 1, 2020.
 35. E. Sharifpour, E. Alipanahpour, A. Asfaram, Ghaedi, M, Goudarzi, A. *Appl. Organomet. Chem.* 33, 4768, 2019.

36. A. Maged, S. Kharbish, I.S. Ismael, A. Bhatnagar, *Environ. Sci. Pollut. Res.* 27, 32980, 2020.
37. P. Saha, S. Chowdhury, S. Gupta, Indresh, K. *Clean Soil Air Water* 38, 437, 2010.
Y. Fu, T. Viraraghavan, *Adv. Environ. Res.* 7, 239, 2002.

Comparing The Catalytic Activity of Mg-BTC Metal Organic Framework and Post Synthetically Modified (TiO₂ @ Mg-BTC) Metal Organic Framework for Cyanosilylation of Aldehydes

S. Santhana Laxmi¹ and K. Usha Nandhini^{2*}

¹ Department of Chemistry, Meenakshi College for Women, Chennai 600 024, India.

^{2*} Department of Chemistry, Queen Mary's College, Chennai 600 004, India.

*Email: kusha.chem@gmail.com

Received: 20.9.2023, Revised: 18.3.2024, 9.4.2024, Accepted: 12.4.24

Abstract

Metal–organic frameworks (MOFs) are an emerging class of porous crystalline hybrid materials synthesised by the coordination of inorganic connectors and organic linkers, which has numerous potential applications in various fields. Here we report a comparative study on Mg-BTC MOF and TiO₂@Mg-BTC MOF as a heterogeneous catalyst. Mg-BTC MOF was synthesised by solvothermal method and subjected to comparative study with its post synthetically modified (PSM) counterpart to understand their catalytic behaviour for cyanosilylation of aldehydes. The synthesised Mg-BTC MOF and TiO₂@Mg-BTC MOF were characterised by powder XRD, BET surface area, SEM, FT-IR, TGA techniques. A detailed characterization study was performed to understand the correlation between catalytic activity and morphology of the assynthesized MOF and PSM-MOF. The catalytic activity of the hybrid materials were evaluated by GC-MS analysis. The results of the catalytic reactions revealed that post synthetically modified (TiO₂@Mg-BTC) MOF exhibited significantly higher catalytic activity compared to Mg-BTC MOF. The enhanced catalytic efficiency is due to the incorporation of TiO₂ nanoparticles, which provides active sites for catalytic reactions under heterogeneous conditions. Even after repeated recycling and reuse, the catalytic ability of the catalyst retains. The impact of TiO₂ on the framework shows variation in texture, surface area, thermal stability and catalytic behaviour on the MOF materials. Thus, our study emphasizes the cogency of catalytically active MOFs as a heterogeneous catalyst and demonstrates the simple and effective way for the practical synthesis of fine compounds using them.

Paper presented during 3rd International Conference on Recent Trends in Analytical Chemistry (26-28 June 23) organized by Department of Analytical Chemistry, University of Madras, Chennai and ISAS Tamilnadu Chapter

Key words: MOFs, Post Synthetic Modification, Catalyst, Hybrid materials, Cyanosilylation of Aldehydes.

Introduction:

Metal-organic frameworks (MOFs) are crystalline materials assembled themselves by the coordination of ligands and metal clusters¹. These materials have attracted tremendous scientific attention during last few decades, not only driven by their highly tuneable structures but also motivated by their potential applications in the fields such as catalysis², electronics, gas storage and selective separation^{3,4}, drug delivery⁵, detoxification⁶, proton conductivity⁷, energy storage⁸, sensing and lighting^{9,10} and among various fields.

Besides these useful properties, few MOFs are hindered by the physical and their chemical constraints resulting in poor performance¹. By changing the metal atom, ligand character, ligand functionality, and synthesis environment, several porous compounds with diverse features, properties, and applications were synthesised. The structure and subsequently the characteristics of the synthesised MOFs are largely determined by the selection of the metal and linker¹¹. Because of their distinct topology and tuneable features, metal organic frameworks continue to be a fascinating subject of research¹². The majority of metal-organic frameworks (MOFs) on the market today are made from 3d or 4f metals, although there has been a recent uptick in interest in MOFs made from light main group elements like Li, Be, B, Mg, Al, or In¹³.

Researchers on alkaline earth metals are limited, notably the Mg-based MOFs, which have been relatively less explored while being regarded as equally important as those focusing on other metals due to their co-ordination behaviour¹⁴. Mg(II) cations have a strong tendency to co-ordinately bind water molecules, which contributes to their sensitivity to moisture and therefore their instability. It can appear that the alkaline earth metals are less intriguing due to their lack of fundamentally beneficial distinctive properties. However, the alkaline earth metals offer other benefits such as their abundancy, low cost, low weight, and lack of toxicity. Various recent studies have been reported which concerns on only alkaline earth metals and their complexes deserve to be cited here¹⁵. MOFs synthesised by Mg²⁺ plays an

important role in exhibiting catalytic activity, their large surface area, low framework density, and malleable shape, etc.¹⁶

Post-synthetic modifications (PSMs) have indeed opened up new possibilities for the application of MOFs in various fields. By performing PSM on MOFs, researchers can tailor their properties and functionalities to meet specific application requirements. To ensure successful post-synthetic modifications (PSMs), it is crucial to prevent the degradation of MOFs throughout the entire reaction and maintain their integrity. Among the various methods for PSM, modifying the linker (ligand) or modifying the metallic node are commonly preferred approaches. Additionally, the adsorption or exchange of guest species is also widely employed. To enable the introduction of desired properties and increase the stability of MOF structures, modifying the surface environment of MOFs is a viable approach. One such method is metal incorporation, also known as metal doping. Metal doping is the process of introducing a new metal ion or metal complex into a pre-existing MOF structure. This can be achieved by directly coordinating the metal at specific sites within the framework or by including metal ions into the open channels of the MOF.

Inspired by the catalytic properties of nanomaterials demonstrated in the work of Rajendran et al and Sridharan et al^{17,18}, our study aims to explore the introduction of TiO₂ nanoparticles through post synthetic modifications. Recent advancements in nanotechnology have led to the development of highly efficient nanomaterial based catalysts, as highlighted by Chandra kishore et al¹⁹, paving way for our current research endeavours.

This study presents a comprehensive comparison of the catalytic activity of the synthesised Mg-BTC MOF and its post synthetically modified counterpart. Through meticulous analysis of reaction yields and catalytic efficiencies, our findings shed light on the superior performance of TiO₂ @ Mg-BTC MOF in promoting the cyanosilylation of aldehydes. This investigation not only contributes to our understanding of MOF-based catalysis but also underscores the potential of post synthetic modification.

Experimental

Materials

Magnesium (II) nitrate hexahydrate [96 %, Mg (NO₃)₂.6H₂O, Sigma Aldrich,], Benzene 1,3,5 tricarboxylic acid [BTC, Sigma Aldrich, C₉H₆O₆, 95%]. Deionized (DI) water, N, N-dimethylformamide (HCON(CH₃)₂) and ethyl alcohol anhydrous (C₂H₅OH, Merck 99.9%), were utilised in the catalyst preparation as solvents. There was no additional purification of the cyanosilylation chemicals because they were all of analytical grade.

Synthesis of catalysts

Synthesis of Mg-BTC MOF catalyst

In a solvent combination of 125 ml comprising water, ethanol, and DMF in a ratio of 1:1:1, 0.5 mmol of Mg (NO₃)₂.6H₂O and 1 mmol of BTC were added. A magnetic stirrer was used to agitate the liquid for two hours. Then, without stirring, the mixture was kept in a stainless-steel autoclave coated with teflon and heated to 393 K. After 48 h the autoclave was cooled to room temperature at a rate of 278 K per hour. Colourless crystals were obtained which was then collected by filtration and washed with DMF and dried at 353 K for 5 h in an oven. The yield of the as synthesized catalyst was found to be 85 % based on Mg(NO₃)₂.6H₂O.

Post synthetic modification of Mg-BTC catalyst

The growth of TiO₂ nanoparticles on the synthesised MOF is based on the procedure followed by Hu et al²⁰. 500 mg of the synthesised MOFs were air-dried at a temperature of 150°C for at least 5 h. Then it was added to the solution of 20 ml titanium (IV) butoxide and 26 ml ethyl alcohol. After sonicating the solution for 30 minutes, it was stirred for another 30 minutes. The solution was centrifuged at 4000 rpm for 20 minutes after 12 h and then the residue was washed with ethanol. The mixture was left in air for 48 h before being poured into a 250 ml teflon container containing 170 ml deionized water. A stainless-steel autoclave was then used to subject the system to air heating at 150 °C for 10 h. A solid was recovered by centrifugation and air-dried at 80°C for 72 h after cooling to ambient temperature. The titania-modified samples were designated as TiO₂@Mg-BTC MOF.

Physicochemical properties

SEM, TGA, FT-IR, PXRD and BET surface area were all employed to characterise the porous metal organic framework. Gas chromatography (GC) was used to separate the by-products of the catalytic process, and GC-MS was used to identify the products.

The crystalline structure of the material was analysed using a Bruker D8 advance powder X-ray diffraction instrument, employing Cu – K α radiation ($\lambda = 0.154$ nm) with an operating voltage of 40 KV and a current rating of 30 mA. Diffractograms were captured over a 2 θ angle range, spanning from 0 to 70, with a step size of 0.02° and a count time of 10 s. To investigate the morphological characteristics of the catalysts, nitrogen adsorption at 77 K was employed, utilizing a Quanta Chrome NOVA 1000 surface analyser. Prior to testing, the samples underwent a degassing process at 573 K for 4 h to eliminate any residual moisture or adsorbed gases. The analysis employed the BET technique to quantify nitrogen adsorption,

and the BJH technique to determine cumulative volume and pore diameter based on desorption isotherms. The FT-IR spectra of the materials were acquired by utilizing KBr pellets and a Perkin Elmer Spectrum One FT-IR spectrometer, featuring a standard resolution of 1.0 cm^{-1} and spanning the spectral range from 450 cm^{-1} to 4000 cm^{-1} . To evaluate the stability of the synthesized material, thermogravimetric analysis was performed using a TGA (Perkin Elmer) Q500 Hi-Res TGA thermal analyser.

For a detailed examination of the morphology of the synthesized MOF material, scanning electron microscopy (SEM) was employed. SEM analysis was conducted using the Supra Zeiss equipment, operating at 30 KV, and equipped with a 20 mm Oxford Energy Dispersive X-ray Spectroscopy (EDS) detector. The MOF sample was allowed to air-dry at room temperature after being deposited from an ethanol solution onto a silicon plate.

Catalytic studies

Liquid-phase cyanosilylation of aldehydes with trimethyl silyl cyanide (TMSCN) was performed. A 50 ml round bottomed flask equipped with a reflux condenser was charged with aldehyde (1 mmol), TMSCN (2 mmol), pentane solvent (15 ml), and the as-synthesised catalysts (5% w.r.t. aldehyde). The flask's contents were magnetically swirled while being heated to 343 K in an oil bath. At certain intervals, aliquots of the heated mixture were taken out to see how things were doing with the reaction. To analyse the liquid products obtained, a procedure was followed. Initially, 10 ml of diethyl ether was added to the reaction mixture, and then the mixture underwent centrifugation. The liquid products were subsequently characterized using GC.

In this study, a Clarus 680 GC instrument was employed, equipped with a merged silica column packed with Elite-5 MS (composed of 5% biphenyl and 95% dimethyl polysiloxane), measuring 30 meters in length, 0.25 millimetres in diameter, and 250 meters in film thickness. The separation of components was achieved at a constant flow rate of 1 ml/min, with helium serving as the carrier gas. To identify the products precisely, GC-MS (Gas Chromatography-Mass Spectrometry) analysis was employed, utilizing a Perkin-Elmer instrument. The mass of the products was determined using a Clarus 600 (EI) turbo mass spectrometer with an electron impact energy of 70 electron volts (70eV). The compounds in the samples were determined by comparing their spectral data to the NIST-2008 library, which has a database of spectra for all known substances.

Results and Discussion :

Characterisation of the catalyst.

X-ray diffraction is a reliable technique for probing the crystallinity of the synthesized material. Fig.1a displays the XRD pattern obtained from Mg-BTC MOF. Figure 1a and 1b display the X-ray diffraction (XRD) patterns obtained during the analysis. The diffraction lines observed at 2θ angles approximately 11.54° , 14.74° , 19.15° , 22.00° , 24.05° , 27.39° , 30.69° and 39.14° have been identified and associated with specific crystal planes of the Mg-BTC MOF. These planes correspond to the (111), (210), (220), (311), (320), (410), (420) and (522) crystallographic planes, respectively. The highest intensity peak is observed at 2θ 27.39° . Fig.1b represents the PXRD pattern for TiO_2 @Mg-BTC MOF. Bragg's Diffraction peaks are observed at 2θ 's 15.84° , 18.75° , 22.04° , 23.81° , 25.29° , 26.96° , 28.89° , 29.11° , 30.16° , are associated with (210), (220), (311), (320), (321), (400), (330), (331), (420) respectively are crystal planes of TiO_2 @ Mg-BTC MOF. Additional diffraction lines were observed at 2θ angles of 15.84° , 25.29° , 26.96° , 28.89° , and 29.11° following the deposition of TiO_2 onto the MOF. These new diffraction lines can be attributed to the presence of specific crystal planes of rutile, which include the (210), (220), and (321) crystal planes. This observation suggests the successful growth of TiO_2 on the Mg-BTC MOF, leading to the appearance of these rutile-related diffraction patterns²⁰. From the XRD pattern it is evident that the TiO_2 was fully dispersed on the MOF material and there is no structural damage even after the growth of TiO_2 . Anatase was found to be the dominant crystalline phase in the pure TiO_2 sample (XRD pattern not shown), consistent with prior research²¹⁻²⁴. Scherrer's equation was employed to determine the mean crystallite size (D) using X-ray line broadening (1)²⁵,

$$D = \frac{0.9\lambda}{\beta_{1/2} \cos\theta} \quad (1)$$

Where

θ - Bragg's angle

λ - wavelength of the X-ray

$\beta_{1/2}$ - angular width at the half maximum intensity

Table 1 displays the crystallographic data validated by EXPO 2014 software for the synthesised materials.

Fourier Transform infrared analysis of the synthesized materials are presented in Fig.2a represents the Mg-BTC MOF. The broad absorption band around 3000 cm^{-1} to 3200 cm^{-1} is due to AR-H stretching vibrations of the benzene tricarboxylic acid, the bands

at 1608 cm^{-1} and 1374 cm^{-1} are assigned as residue of C=O asymmetric and symmetric stretching vibrations originating from the C=O of 1,3,5 benzene tricarboxylic acid. The FT-IR of $\text{TiO}_2@\text{Mg-BTC}$ MOF in Fig 2b show weak absorption band in the region 3100 cm^{-1} is due to aromatic C-H stretching vibrations originating from the 1,3,5 benzene tricarboxylic acid. The bands at 1694 cm^{-1} are assigned as residue of C=O asymmetric and symmetric stretching vibrations originating from the C=O of 1,3,5 benzene tricarboxylic acid. Additionally absorption band at 1269 and 1091 cm^{-1} can be assigned to O-C=O symmetric and asymmetric stretching vibration and C-O stretching vibrations of unreacted BTC. The bands observed from 600 to about 950 cm^{-1} have been assigned to Ti-O bonds^{26, 27}. The features at 1397 cm^{-1} and 1399 cm^{-1} are associated with the bending modes of CH_3 and CH_2 groups²⁸ respectively. These bands can be related to ethanol or dimethyl formamide used to synthesise the MOF matrices and TiO_2 nanoparticles. It is shown that in $\text{TiO}_2@\text{Mg-BTC}$ MOF, the absorption bands attributed to Ti-O bonds are so strong that the bands related to Mg-BTC MOF from 500 to 600 cm^{-1} are barely visible.

Surface area of the materials $\text{TiO}_2@ \text{Mg-BTC}$ and Mg-BTC MOFs was found to be $375\text{ m}^2/\text{g}$ and $893\text{ m}^2/\text{g}$ respectively. Significant changes in specific surface area A_{BET} , pore volume V_p , and pore diameter d_p occur when titanium is included in the frameworks. The decrease in surface area of the $\text{TiO}_2@\text{Mg-BTC}$ MOF is due the presence of TiO_2 nanoparticles on the pores of the Mg-BTC frameworks. Table 2 displays the synthesised MOFs' textural characteristics. The morphologies and the microstructure of the synthesized MOF materials were investigated by scanning electron microscopy (SEM).The SEM micrograph Fig 3(a) shows distribution of particles in Mg-BTC MOF as needle like crystals. A magnification at $30\mu\text{m}$ confirm these needles as irregular rod like particles. The SEM images of $\text{TiO}_2 @ \text{Mg-BTC}$ MOF Fig 3(b) shows the distribution of TiO_2 particles in Mg-BTC MOF. It exhibits an irregular morphology, which is similar to the shape of previously reported PSM MOFs in the literature²⁰.

Thermogravimetric analysis (TGA) showed that the temperature in the limits of $25\text{-}800^\circ\text{C}$ increase at 10°C per minute when exposed to a N_2 environment. Weight loss of 15% was observed after 200°C in the TGA result of the synthesised Mg-BTC MOF (see Figure 4), which corresponds to the loss of water and ethanol molecules. At temperatures over 400°C , Mg-BTC MOF decomposed into metal oxide and lost its structural integrity. According to the results, the Mg-BTC MOF framework was highly stable at temperatures below 500°C ^{20,29}. While in the case of **$\text{TiO}_2@ \text{Mg-BTC}$ MOF, the material shows very little weight loss of 2 to 5% throughout the heating process, from which it is obvious that there is no**

significant weight loss and the post synthetically modified material remains unchanged even at 800°C, which is probably due to TiO₂ doping. Thus **TiO₂@Mg-BTC MOF shows extra ordinary thermal stability over Mg-BTC MOF.**

Catalytic Studies of Mg-BTC and TiO₂ @ Mg-BTC MOFs.

The catalytic activity of the synthesised materials for cyanosilylation of aldehydes was explored by using 5 wt% of MOF w.r.t aldehydes. Specifically, the study focused on examining the catalytic potential of Mg-BTC MOF for cyanosilylation of aromatic aldehydes due to its uniformly dispersed Lewis acid sites and the porous structure present throughout its entire framework³⁰. Cyanohydrin formation through the addition of cyanide to carbonyl compounds is a fundamental C-C bond-forming reaction in organic chemistry and has played a pivotal role in various chemical advancements^{31, 32}. As such, the catalytic capabilities of both Mg-BTC MOF and TiO₂@Mg-BTC MOF were assessed for their ability to facilitate the reaction between trimethylsilyl cyanide (TMSCN) and benzaldehyde, as well as various substituted benzaldehydes.

The results, as depicted in Table 3, revealed that compared to TiO₂@Mg-BTC MOF, Mg-BTC MOF exhibited significantly lower catalytic activity in this reaction, resulting in a notably reduced yield. The incorporation of titanium dioxide (TiO₂) nanoparticles into MOF structure leads to a significant enhancement in catalytic performance. The synergetic interaction between TiO₂ nanoparticles and the MOF framework not only increases the active sites available for catalysis but also promotes improved mass transport and stability, rendering TiO₂ doped MOFs as highly effective catalyst for cyanosilylation reaction¹⁹. It was also observed that the presence of different substituents around the benzylic portion of the benzaldehyde backbone influenced the reaction yields, indicating the impact of electronic effects and steric hindrance. For instance, yields of 87% and 89.7% were obtained for 4-methoxybenzaldehyde and 4-hydroxybenzaldehyde, while the yield for 4-nitrobenzaldehyde reached 98%³³. This suggests that substrates functionalized with electron-withdrawing groups are more inclined to react in this context. Schematic representation of the cyanosilylation of aldehydes is shown in scheme 1.

Reusability of the catalyst.

A catalyst recycling test was carried out at 80°C to assess the long-term durability of the synthesised catalysts in the liquid phase reaction. The filtered-out, utilised catalyst samples were washed with diethyl ether and air-dried for 24 h. After each run, the catalysts were reactivated at 80°C in air oven for two hours before being utilised again. Figure 5 displays the outcomes of para nitro benzaldehyde conversion. Other substrates also showed similar

behaviour. The yield of the product obtained demonstrates that both catalysts shows considerable reduction in their catalytic activity. However, no abrupt change was observed, which confirms that Mg-BTC MOF and TiO₂@Mg-BTC MOF are stable and efficient heterogeneous catalysts for chemical transformations.

Conclusion :

In summary, we have synthesized Mg-BTC MOF and TiO₂@Mg-BTC MOF and demonstrated that the synthesized materials are a highly potential heterogeneous catalyst for cyanosilylation of aldehydes. Under heterogeneous circumstances, the catalytic process shows great selectivity and good yields. The catalytic activity of the synthesised materials are maintained even after repeated recycling and reuse. Our work thus shows the easy and efficient method for practical synthesis of fine chemicals via catalytically active MOFs and highlights their efficiency as a heterogenous catalyst. Our future research is dedicated to exploring the impact of post-synthetic modifications on the catalytic properties of our synthesized MOF materials and assessing their potential to compete with established industrial catalysts. We aspire to uncover any unique catalytic characteristics that may arise from these modifications and offer valuable insights into the design and application of MOFs for a wide range of organic conversions. Ultimately, our work aims to contribute to the development of MOF-based catalytic systems that can provide innovative and sustainable solutions, advancing the field of catalysis and addressing industrial challenges.

Acknowledgments :

The authors express their sincere gratitude to the Science and Engineering Research Board (SERB) in New Delhi for generously providing funding support through the Start-Up Research Grant (Young Scientists). – Chemical Sciences No. SB/FT/CS-061/2012.

Figures:

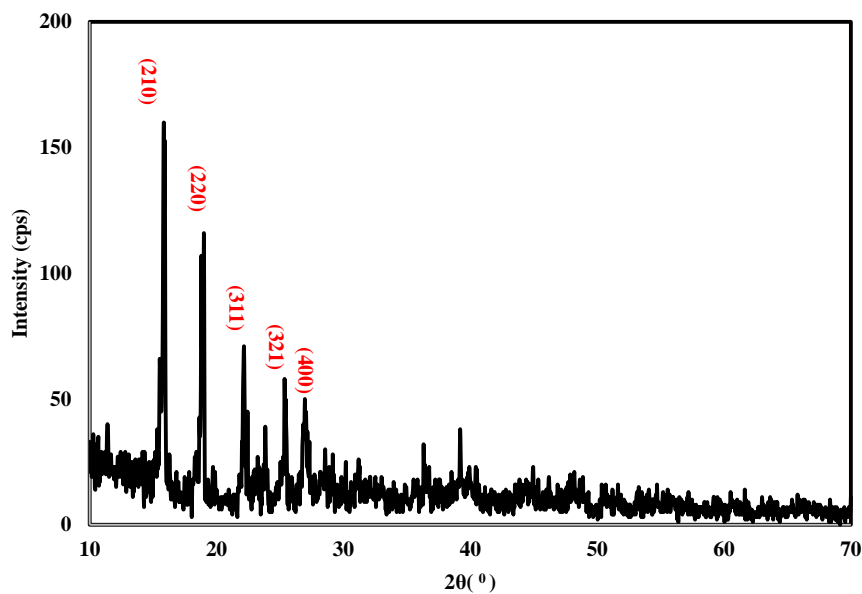


Fig. 1a PXRD image of Mg-BTC MOF.

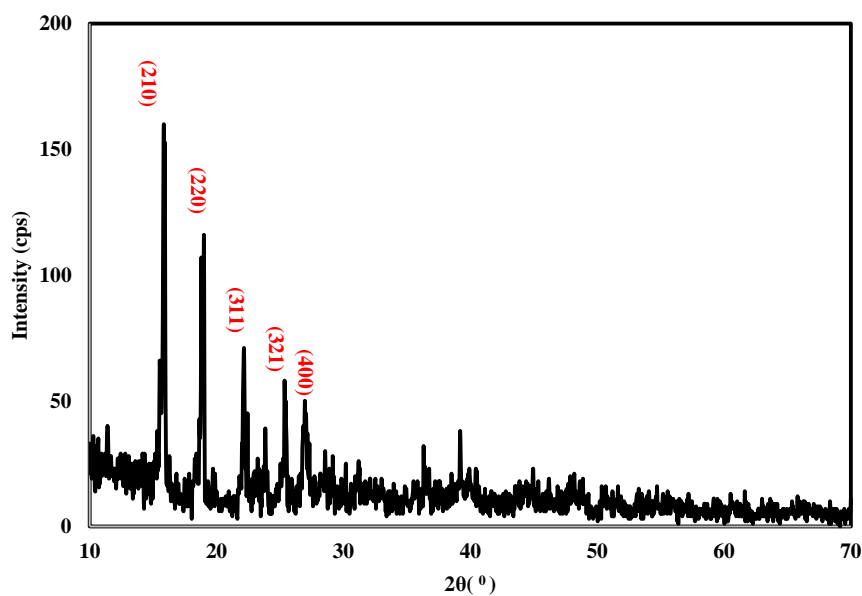


Fig. 1b PXRD image of TiO₂@ Mg-BTC MOF.

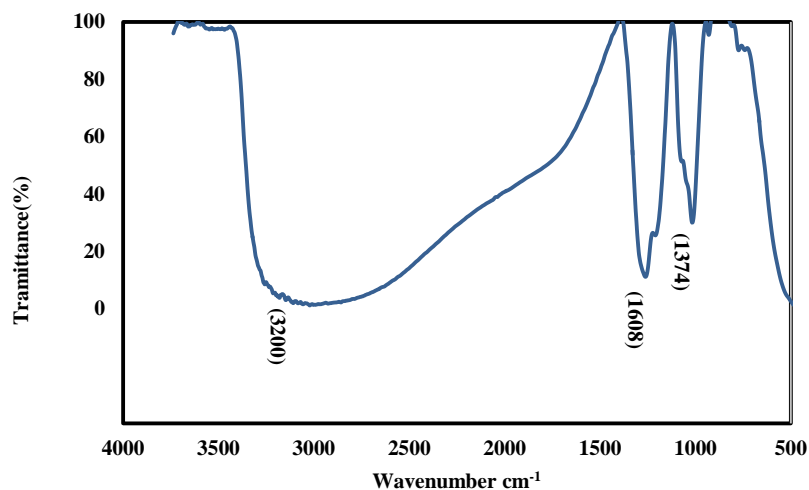


Fig. 2a FT-IR image of Mg-BTC MOF.

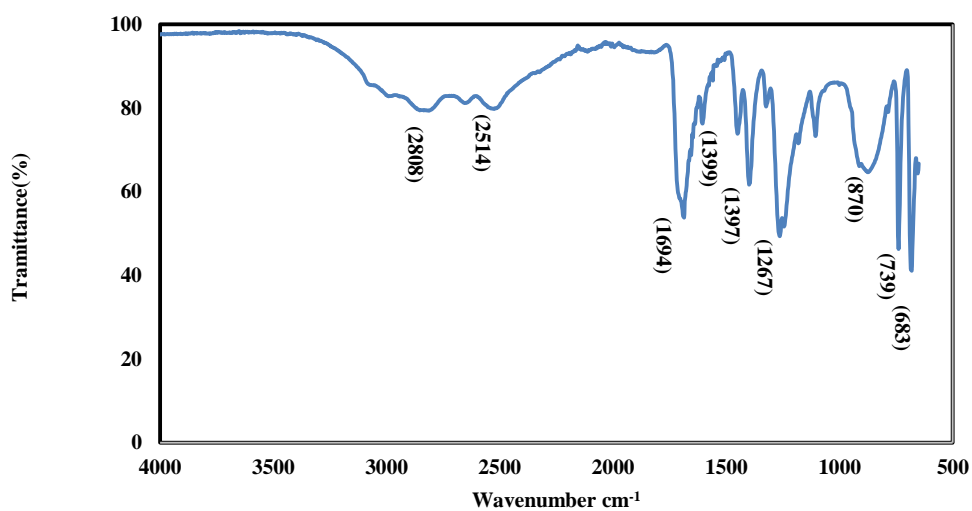


Fig.2b FT-IR image of TiO₂ @Mg-BTC MOF.

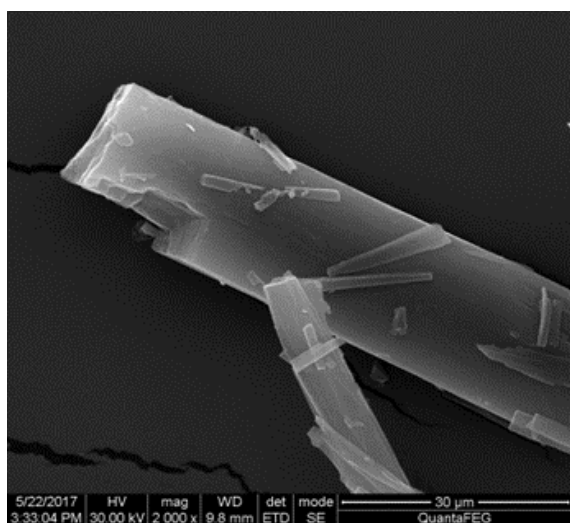


Fig. 3a SEM image of Mg-BTC MOF.

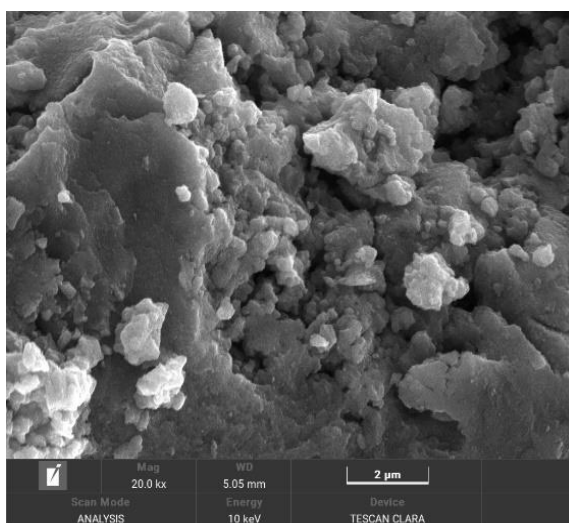


Fig. 3b SEM image of TiO₂@ Mg-BTC MOF.

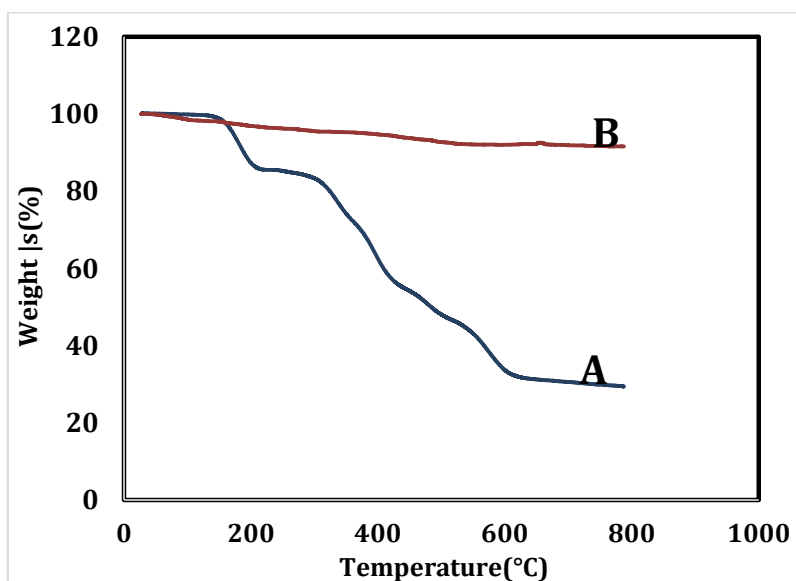


Fig. 4 Thermogravimetric analysis Spectrum of A) Mg-BTC MOF B) TiO₂@ Mg-BTC MOF

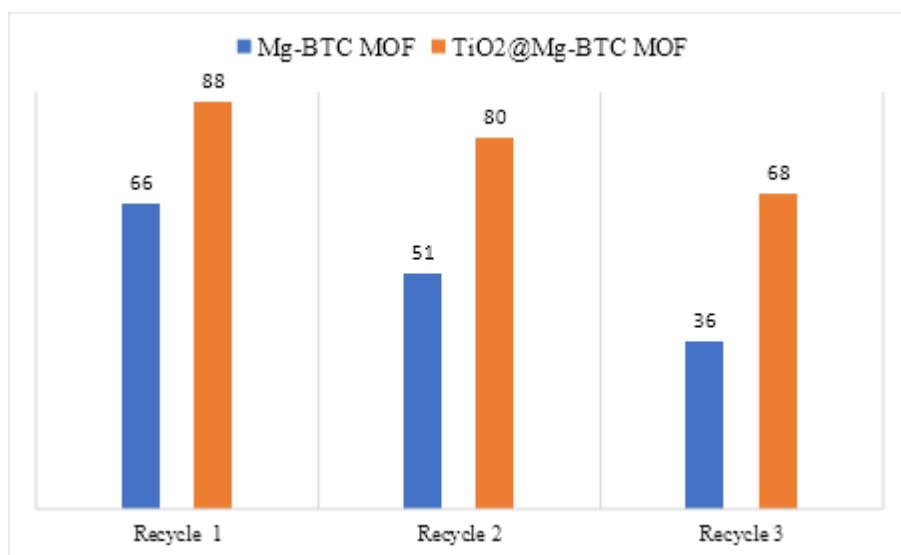


Fig.5 Reusability of Mg-BTC MOF and TiO₂@Mg-BTC MOF for cyanosilylation of aldehydes.

Tables:

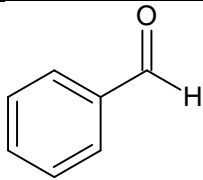
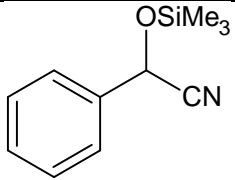
Table 1: Plausible Crystallographic data of Mg-BTC and TiO₂ @ Mg-BTC MOFs.

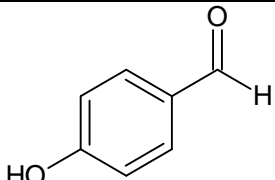
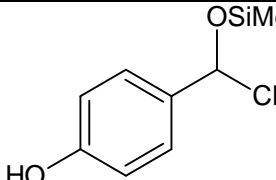
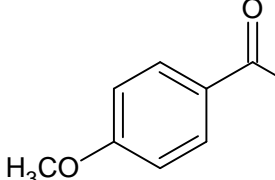
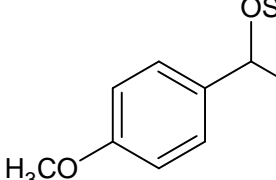
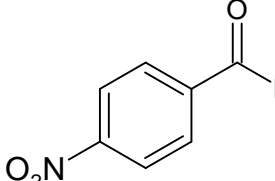
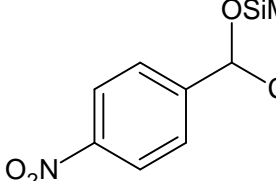
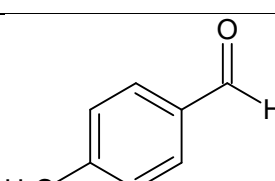
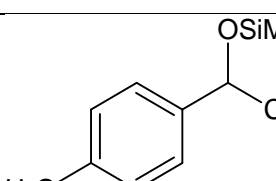
Properties	Mg-BTC MOF	TiO ₂ @ Mg-BTC MOF
Crystal system	Triclinic	Triclinic
a [Å]	7.87097	12.38563
b [Å]	11.60119	14.61443
c [Å]	15.95049	6.20901
α [degree]	59.26130	92.52675
β [degree]	117.29031	90.24860
γ [degree]	90.33700	103.29796
V(Unit cell volume)[Å ³]	912.21	1092.57
Space group	P1	P1
D crystallite size nm	25.5614	51.62482

Table 2: Textural properties of Mg-BTC and TiO₂@Mg-BTC MOFs

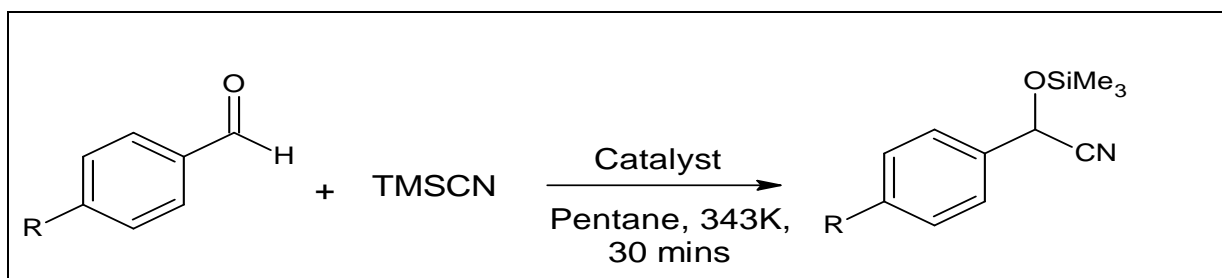
Metal Organic Frameworks	A _{BET} (m ² /g)	d _p (nm)	V _p (cm ³ /g)
TiO ₂ @ Mg-BTC	375	2.25	0.185
Mg-BTC	893	3.1	0.723

Table 3. Comparative study on the catalytic activity of Mg-BTC and TiO₂ @ Mg-BTC MOF

Substrate	Product	Yield %	
		Mg-BTC MOF	TiO ₂ @ Mg-BTC MOF
			

		60	82.25
		64	89.7
		67	87
		75	98
		65	85

Scheme:



Scheme 1 Schematic representation of cyanosilylation of aldehydes.

References

1. J. D. Sosa, T. F. Bennett, K. J. Nelms , B. M. Liu , R. C. Tovar and Y. Liu, Crystals, 8, 325, 2018.
2. A. Aijaz, Q. Xu, J. Phys. Chem. Lett, 5, 1400, 2014.
3. K.V. Kumar, K. Preuss, M.M Titirici, F. Rodríguez-Reinoso, Chem. Rev., 117, 1796, 2017.
4. Z.R. Herm, E.D. Bloch, J.R. Long, Chem. Mater, 26, 323,2014.

5. S. Rojas, F.J. Carmona, C.R. Maldonado, P. Horcajada, T. Hidalgo, C. Serre, J.A.R. Navarro, E. Barea, *Inorg. Chem.*, 55, 2650, 2016.
6. Y. Liu, J. Howarth Ashlee, T. Hupp Joseph, K. Farha Omar, *Angew. Chem.Int.Ed.*, 54, 9001, 2015.
7. X.M. Li, L.Z. Dong, S.L. Li, G. Xu, J. Liu, F.M. Zhang, L.S. Lu, Y.Q. Lan, *ACS Energy Lett.*, 2, 2313, 2017.
8. W. Huang, S. Li, X. Cao, C. Hou, Z. Zhang, J.Feng, L. Ci, P. Si, Q. Chi, *ACS Sustain. Chem. Eng.*, 5, 5039, 2017.
9. C.T. Buru, P. Li, B.L. Mehdi, A. Dohnalkova, A.E. Platero-Prats, N.D. Browning, K.W. Chapman, J.T. Hupp, O.K. Farha, *Chem. Mater.*, 29, 5174, 2017.
10. Z. Chen, Z.G. Gu, W.Q. Fu, F. Wang, J. Zhang, *ACS Appl. Mater. Interfaces*, 8, 28737, 2016.
11. H. K. Okoro, S. O. Ayika, J. C. Ngila, A. C. Tella, *Applied Water Science* , 8:169, 2018.
12. D. Saha, T. Maity, S. Das and S. Koner, *Dalton Trans.*, 42, 13912, 2013.
13. J. Xu, Y. Yu, G. Li, S. Wang, Y. Liu, D. Liu and C. Wang, *RSC Adv.*, 6 (106), 104451, 2016.
14. G. Mali, J. Trebosc, C. Martineau, M. Mazaj, *J. Phys. Chem. C* , 119, 7831, 2015.
15. D. Saha, T. Maity and S. Koner, *Dalton Trans.*, 43, 13006, 2014.
16. S. Mandal, S. Natarajan, P. Mani, and A. Pankajakshan , *Adv. Funct. Mater.* 31(4), 2006291, 2020.
17. J. Rajendran, K. Tamil , D. Lokhendra, M. Preethika, A. Raji , A. Zeid , O. Mohamed and S. Ashok. *Chemosphere*. 287, 132106, 2021.
18. G. Sridharan, R. Atchudan, V. Magesh, S. Arya, D. Ganapathy, D. Nallaswamy, A. K. Sundramoorthy, *Electroanalysis*, 35, e202300093, 2023.
19. S. Chandra Kishore, S. Perumal, R. Atchudan, A.K. Sundramoorthy, M. Alagan, S. Sangaraju and Y.R. Lee, *Catalysts*, 12(12), 1501, 2022.
20. Y. Hu, Z. Huang, L. Zhou, D. Wang, G. Li, *J Sep Sci*, 37, 1482, 2014.
21. P. H. M. Andrade , A. L. M. Gomes , H. G. Palhares , C. Volkringer , A. Moissette , H. F. V. Victoria , N. M. A. Hatem, K. Krambrock , M. Houmard and E. H. M. Nunes, *J Mater Sci* , 57, 4481, 2022.
22. H. G. Palhares, B.S. Goncalves, L.M.C. Silva et al, *J Sol-Gel Sci Technol*, 95, 119, 2020.
23. H. Hu, M. Chang, X. Wang, D. Chen, *J Mater Sci* , 7, 55653, 2017.
24. B.S. Goncalves, H. G. Palhares, T.C.C. de Souza et al , *J Mater Res Technol*, 8, 6262, 2019.

25. B.S. Goncalves , T.C.C. de Souza, V.G. de Castro et al, J Mater Res, 34, 3918, 2019.
26. A. K. Singh, S. R. Deo, G. S. Thool, R. S. Singh, Y. R. Katre And A. Gupta, J. Synth. React. Inorg. Metal-Org. Nanometal. Chem, 41(10), 1346, 2011.
27. M. Crisan , A. Braileanu, M. Raileanu et al, J Non Cryst Solids, 354,705, 2008.
28. D.C.L Vasconcelos, E.H.M. Nunes, A.C.S. Sabioni et al, J Non Cryst Solids, 07, 035 , 2012.
29. J. Yang, H. Peterlik, M. Lomoschitz, U. Schubert, J Non Cryst Solids, 356:1217, 2010.
30. J. B. DeCoste, G, W. Peterson, B. J. Schindler, K. L. Killops, M. A. Broweb and J. J. Mahle, J. Mater. Chem. A, 1, 11922, 2013.
31. Y. Liu, P. Zhao, C. Duan and C. He, RSC Adv., 11, 34779, 2021.
32. H. Jun, S. Oh, G. Lee and M. Oh, Scientific Reports, 12, 14735, 2022.
33. J. Du, X. Zhang, X. Zhou and D. Li, *Inorg. Chem. Front.*, 5, 2772, 2018.

Tropospheric Ozone levels in and around southern city Bengaluru, India

P. Anukrishna¹, Aditya D. Chate^{2*} and G. Dhanya³

¹Indian Institute of Science Education and Research, Tirupati- 517619, India

^{2*}SMIT Enviro Solutions, Pune – 411057, India

³National Institute of Advanced Studies, Bengaluru- 560054, India

*Email: admin@smitenvirosolutions.in

Received: 23.3.2024, Revised: 16.4.2024, 23.4.2024, Accepted: 24.4.2024

Abstract

The diurnal to seasonal ozone (O₃) pre-cursors (NO, NO₂, CO, VOCs) trends over local climatic zones (LCZs) with the changes in weather patterns with respect to land cover classes determines the O₃ trends and useful for air quality management. In this work, diurnal to seasonal patterns of O₃ concentrations are analysed across the different LCZs in Bengaluru region. The Central/State Pollution Control Boards (CPCB/SPCB) operate more than 500 continuous air quality and weather monitoring stations across the India. Hourly O₃ concentration data were collected from CPCB for 5 different LCZs within the Bengaluru region over a period of four years (2019-2022). Time series analyses were conducted to examine the temporal variations in O₃ levels. The results showed significant fluctuations in diurnal trends of O₃ due to the influence of air temperature and relative humidity variations across the five LCZs within Bengaluru region. There were distinct seasonal trends in O₃ concentrations with maximum (60-65 ppb) observed during the winter and summer seasons and that of minimum concentration in the range 20-25 ppb during the monsoon months. The observed maximum ozone levels (60 -65 ppb) found to be beyond the threshold national ambient air quality standard (NAAQ) and the accumulation exposure over threshold of 40 ppb (AOT 40) during the winter and summer. The O₃ concentration trends are in line with the published research on premature mortality about 1200 annually for Karnataka state for chronic obstructive pulmonary disease owing to population exposure to O₃ beyond its threshold level of NAAQ. Also, the annual rice yield loss is about 2% (~0.1 Metric Tonne) with the AOT 40 to paddy crop for Karnataka state. Thus, O₃ diurnal to seasonal trends serve the first-hand information to local authorities for the action plan of air quality management taking into consideration O₃ precursors, wind speed, and wind direction.

Keywords: *Greenhouse gases, ozone pre-cursors, local climatic zones, CPCB*

1. Introduction

Short-lived greenhouse gas emitted largely from fuel combustions account directly or indirectly for extreme pollutant episodes that damages the crops. They also account for most of the direct damage to human health from energy consumption. These air pollutants include both health and crop damaging agents such as ozone (O_3), a secondary pollutant formed after complex photochemical reactions, and other gases that contribute to ozone formation such as carbon monoxide (CO), volatile organic compounds (VOCs), and oxides of nitrogen (NO, NO_2). Most of these precursors to O_3 also exert direct effects on crop yields and human health¹. South Asian countries² (Male Declaration on Control and Prevention of Air Pollution, 2010)² have yet to be successful in gaining political support for action to be taken to reduce the threat posed by ground level O_3 on health and agriculture. This is a major concern for developing countries like India where economic growth has led to rapid increase in NO, NO_2 , CO, and VOCs and to increased levels of O_3 . The O_3 concentration is influenced by air temperature, relative humidity, solar radiation, wind speed, and wind direction^{3, 4}. The weather scenarios over land covers-specific local climatic zones (LCZs)-determines O_3 and its precursors (NO, NO_2 , CO, VOCs) levels.

The O_3 and its precursors trend depends on temperature and O_3 photochemical reaction rate, urban and suburban activities, and sector-specific emission factors. The analysis of O_3 and its pre-cursors over the urban and suburban LCZs within the megacities is crucial to understand the air quality scenarios. These results can be the first-hand information for planning of policy-induced air pollution control strategies. This paper presents the analysis of diurnal to seasonal patterns of O_3 across the 5 LCZs within the domain of Bengaluru region.

2. Experimental

2.1 Instruments and dataset

Large volumes of datasets for variety of weather and air quality parameters are available from the Central/State Pollution Control Boards (CPCB/SPCBs). Surface air quality dataset consists of CO_2 , CO, SO_2 , NO_2 , O_3 , PM_{10} , $PM_{2.5}$, NH_3 , and Benzene. The measurements of these air pollutants along with weather parameters are conducted by CPCB and SPCBs, with the continuous air quality and automated weather monitors over more than 500 stations across India. The datasets of hourly O_3 concentrations, air temperature and relative humidity used in this paper were collected from CPCB's website⁵. The O_3 concentrations are measured using commercial ozone analyzer (model O342M, Environment SA, France) which works on UV absorption principle. The lower detection limit of the analyser is 0.4 ppb⁶. Hourly O_3

concentration data were collected for four years, 2019 to 2022 from 5 continuous air quality and weather monitoring stations within the study domain of Bengaluru region.

2.2 Study domain

Bengaluru's transformation into one of the major Information and Technology hub with the establishment of start-ups and corporate offices and industries have led to population growth, road expansion, and rapid infrastructural development. These changes in land cover impact air quality. The rapid increase in number of vehicles, coupled with rising population, has led to significant vehicular pollution. Traffic congestion results in more emissions, especially during stop-and-go situations across the junctions. The details of air quality and weather monitoring sites as shown in map (Figure 1) are tabulated in Table 1. The map in Figure 1 is created using Geographic Information System with latitudes and longitudes (Table 1) of CPCB's air quality and weather monitoring stations within Bengaluru region. Hourly O₃ concentrations, air temperature and relative humidity data collected from these LCZs are analyzed over diurnal to seasonal variations, and emission sources⁷.

2.3 Weather and climatology of Bengaluru

The seasons in Bengaluru can be broadly categorized into:

1. Summer (March to May): Summers are generally warm, with temperatures ranging from 25°C to 35°C. Average annual maximum and minimum temperatures are 29.6°C and 19.2°C respectively. The mean maximum temperature of the hottest month (April) is 34°C and the coldest month (January) is 27.9°C.
2. Monsoon (June to September): Bengaluru receives the majority of its rainfall during the monsoon season. Average annual rainfall is 1004 mm. The mean monthly highest rainfall observed in September is 220 mm and lowest rainfall observed in January is 2 mm.
3. Post-Monsoon/Autumn (October to November): After the monsoon season, temperatures start to cool down gradually, and the weather becomes more pleasant. In post monsoon skies are moderately cloudy.
4. Winter (December to February): Winters in Bengaluru are generally mild, with temperatures ranging from 15°C to 28°C. Fogs occur occasionally during winter season.

2.4 Local Climatic Zone map

Local Climate Zones (LCZs) are a classification system used to categorize urban areas based on their surface cover and other characteristics that influence the local climate. The LCZs are used in urban climatology and urban planning to understand the urban heat island effect, energy consumption, and the impact of urbanization on local climate conditions. These zones are often determined by factors such as latitude, altitude, proximity to large bodies of water, ocean currents, prevailing winds, and topography. Different regions around the world can be categorized into various local climatic zones based on their unique climatic features. LCZ classification is based on 17 classes, each representing different urban and natural features⁸. These classes are denoted by numbers and labels. Understanding the specific climatic characteristics of a region helps in making informed decisions related to land use, infrastructure development, and resource management. It also plays a crucial role in predicting weather patterns and natural disasters, as well as understanding the impact of climate change on different regions. Figure 2, shows the generated LCZs classification of Bengaluru region using standard land use land cover data⁹.

2.5 Methodology

Surface measurements conducted by the Central Pollution Control Board (CPCB) and the Quality Control and Quality Assurance (QC/QA) guidelines are archived¹⁰. The hourly data of ozone, temperature, and relative humidity during the years 2019 - 2022 were obtained from CPCB for the five stations tabulated (Table 1) as shown in Figure 1. The random fluctuations with the reference threshold value ($O_3 > 1000 \mu\text{g}/\text{m}^3$) that appeared in just one hour in all five monitoring stations in and around Bengaluru have been filtered. The QC/QA were performed on the collected meteorological parameters by removing outliers with respect to technical specifications of measurement sensors, random fluctuations and single peaks right after the missing data points in time-series. The diurnal variations of ozone with temperature and relative humidity were plotted. The hourly data over different months were averaged to plot the seasonal variations as well. The months from December to February were considered as winter, March to May as summer, June to September as monsoon, and October to November as post-monsoon as per India Meteorological Department (IMD).

3. Results and Discussion

Figs 3 to 11 show the diurnal variation of ozone along with temperature and relative humidity. The diurnal variation of ozone shows a similar trend in all the sites. The ozone

concentration is maximum during the afternoon hours (12 - 3 pm). This can be attributed to intense solar radiation during afternoon hours. The ozone concentration is minimum during the early morning (4-8 am) and evening hours (6-7 pm). The boundary layer of the atmosphere is well-mixed during the daytime. As the Sun sets, the boundary layer stabilizes and mixing reduces, thereby reducing the ozone concentration. This is further assisted by the absence of photochemical reactions due to reduced solar radiation. The maximum concentration of ozone varies between 60-65 ppb and the minimum varies between 20-25 ppb. For Karnataka state, premature mortality of about 1200 reported for chronic obstructive pulmonary disease with the population exposure to O₃ beyond its threshold level of national ambient air quality standard by CPCB¹¹. Also, the percentage loss of rice around 2% (~0.1 Metric Tonne) with the accumulation exposure over threshold of 40 ppb (AOT 40) to paddy crop for Karnataka state¹². Nevertheless, the LCZs specific health and vegetation impact within the Bengaluru region is out of the scope of this work and option to future study.

There are also yearly variations in this trend. The ozone concentration trend during 2019 is maximum compared to other years. The meteorological parameters considered for the study are temperature and relative humidity. The diurnal variation of temperature shows that it is maximum during the afternoon hours and minimum during the early morning and midnight. It shows a maximum of 27° C and a minimum of 20° C. Whereas, the relative humidity is maximum during early morning and late-night hours and minimum during afternoon hours. It shows a maximum of 75-80% and a minimum of 40%.

Diurnal variations of ozone and temperature follow a similar pattern in all the stations. The ozone concentration is maximum during the maximum temperature. This indicates that ozone is formed during intense solar radiation assisted by high temperature. At ground level, ozone peaks during the noon and afternoon hours due to photochemical formation and decreases gradually during late afternoon and evening hours due to dry deposition. But, the diurnal variations of ozone and relative humidity show the opposite trend. The ozone concentration is maximum when the relative humidity is minimum. The ozone concentration decreases with increasing humidity due to the attenuation of light due to absorption by water vapor, leading to a decreased O atom production by O₂ which is required to produce ozone^{13, 14}. The high ozone episode days during peak summer were associated with meteorological parameters such as sunny and warm weather, with the low relative humidity¹⁵.

Figs. 12 to 21 explain the seasonal variation of ozone with temperature and relative humidity. The seasonal variation of ozone shows a peak ranged from 60-65 ppb during the winter and

summer seasons. During winter, the atmosphere tends to be more stable, leading to reduced vertical mixing of air. This stability can trap pollutants, including ozone, closer to the ground, resulting in higher concentrations. Also, the emissions from sources like heating systems and vehicular traffic may increase during colder months, contributing to higher ozone levels. In the summer, higher temperatures and increased solar radiation can promote the formation of ground-level ozone through complex photochemical reactions involving volatile organic compounds (VOCs) and oxides of nitrogen ($\text{NO}_x = \text{NO} + \text{NO}_2$). The seasonal variation of ozone is minimum during monsoon season and ranged from 20-25 ppb. The monsoon season is characterized by heavy and frequent rainfall. The reduced variability during monsoon season may be first attributed to overcast sky condition leading to reduced photochemical ozone formation further being assisted by scavenging¹⁶.

The seasonal variation of temperature shows a usual trend of maximum during the summer season and minimum during the winter season. The seasonal variation of relative humidity is maximum during the monsoon season and minimum during the summer season. During the monsoon season, which is characterized by heavy and frequent rainfall, the air become moist due to the evaporation of water from land and water bodies. The increased moisture content in the air leads to higher relative humidity levels. It is the opposite during the summer season. The seasonal variations of ozone and temperature indicate that ozone is formed maximum during the summer season when the solar radiation is more intense. Seasonal variation of ozone and relative humidity shows that ozone is minimum during the monsoon and post-monsoon season when the relative humidity is maximum. Ozone is maximum during winter and summer when the relative humidity is minimum with respect to monsoon months.

4. Conclusions

The ozone pre-cursors (NO, NO_2 , CO, VOCs) concentration in presence of solar radiation determines the diurnal to seasonal trends in ozone levels across the different local climatic zones (LCZs) with the changes in weather patterns with respect to land cover classes and they are the essential ingredients for managing the air quality. The diurnal to seasonal trends of ozone concentrations based on hourly data of air quality, temperature and relative humidity at five different LCZs over a period of 4 years (2019-2022) showed the maximum (60-65 ppb) observed levels during the winter and summer seasons and the minimum (20-25 ppb) during monsoon months. The maximum ozone levels in the range 60 -65 ppb are found to be beyond the threshold national ambient air quality standard (NAAQ) and the accumulation exposure

over threshold of 40 ppb (AOT 40) during the winter and summer seasons over a period of 2019 to 2022. These results corroborate published research on the premature mortality of about 1200 annually for chronic obstructive pulmonary disease owing to population exposure to O₃ beyond its threshold level of NAAQ for Karnataka state. The results are in line with the published research on annual rice yield loss of about 2% (~0.1 Metric Tonne) with the AOT 40 to paddy crop for Karnataka state. The diurnal to seasonal trends of ozone concentrations with the temperature and relative humidity across the different local climatic zones (LCZs) within the Bengaluru region serves the ready reckoner to undertake policy-induced emission control measures of ozone pre-cursors to manage quality of the air across the LCZs in Bengaluru region. The future scope can be the LCZ-specific health and vegetation impact assessments within the Bengaluru region taking into consideration diurnal to seasonal trends of ozone and its precursors as a function of weather parameters including prevailing winds.

5. Acknowledgement

Authors thank the Central and State Pollution Control Boards for retrieving air quality and weather data from their websites. One of the post graduate student authors of IISER, Tirupati (P. Anukrishna) thanks SRFP for sponsoring her fellowship and Dr. Dilip M. Chate for guidance. Co-author, Aditya D. Chate would like to thank SMIT Enviro Solutions, Pune India for sponsoring him for scientific editing of this manuscript.

Figures:

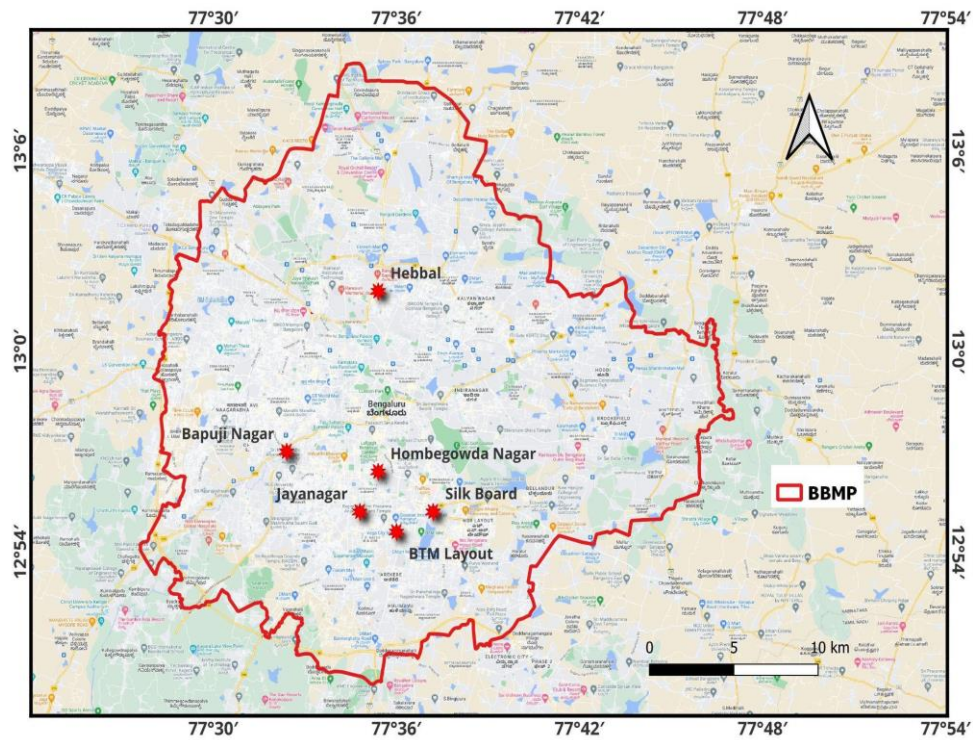


Fig. 1: Map shows locations of air quality and weather monitoring sites

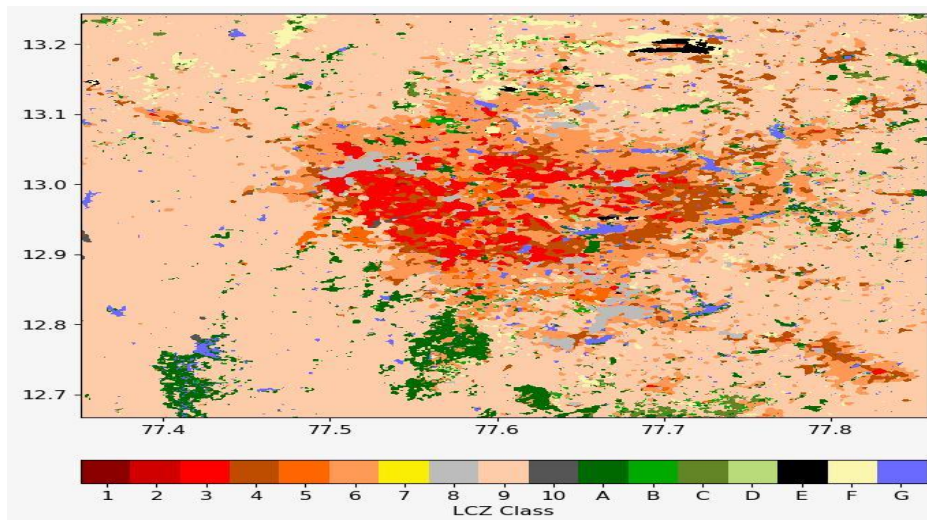


Fig. 2: Local climatic zones (LCZ) with LCZ classes (Bengaluru)

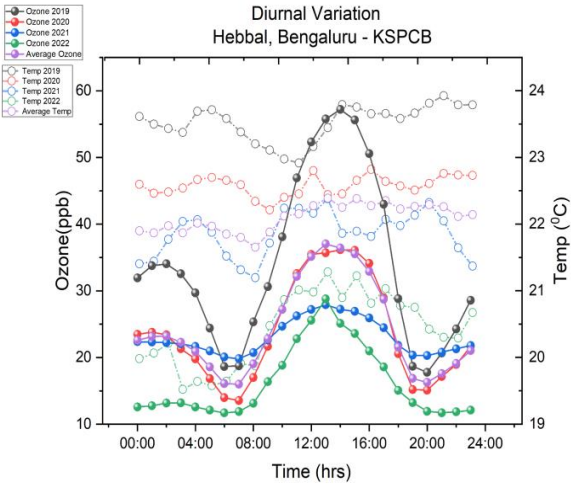


Fig. 3

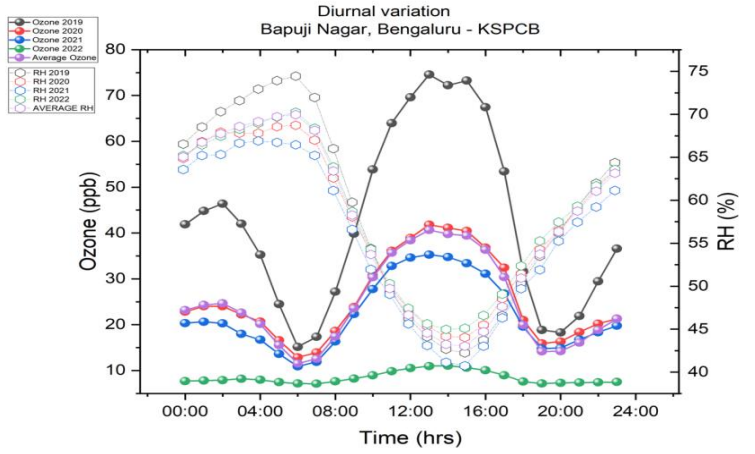


Fig.4

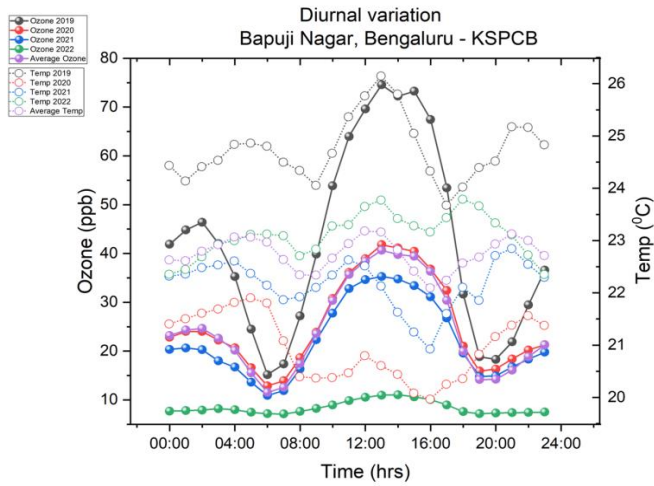


Fig. 5

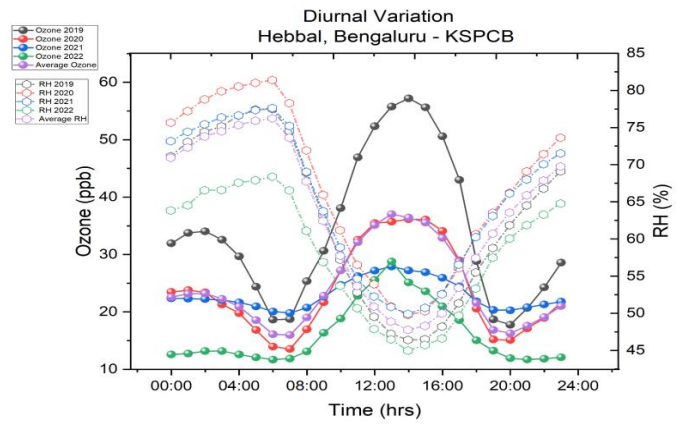


Fig. 6

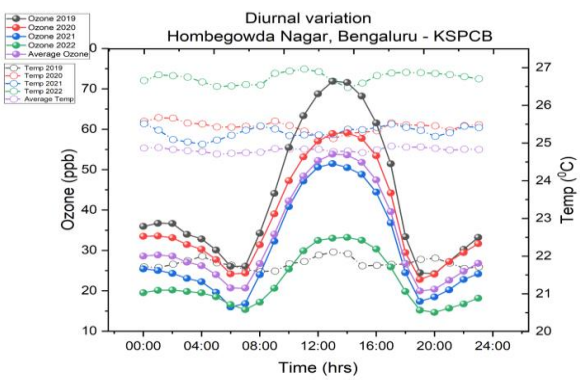


Fig. 7

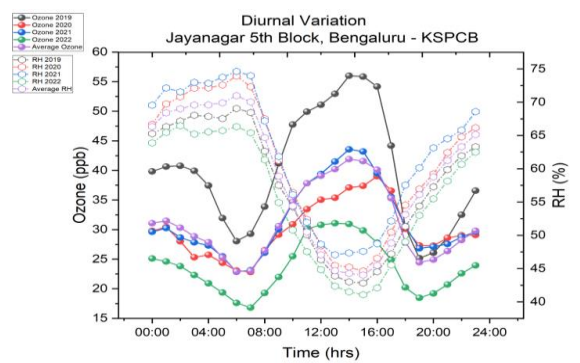


Fig. 8

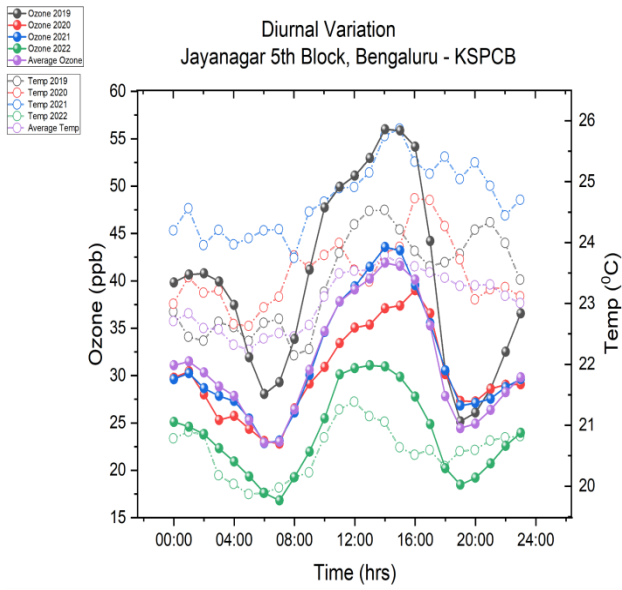


Fig. 9

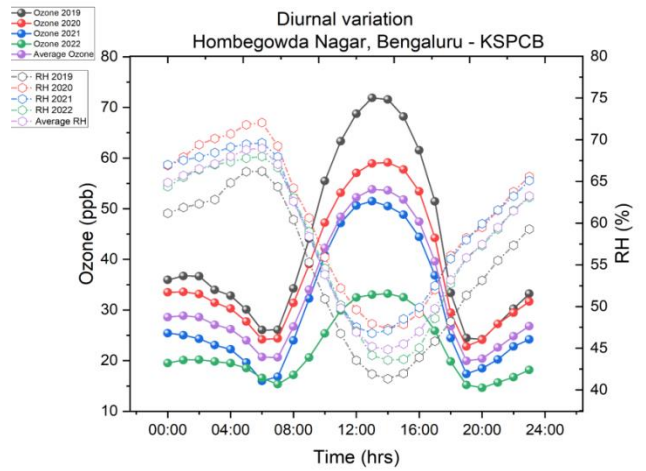


Fig.10

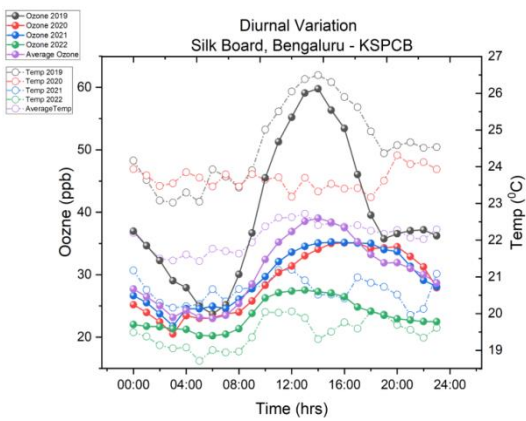
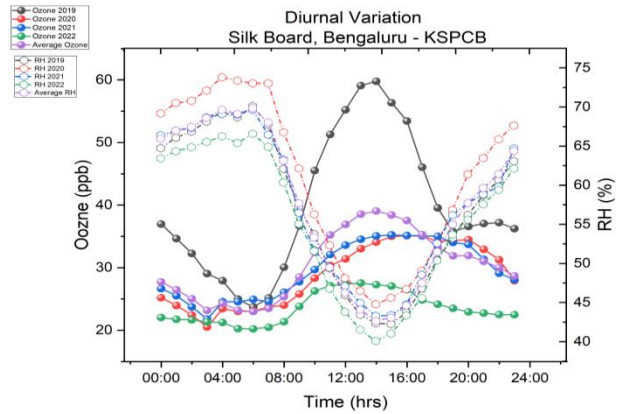


Fig. 11



Figs. 3 to 11: The diurnal variation of ozone with temperature and relative humidity over different stations.

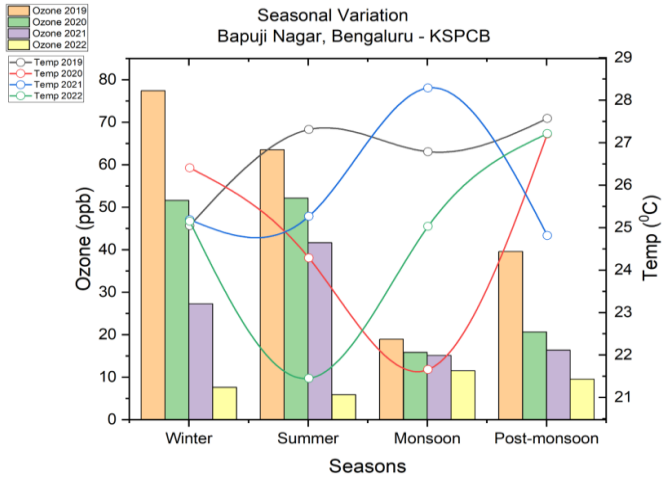


Fig. 12

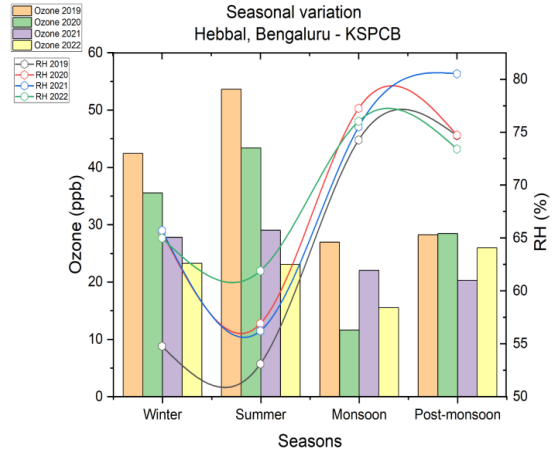


Fig. 13

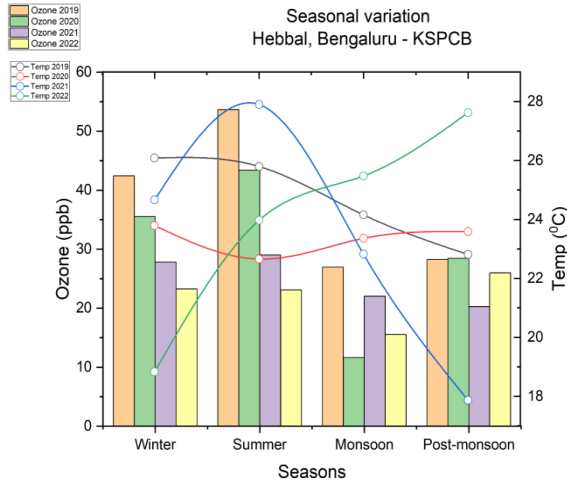


Fig. 14

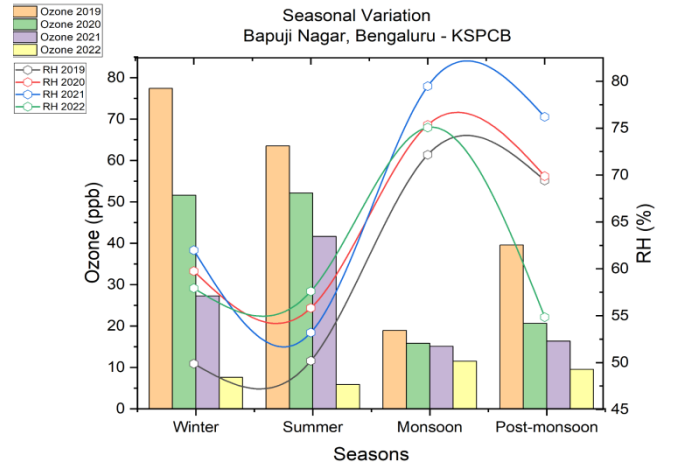


Fig. 15

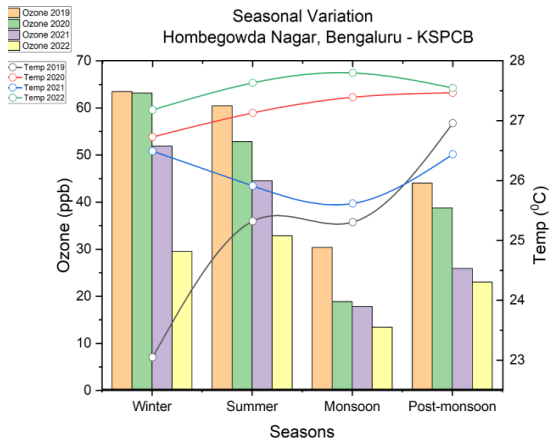


Fig. 16

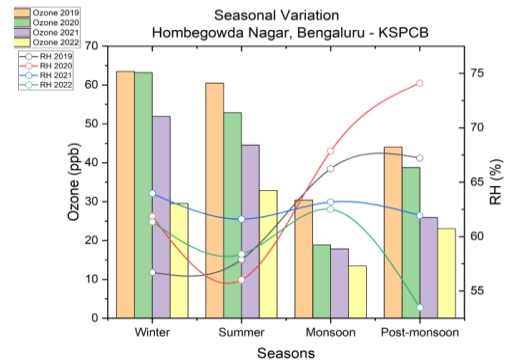


Fig. 17

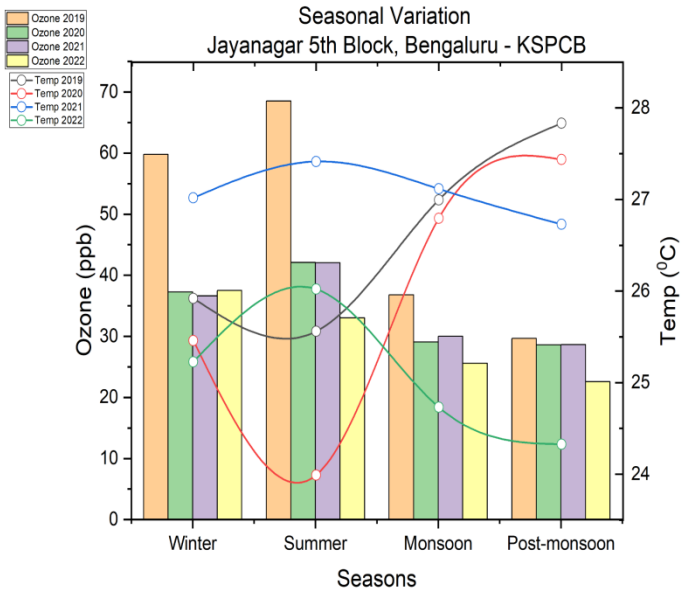


Fig. 18

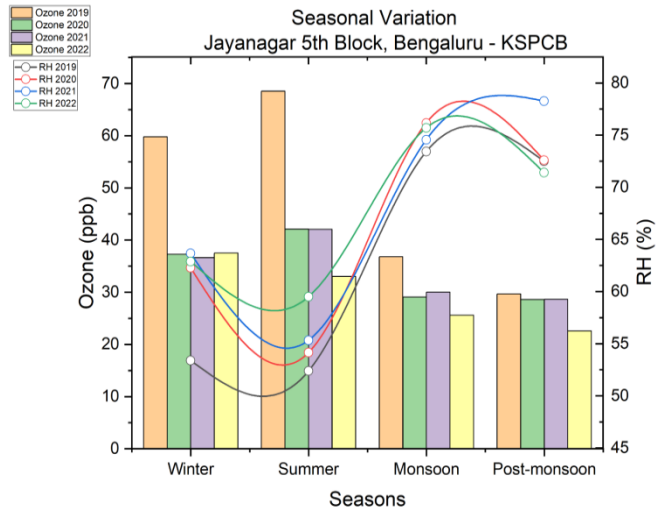


Fig. 19

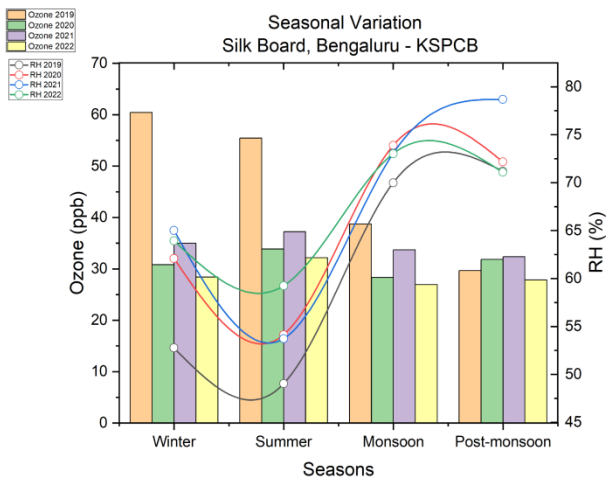


Fig. 20

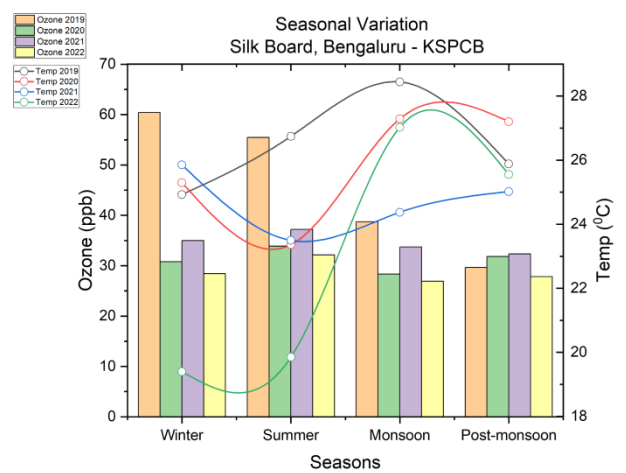


Fig. 21

Figs. 12 to 21: Seasonal variation of ozone as a function of temperature and relative humidity.

Table 1: Air Quality and weather monitoring sites in Bengaluru

S N	Sites in and around Bengaluru	Latitude	Longitude
1	Bapuji Nagar	12.951913° N	77.539784 °E
2	Hebbal 1 st Stage	12.21041 °N	76.37376 °E
3	Hombegowda Nagar	12.938539° N	77.590100 °E
4	Jayanagar 5 th Block	12.920984 °N	77.584908 °E
5	Silk Board	12.917348 °N	77.622813° E

References:

1. A. P. K. Tai, M. Sadiq, J. Y. S. Pang, D. H. Y. Yung and Z. Feng, *Front. Sustain. Food Syst.*, 5, 534616, 2021.
2. Male Declaration on Control and Prevention of Air Pollution, 2010, (<http://www.sacep.org/library/male-declaration-reports>)
3. H. Bao, K. L. Shrestha, A. Kondo, A. Kaga, Y. Inoue, *Atmos. Environ.* 44, 421, 2010.
4. G. Dhanya, T. S. Pranisha, D. M. Chate, G. Beig, *J. Photochem. Photobio.*, 98 (6), 1312, 2022.
5. Central Pollution Control Board (<https://www.cpcb.nic.in>)
6. S. Sharma, P. Sharma, M. Khare. and S. Kwatra, *Sus. Environ. Res.*, 26 (3): 142, 2016.
7. K. C. Gouda, S. Singh, P. Nikhilasuma, M. Benke, K. Reshama, A. Geeta, K. M. Hungund, M. Chandrika, K. B. Rao, V. Ramesh, S. Himesh, *Environ. Monit Assess* 193, 395, 2021.
8. I. D. Stewart, T. R. Oke, *Bulletin of the Ameri. Met. Soc.*, 93 (12), 1879, 2012.
9. United States Geological Survey (<https://www.usgs.gov/>)
10. Central Pollution Control Board's data quality assurance and data quality control (<https://cpcb.nic.in/quality-assurance-quality-control/>).
11. S. D. Ghude, C. Jena, D. M. Chate, G. Beig, G. G. Pfister, R. Kumar, and V. Ramanathan, *Geophys. Res. Lett.*, 41, 5685, 2014.

12. S. D. Ghude, D. M. Chate, C. Jena, G. Beig, R. Kumar, M. C. Barth, G. G. Pfister, S. Fadnavis, and P. Pithani, *Geophys. Res. Lett.*, 43, 4650, 2016.
13. D. M. Chate, S. D. Ghude, G. Beig, A. S. Mahajan, C. Jena, R. Srinivas, A. Dahiya and N. Kumar, *Atmos. Enviro.* 96, 353, 2014.
14. R. Ono, Y. Nakagawa, Y. Tokumitsu, H. Matsumoto, T. Oda, *J. Photochem. Photobio.*, 274, 13, 2014
15. V. Singla, A. Satsangi, T. Pachauri, A. Lakhani, K. K. Maharaj, *Atmos. Res.* 101 (1/2), 2011.
16. H. M. T. Brink, A. J. Janssen, J. Slanina, *Atmos. Enviro.* 22 (1) 177, 1967.

Removal of crystal violet, an emerging pollutant from aqueous solution using biochar prepared from coconut shell

Jonty Rodrigues, Sugandha Shetye*, Sheba Raju

Department of Chemistry, K J Somaiya College of Science and Commerce, Vidyavihar,

Mumbai 400077, India

Email: *sugandha@somaiya.edu

Received: 23.3.2024, Revised: 26.4.2024, Accepted: 27.4.2024

Abstract

Crystal violet is an emerging pollutant which may be transferred into water bodies and does not have any established guidelines for detection. Biochar, a material derived from the partial pyrolysis of biomass, exhibits remarkable potential in removing organic contaminants like crystal violet due to its porous structure. In this study coconut shell powder was subjected to pyrolysis at four distinct temperatures to obtain biochar samples. Proximate analysis was performed for all the biochar samples obtained. The samples were characterised using FTIR, SEM and XRD. Kinetics and isotherm studies were performed on the biochar to determine the mechanism of adsorption and maximum removal capacity. As the pyrolysis temperature increased the pH and ash content increased, the yield of biochar decreased. The biochar prepared at 700 °C showed the best adsorption capacity among all the prepared biochar samples. Response surface methodology suggested the optimum dosage of biochar required is 210 mg at a concentration of 12 ppm. The adsorption process adhered to second-order kinetics, and the maximum adsorption capacity, according to the Langmuir adsorption isotherm, was determined to be 124.5 mg.g⁻¹.

Key words: Coconut shell Biochar, Emerging Contaminants, Adsorption Studies, crystal violet, Response Surface Methodology.

Introduction

In recent years, water resources have become increasingly polluted due to overexploitation and rapid industrialization. Dyes are one of the major constituents of industrial pollutant¹. As such a considerable effluent enters the environment and pollutes the environment, as well as enters the food chain leading to biomagnification². Crystal violet is a purple-coloured dye used chiefly in textile industries for colouring cotton and silk. It is also used as a biological staining, external skin disinfectants³, as well as an antimicrobial agent to prevent fungal growth in poultry litter⁴. The dye is potentially carcinogenic, genotoxic and mutagenic

causing development of tumour in some species of fish if persistent in environment for long periods of time⁵. It is found to be a moderate eye irritant, and can cause permanent injury to cornea and conjunctiva, and in extreme cases lead to kidney or respiratory failure⁵. Norman List of emerging pollutants⁶ has included crystal violet as an emerging pollutant that is currently not included in routine monitoring programmes at the European level and which may require future regulation, depending on further research on their ecotoxicity, potential health hazards.

Many techniques have been developed for the removal of dyes from wastewater⁷ such as photodegradation^{8,9}, chemical oxidation¹⁰ and adsorption^{11,12}. Among them adsorption techniques have been identified as cheap and efficient treatment of wastewater at scale without the use of any harmful chemical or production of side products¹³.

Biochar is a carbonaceous material prepared by the pyrolysis of biomass in limited supply of oxygen¹⁴. The properties of biochar heavily depend on the biomass, the resident time, resident temperature, heating rate as well as chemical or physical modification to the surface¹⁵⁻²⁰. The properties of biochar can be modified by proper control of each parameter, and it can be used for various applications^{13,21,22}.

Biochar has been successfully used for the removal of organic as well as inorganic contaminants^{11,12,23,24}. It has been used for the removal of dyes such as methylene blue²⁵, Congo red²⁶. Several studies have been done for the removal of crystal violet using biochar prepared using palm petioles²⁷, kernel shell²⁸, coconut husk²⁹, walnut shell³⁰, *Gliricidia sepium*³¹, banana stem³² and sugarcane bagasse³³. Coconut shell is an agricultural waste which is low cost, readily available biomass^{34,35}. Biochar made from coconut shell has been used for the removal of dyes such as methylene blue^{36,37}, Reactive Orange 16³⁸, Basic Red 09³⁹. Most of these biomaterials exhibit varying adsorption capacities, making them valuable tools for treating dye-contaminated wastewater. Researchers continue to explore their potential and optimize their performance for sustainable environmental solutions.

As research lacks on the adsorption of crystal violet onto coconut shell biochar our objective is to prepare biochar from coconut shell at different temperatures and investigate its potential for removal of crystal violet from its aqueous solution. The factors such as resident temperature, concentration, dosage was optimized, for adsorption isotherm and kinetics studies.

Experimental

Materials: Coconut shell was procured from local market, dried in sunlight for one week and ground to a powder in a domestic mixer grinder, followed by screening through a one mm

mesh. Crystal violet (C.I. No = 42555) was procured from SD fine Chem limited India. A 500 ug/ml stock solution was prepared by dissolving 500 mg of crystal violet in 1000 mL of distilled water.

Biochar Preparation: Powdered coconut shell was pyrolyzed in a steel container at four different temperatures, 400 °C, 500 °C, 600 °C, 700 °C for half an hour. Three samples of biochar at each temperature were prepared and stored separately. The percentage yield of the biochar was calculated using Eq. (1) ⁴⁰:

$$\%Yield = \frac{m_{bc}}{m_{bm}} \times 100 \#(1)$$

Where, m_{bc} is the weight of the biochar and m_{bm} is the weight of the biomass before pyrolysis.

Proximate Analysis: For pH determination, biochar was mixed with distilled water in a ratio of 1:20 and kept for 24 hours after which the pH was measured⁴¹. For Ash Content ASTM D3174 was used ^{41,42}.

Characterization : To determine the functional groups on the biochar samples, FTIR of all the four biochar samples was done. Further, SEM and XRD analysis of biochar having the maximum adsorption capacity was carried out.

Adsorption Studies: Batch adsorption studies were carried out to determine the amount of crystal violet adsorbed onto the biochar. After each adsorption study the solution was filtered through a Whatmann filter paper no 41, followed by measuring the absorption of the solution on a JASCO V-620 UV-Vis spectrometer at 590 nm. A linear calibration curve was used to determine the concentration of the crystal violet in the solution. The percentage removal was calculated using Eq. (2) ⁴³:

$$\%Removal = \frac{(C_i - C_t)}{(C_i)} \times 100 \#(2)$$

Where, C_t Is the final concentration, C_i is the initial concentration.

Adsorption capacity was calculated using Eq. (3) ⁴³:

$$Q = \frac{x}{M} \#(3)$$

Where, Q represents the adsorption capacity in mg.g^{-1} . x represents the mass of the adsorbate adsorbed in mg. M represents the mass in grams of the biochar.

Performance evaluation of biochar samples: To evaluate the performance of each biochar sample, adsorption capacity of each sample was determined. 250 mg of each biochar sample

was shaken on an orbital shaker for 2 hours with 100 mL of 10 ppm crystal violet solution in a 250 mL conical flask. This process was done in triplicate.

Optimization of parameters: Response surface methodology (RSM), a multivariate statistical technique was used for optimization of the two parameters, concentration of the dye and dosage of biochar^{44,45}. A central composite design (CCD) was used to decide the number of experiments. Ten experiments were performed with the adsorption capacity and percentage removal as two response variables.

Adsorption Kinetics and Isotherm: To determine the mechanism and kinetics of the adsorption, the study was performed in two steps:

Isotherm Fitting: 250 mg of biochar was added in eight different conical flasks. To each flask 100 ml of 1, 5, 10, 20, 50 100, 250, 500 ppm of crystal violet was added and shaken on an orbital shaker for 2 hours, the results obtained from this experiment was used to perform the isotherm fitting.

Kinetic Experiment: 250 mg of biochar was added in seven different conical flasks. To each flask 100 ml of 10 ppm crystal violet solution was added. All the flasks were shaken on an orbital shaker for 2, 5, 10, 20, 40, 70 and 100 min. The solution was filtered through a Whatman filter paper no 41, followed by measuring the absorbance of the solution on a JASCO V-620 UV-Vis spectrometer at 590 nm.

Statistical Analysis and Model Fitting: Analysis of Variance (ANOVA) was performed using Minitab 21, with $p < 0.05$ signifying statistical significance. Response Surface Methodology was performed using Design Expert 13 and model fitting was performed using Origin Pro 2021.

Result and Discussion

Biochar Preparation: The results from the yield are given in Table 1. The difference in yields of biochar produced at different temperatures showed a statistically significant difference ($p < 0.05$). Each pair, student's t-test showed that, there was a statistically significant difference in the yields of biochar except that produced at 600 °C and 700 °C (Fig. 1). There is a decrease in yield with an increase in temperature of pyrolysis. The decrease in yield could be attributed to decomposition of lignin, which occurs at a higher temperature than that of hemicellulose, enhancing properties such as surface area and pore size^{46,47}. Furthermore, no appreciable change in yield was observed beyond 600 °C. At temperatures about 550 °C the fixed carbon reaches a steady state and there is little to no decrease in yield⁴⁸.

Proximate Analysis: The pH and ash content (Table 1) of all the biochar samples were statistically different from each other ($p > 0.05$), suggesting that there is a change in ash content and pH as the pyrolysis temperature changes. It is observed that with an increase in pyrolysis temperature the ash content of biochar is increasing, which may be attributed to the increased concentration of inorganic matter after volatilization of organic matter⁴⁰. A similar trend can be seen in pH, as the temperature increases the pH of the biochar increases. This could be attributed to the increase in alkaline salts and reduction of acidic functional groups^{19,49}.

Characterization: Biochar like other agricultural biomass is typically made up of cellulose, hemicellulose and lignin⁵⁰. Fig. 3 shows the FTIR spectra of CS400, CS500, CS600 and CS700 biochar. A considerable broad O-H stretching at around 3384 cm^{-1} , a prominent C-H stretching at 2950 cm^{-1} , aromatic C=O and C=C was observed at about 1698 cm^{-1} ⁴⁴. A C-O-C lignin stretching was observed at 1243 cm^{-1} ⁴⁰ and a C-O-C cellulose/hemicellulose (holocellulose) stretching was observed at 1049 cm^{-1} ⁴⁰. A peak at 870 cm^{-1} corresponds to O-Si stretching, due to presence of silicates in biochar⁵¹. It is observed that as the temperature increases, there was a reduction in oxygen containing functional groups. This is due the thermal decomposition of lignin, cellulose and hemicellulose⁵². A relative increase of silicate functional group was also observed, this could be attributed to the ash present in the biochar and high thermal stability of silicates in biochar.

As CS700 biochar showed the best removal capacity among all the prepared biochar, it was selected for SEM and XRD characterization. Fig. 4 shows the Scanning Electron Microscopy (SEM) images of CS700 before and after adsorption of crystal violet. At a magnification of 5k the smooth, well organised, porous, carbonaceous cellular framework of coconut shell can be clearly seen⁴³. Comparison of images before and after adsorption suggest the deposition of crystal violet on the biochar and the available pores were fully occupied.

The X-ray diffraction (XRD) pattern was collected on an X-ray diffraction (XRD) spectroscopy with Cu K α radiation ($\lambda = 1.5405\text{ \AA}$) over the angular range $10^\circ \leq 2\theta \leq 70^\circ$, operating at 40 kV and 30 mA. Fig. 5 shows the XRD patterns of biochar before and after adsorption of crystal violet. A broad low intensity peak at about 23° was observed, which could be due to the presence of crystalline carbon present in the structure, mostly cellulose⁵³. This is in good agreement with the XRD pattern reported previously⁵⁴. The XRD pattern confirms that the prepared biochar was mostly amorphous in nature⁵⁴.

Performance evaluation of biochar samples: As seen in Fig. 6 increase in the pyrolysis temperature increased the adsorption capacity, gradually with temperature. The biochar

prepared at 700 °C showed the highest average adsorption capacity with the lowest standard deviation. The increase in adsorption could be attributed to the increased surface area, high porosity and surface morphological changes^{19,55}. Therefore, the biochar prepared at 700 °C was selected to perform further studies.

Response Surface Methodology: According to the given design (Table 2), ten experimental runs were conducted.

The results were then analysed using the analysis control and a summary of fit of all the models are given in Table 3. In case of the adsorption capacity, a linear model was suggested with a sequential p-value of 0.0011 and Adjusted R² to 0.8152. Thus, this model was selected for further analysis. For the removal capacity, both the linear and quadratic models were suggested but as the adjusted R² of the quadratic model was higher the quadratic model was selected whereas the terms in the cubic models were aliased due to low factor count, they were ignored.

The equations for the adsorption capacity (Y₁) and Percentage Removal (Y₂) are given as Eq. (4) and Eq. (5):

$$Y_1 = 5.9964 - 0.0155 X_1 + 0.14513 X_2 \quad \#(4) \#\#\#\#\#$$

$$Y_2 = 66.5279 + 0.0438 X_1 - 2.3224 X_2 + 0.00237 X_1 X_2 - 0.00012 X_1^2 + 0.02002 X_2^2 \quad \#\#(5)$$

The selected models were then used for numerical optimization, with the default options and a dosage value of 210 mg and concentration of 12 ppm was obtained, with an overall desirability of 0.693, the contour plots of all the factors are given in Fig. 7.

Adsorption Isotherms: A non-linear Langmuir and Freundlich isotherms were fitted, to understand the mechanisms of adsorption of the crystal violet onto the surface of biochar.

The Langmuir adsorption isotherm assumes that the adsorption occurs on a monolayer, and once the sites have been occupied no further adsorption occurs⁴.

The Freundlich isotherm assumes that the adsorption occurs on heterogeneous surface⁴.

The Langmuir equation is given as Eq. (6)^{4,56}:

$$Q_e = \frac{K_a Q_{max} C_e}{1 + K_a C_e} \quad \#(6)$$

And the Freundlich isotherm is given as Eq. (7)^{4,56}:

$$Q_e = K_f C_e^{1/n} \quad \#(7)$$

Where, K_a is the Langmuir isotherm constant and Q_{max} (mg.g^{-1}) is the maximum adsorption capacity. Q_e (mg.g^{-1}) is the amount of adsorbate on the surface of the adsorbent at equilibrium and C_e is the concentration of the solution (mg.L^{-1}). K_f is the Freundlich isotherm constant, and n (Freundlich exponent) is an indicator of intensity change during adsorption process. The results of the fits are given in table .

As the Freundlich model showed a better fit ($R^2=0.99$) this indicates that a multilayer adsorption process, and the adsorption occurs on heterogeneous sites⁴³, this is similar to previous work^{4,29,43}. The maximum adsorption capacity calculated from the Langmuir adsorption isotherm of 124.5 mg.g^{-1} showed an excellent removal capacity for crystal violet.

Adsorption Kinetics: The results from kinetics experiments were used to fit, a non-linear Pseudo-first-order (PFO) and Pseudo-second-order (PSO) kinetics modes, to understand the rate and the order of the reaction. The PFO model equation is given as Eq. (8)⁵⁷:

$$Q_t = Q_e(1 - e^{(-k_1 \times t)}) \#(8)$$

The PSO model equation is given as Eq. (9)⁵⁷:

$$Q_t = \frac{Q_e^2 k_2 t}{1 + Q_e^2 k_2 t} \#(9)$$

Where Q_e and Q_t (mg.g^{-1}) are adsorption capacity at equilibrium and t time (h), respectively, k_1 (min^{-1}) and k_2 ($\text{g.mg}^{-1} \cdot \text{min}^{-1}$) are the constants for pseudo-first and pseudo-second order models, respectively. The results of the fitting parameters are given in Table .

The PSO model was a good fit for the adsorption of crystal violet onto the surface of biochar showing that the adsorption follows a second order kinetics process with a rate constant of $0.24153 \text{ (g.mg}^{-1} \cdot \text{min}^{-1})$. As seen in Fig. 9 90 % adsorption occurred during the first few minutes of the adsorption process showing that the adsorption process is a kinetically favourable process⁵⁸. The PSO model confirms chemisorption as the rate-limiting step caused by the involvement of physicochemical interactions between the two phases⁵⁹. This is in agreement with previous studies^{4,29,43}.

Comparison of biochar: A summary of various biomass materials used to prepare biochar for the removal of dyes from aqueous solutions is given in Table 6. Biochar prepared from coconut shell has a moderate adsorption capacity as compared to other types of biochar. Modification of biochar properties is possible with techniques such as chemical and physical modification^{18,36}, but this adds further cost and complexity for preparation of biochar from a relatively low-cost biomass⁶⁰.

Conclusion

Biochar prepared from coconut shell powder was tested for its potential for removal of crystal violet from simulated water samples. Biochar prepared at a temperature of 700 °C showed the best adsorption capacity among all the prepared biochar for crystal violet. The results from the FTIR analysis showed that as the temperature increased, the oxygen functional group decreased. SEM analysis showed that the prepared biochar had a well-organized porous structure. The XRD pattern showed that the biochar was mostly amorphous in nature, with no crystalline inorganic contaminant. The crystal violet mostly adsorbed into the mesoporous structures of the biochar. Optimization of dosage and concentration was performed using CCD and yielded a dosage of 210 mg and 12 ppm, with desirability of 0.693. The results from the optimization can be for future studies using crystal violet and coconut shell biochar. The maximum removal capacity Q_{\max} was found to be 124.5 mg.g⁻¹ and the adsorption followed a second order kinetic with a rate constant of 0.241 g.mg⁻¹.min⁻¹. Thus, biochar prepared from coconut shell can be used as a low cost, sustainable solution for removal of emerging pollutants such as crystal violet and other dyes.

Acknowledgements and funding statements

Acknowledgements: The author would like to thank Dr Abhay Sinh Salunke for his continuous help and support during the preparation of this work. The authors would also like to thank

Dr P A Hassan, BARC for providing support for this project.

Figures:

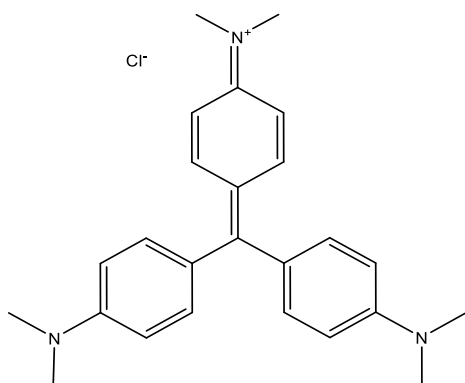


Fig. 1: Structure of crystal violet.

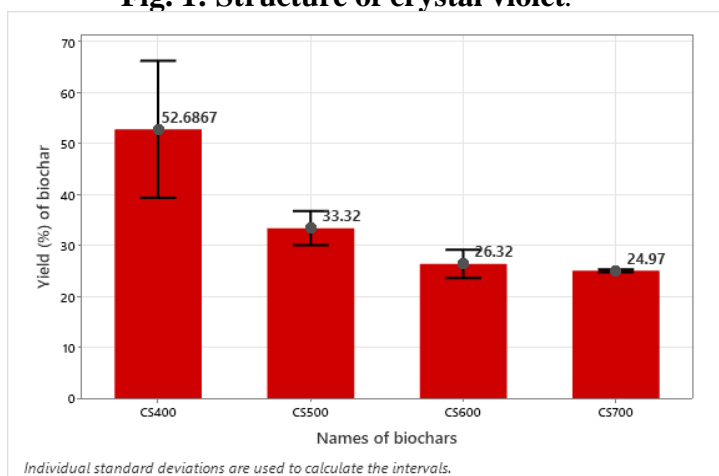


Fig. 2: Bar graph showing the yield of biochar at various temperature.

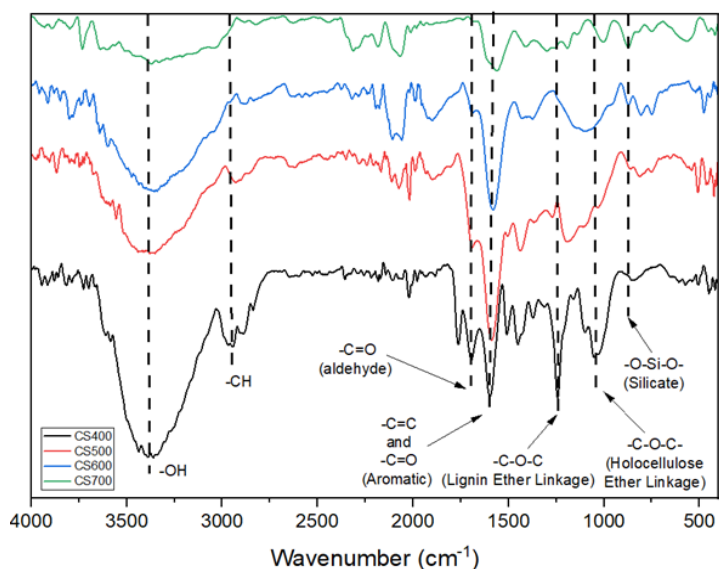


Fig. 3: FTIR spectra of CS400, CS500, CS600, CS700

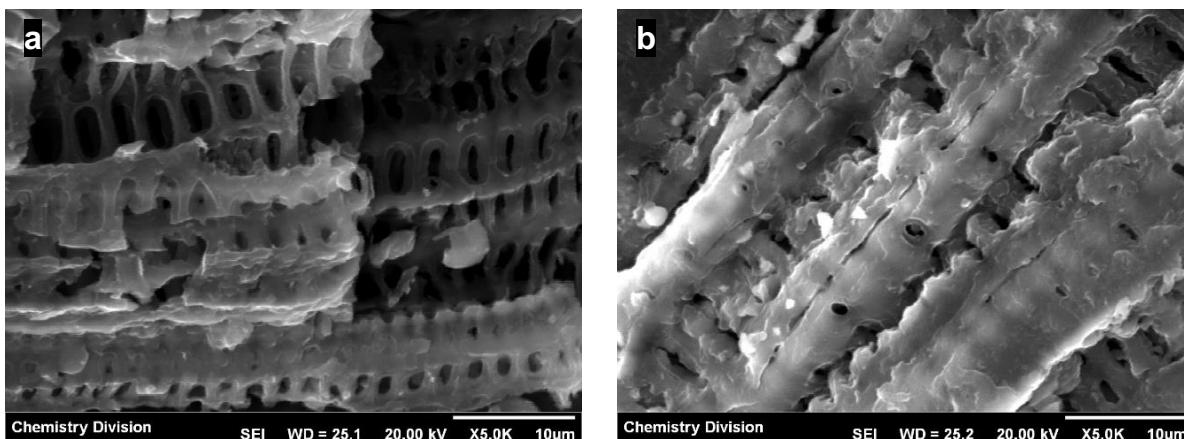


Fig. 4: SEM images of CS700 (a) before and (b) after adsorption.

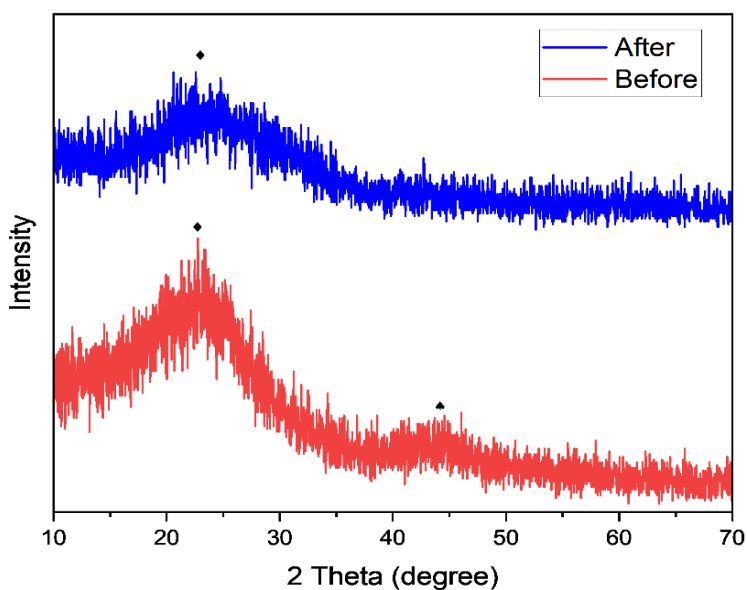


Fig. 5: XRD pattern of CS700 before and after adsorption.

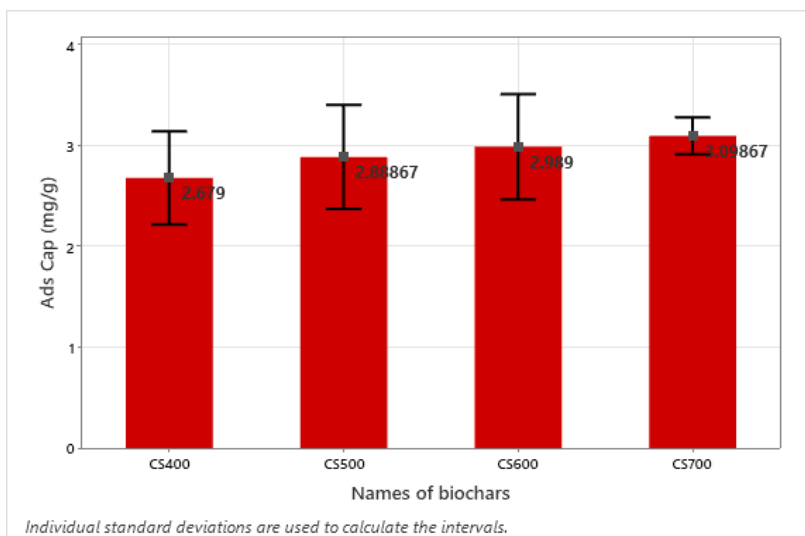


Fig. 6 : Plots of Adsorption Capacity of CS400, CS500, CS600, CS700.

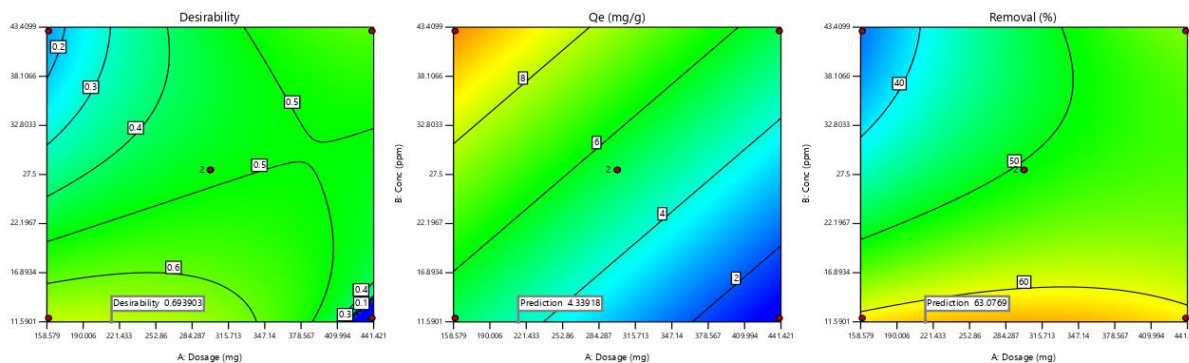


Fig.7: Contour Plot of Optimized results.

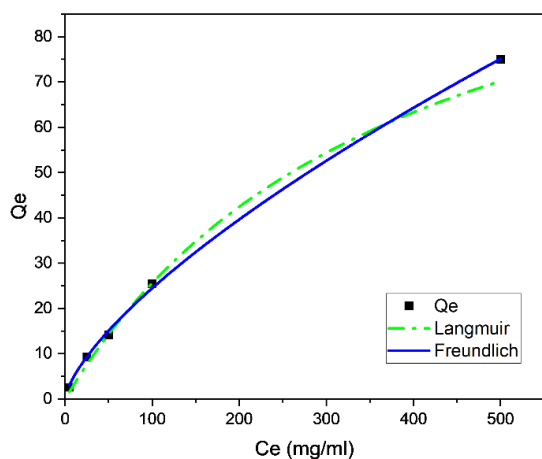


Fig. 8: Adsorption isotherms of crystal violet.

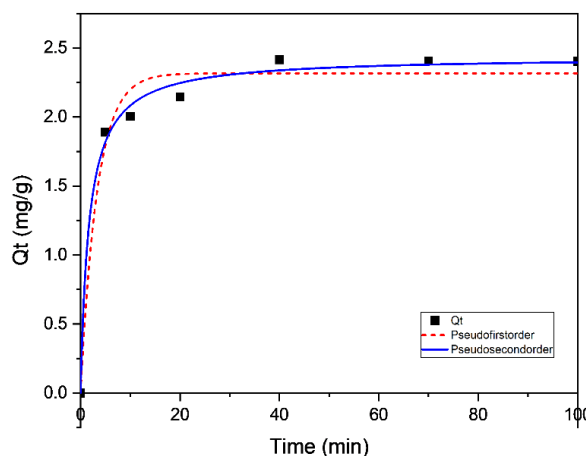


Fig. 9: Adsorption kinetics of crystal violet onto biochar.

Tables:

Table 1: The yield, Ash Content and pH of biochar derived from coconut shell, at four pyrolysis temperatures ranging from 400 °C to 600 °C.

Label	Percentage Yield	Ash Content	pH
CS400	52.68±5.41 ^a	1.58±0.02 ^a	7.68±0.16 ^a
CS500	33.32±1.35 ^b	1.88±0.04 ^b	8.01±0.13 ^b
CS600	26.32±1.12 ^c	2.23±0.02 ^c	8.31±0.05 ^c
CS700	24.97±0.10 ^c	2.82±0.00 ^d	8.77±0.01 ^d

Mean ± Standard deviation; The different letters following the figures indicate significant differences ($p < 0.05$).

Table 2: Experimental Design and Variables of CCD

Std Order	Run Order	X1	X2	Qe (mg.g ⁻¹)	Removal (%)
8	1	300	50	9.21091	55.2654
7	2	300	5	1.1784	70.704
5	3	100	28	11.1173	39.7045
10	4	300	28	4.90239	52.5256
9	5	300	28	4.54942	48.7438
6	6	500	28	3.13807	56.037
3	7	160	43	8.15145	30.331
1	8	160	12	4.64264	61.9019
4	9	440	43	4.9118	50.2603
2	10	440	12	1.67117	61.2763

Table 3: Summary of fits of Linear, 2 factor interaction, quadratic and cubic models for (a) Adsorption capacity and (b) Percentage removal.

(a) Fits summary of Adsorption Capacity					
Source	Sequential p-value	Lack of Fit p-value	Adjusted R ²	Predicted R ²	
Linear	0.0011	0.1273	0.8152	0.6707	Suggested
2FI	0.9109	0.1155	0.7848	0.5279	
Quadratic	0.4261	0.1073	0.7893	0.3448	
Cubic	0.3879	0.0865	0.8366	-1.2978	Aliased
(b) Fits summary of Removal Capacity					
Source	Sequential p-value	Lack of Fit p-value	Adjusted R ²	Predicted R ²	
Linear	0.0319	0.2352	0.5197	0.1281	Suggested
2FI	0.2193	0.2441	0.5734	0.2109	
Quadratic	0.0966	0.3280	0.8011	0.3952	Suggested
Cubic	0.4583	0.2516	0.8177	-1.2455	Aliased

Table 4: Fitted Parameters of the Langmuir and Freundlich isotherms.

Isotherm	Parameters		R ²
Langmuir	Q _{max} (mg.g ⁻¹)	K _a (L.mg ⁻¹)	0.97
	124.5	0.00234	
Freundlich	K _f	n	0.99
	0.9308	1.40955	

Table 5: Kinetics Model parameters of PFO and PSO kinetics model

Model	Parameters		R ²
PFO	Q _e (mg.g ⁻¹)	k ₁ (min ⁻¹)	0.97
	2.31631	0.29808	
PSO	Q _e (mg.g ⁻¹)	k ₂ (g.mg ⁻¹ .min ⁻¹)	0.99
	2.43695	0.24153	

Table 6: Comparison of various biochar in literature

Biomass	Adsorbate	Maximum Adsorption Capacity (mg.g ⁻¹)	Ref
Palm petioles	Crystal violet	209	27
Gliricidia sepium		125.53	31
Palm Kernal Shell		25.45	28
Banana Stem		153.50	32
Coconut Shell	Methylene Blue	200.01	36
		8.612	37
	Reactive Orange 16	106.60	38
	Basic Red 09	65.24	39
Coconut Shell	Crystal violet	124.5	this study

References

1. R. Al-Tohamy, S. S. Ali, F. Li, K. M. Okasha, Y. A. G. Mahmoud, T. Elsamahy, H. Jiao, Y. Fu, and J. Sun, *Ecotoxicol Environ Saf*, 231, 113160, 2022.
2. B. Lellis, C. Z. Fávoro-Polonio, J. A. Pamphile, and J. C. Polonio, *Biotechnology Research and Innovation*, 3, 275, 2019.
3. M. Saji, S. Taguchi, K. Uchiyama, E. Osono, N. Hayama, and H. Ohkuni, *J Hosp Infect*, 31, 225, 1995.
4. A. Mittal, J. Mittal, A. Malviya, D. Kaur, and V. K. Gupta, *J Colloid Interface Sci*, 343, 463, 2010.
5. S. Mani and R. N. Bharagava, *Rev Environ Contam Toxicol*, 237, 71, 2016.
6. <https://www.norman-network.net/?q=node/19> accessed: 22-04-2024
7. M. T. Amin, A. A. Alazba, and U. Manzoor, *Advances in Materials Science and Engineering*, 2014, 1, 2014.
8. N. Welter, J. Leichtweis, S. Silvestri, P. I. Z. Sánchez, A. C. C. Mejía, and E. Carissimi, *J Alloys Compd*, 901, 163758, 2022.
9. N. P. F. Gonçalves, M. A. O. Lourenço, S. R. Baleuri, S. Bianco, P. Jagdale, and P. Calza, *J Environ Chem Eng*, 10, 107256, 2022.
10. X. Li, Y. Jia, M. Zhou, X. Su, and J. Sun, *J Hazard Mater*, 397, 122764, 2020.
11. R. Guo, L. Yan, P. Rao, R. Wang, and X. Guo, *Environmental Pollution*, 258 2020.
12. E. Baldikova, K. Pospiskova, and I. Safarik, *Chem Eng Technol*, 43, 168, 2020.
13. F. L. Braghiroli, H. Bouafif, C. M. Neculita, and A. Koubaa, *Water Air Soil Pollut*, 229 2018.
14. X. Tan, Y. Liu, G. Zeng, X. Wang, X. Hu, Y. Gu, and Z. Yang, *Chemosphere*, 125, 70, 2015.
15. J. A. Ippolito, L. Cui, C. Kammann, N. Wrage-Mönnig, J. M. Estavillo, T. Fuertes-Mendizabal, M. L. Cayuela, G. Sigua, J. Novak, K. Spokas, and N. Borchard, *Biochar*, 2, 421, 2020.
16. E. Thomas, N. Borchard, C. Sarmiento, R. Atkinson, and B. Ladd, *Biochar*, 2, 151, 2020.

17. J. S. Cha, S. H. Park, S.-C. Jung, C. Ryu, J.-K. Jeon, M.-C. Shin, and Y.-K. Park, *Journal of Industrial and Engineering Chemistry*, 40, 1, 2016.
18. L. Wang, Y. S. Ok, D. C. W. Tsang, D. S. Alessi, J. Rinklebe, O. Mašek, N. S. Bolan, and D. Hou, *Soil Use Manag*, 38, 14, 2022.
19. S. Li, S. Harris, A. Anandhi, and G. Chen, *J Clean Prod*, 215, 890, 2019.
20. P. R. Yaashikaa, P. S. Kumar, S. Varjani, and A. Saravanan, *Biotechnology Reports*, 28, e00570, 2020.
21. C. Wang, D. Luo, X. Zhang, R. Huang, Y. Cao, G. Liu, Y. Zhang, and H. Wang, *Environmental Science and Ecotechnology*, 10, 100167, 2022.
22. M. Ahmad, A. U. Rajapaksha, J. E. Lim, M. Zhang, N. Bolan, D. Mohan, M. Vithanage, S. S. Lee, and Y. S. Ok, *Chemosphere* 99, 19, 2014.
23. Y. Yao, B. Gao, M. Inyang, A. R. Zimmerman, X. Cao, P. Pullammanappallil, and L. Yang, *J Hazard Mater*, 190, 501, 2011.
24. P. Wijeyawardana, N. Nanayakkara, C. Gunasekara, A. Karunarathna, D. Law, and B. K. Pramanik, *Environ Technol Innov*, 28 2022.
25. Y. Mu, H. Du, W. He, and H. Ma, *Diam Relat Mater*, 121, 108795, 2022.
26. S. Kaur, S. Rani, and R. K. Mahajan, *J Chem*, 2013, 1, 2013.
27. H.-O. Chahinez, O. Abdelkader, Y. Leila, and H. N. Tran, *Environ Technol Innov*, 19, 100872, 2020.
28. P. P. Kyi, J. O. Quansah, C.-G. Lee, J.-K. Moon, and S.-J. Park, *Applied Sciences*, 10, 2251, 2020.
29. A. M. Aljeboree, A. F. Alkaim, and A. H. Al-Dujaili, *Desalination Water Treat*, 53, 3656, 2015.
30. Y. Shkliarenko, V. Halysh, and A. Nesterenko, *Water (Basel)*, 15, 1536, 2023.
31. A. W. Indika and H. M. C. M. I. Meththika Vithanage, *Environ Geochem Health*, 41 2017.
32. S. K. Jadhav and S. R. Thorat, *Oriental Journal Of Chemistry*, 38, 475, 2022.
33. F. M. Jais, S. Ibrahim, C. Y. Chee, and Z. Ismail, *Sustain Chem Pharm*, 24 2021.

34. K. Harshwardhan and K. Upadhyay, *Journal of Fundamentals of Renewable Energy and Applications*, 07 2017.
35. W. L. Bradley and S. Conroy, *E3S Web of Conferences*, 130, 01034, 2019.
36. M. A. Islam, M. J. Ahmed, W. A. Khanday, M. Asif, and B. H. Hameed, *J Environ Manage*, 203, 237, 2017.
37. P. T. Le, H. T. Bui, D. N. Le, T. H. Nguyen, L. A. Pham, H. N. Nguyen, Q. S. Nguyen, T. P. Nguyen, N. T. Bich, T. T. Duong, M. Herrmann, S. Ouillon, and T. P. Q. Le, *Adsorption Science and Technology*, 2021 2021.
38. R. Muralikrishnan and C. Jodhi, *ChemistrySelect*, 5, 7734, 2020.
39. P. Saravanan, B. P. Thillainayagam, G. Ravindiran, and J. Josephraj, *Energy Sources, Part A: Recovery, Utilization, and Environmental Effects*, 2020.
40. S.-X. Zhao, N. Ta, and X.-D. Wang, *Energies (Basel)*, 10, 1293, 2017.
41. D. Angin, *Bioresour Technol*, 128, 593, 2013.
42. ASTM International, D3174 Standard Test Method for Ash in the Analysis Sample of Coal and Coke from Coal 2018.
43. J. Missau, D. A. Bertuol, and E. H. Tanabe, *Appl Clay Sci*, 214, 106297, 2021.
44. R. Zhou, M. Zhang, J. Zhou, and J. Wang, *Sci Rep*, 9 2019.
45. R. Zhou, M. Zhang, J. Li, and W. Zhao, *J Environ Chem Eng*, 8, 104198, 2020.
46. S. Li and G. Chen, *Waste Management*, 78, 198, 2018.
47. F. Amalina, A. Syukor Abd Razak, S. Krishnan, H. Sulaiman, A. W. Zularisam, and M. Nasrullah, *Cleaner Materials*, 6, 100137, 2022.
48. J. Yu, M. Song, and Z. Li, *Green Processing and Synthesis*, 11, 423, 2022.
49. A. Tomczyk, Z. Sokołowska, and P. Boguta, *Rev Environ Sci Biotechnol*, 19, 191, 2020.
50. Q. Wang and J. Sarkar, *International Journal of Energy Production and Management*, 3, 34, 2018.
51. R. Choudhary, S. Koppala, and S. Swamiappan, *Journal of Asian Ceramic Societies*, 3, 173, 2015.

52. M. Behrens, J. S. Cross, H. Akasaka, and N. Ohtake, *Biomass Bioenergy*, 122, 290, 2019.
53. D. Ciolacu, F. Ciolacu, and V. I. Popa, *Cellulose Chem. Technol*, 45, 13, 2011.
54. M. L. Yeboah, X. Li, and S. Zhou, *Materials 2020, Vol. 13, Page 625*, 13, 625, 2020.
55. S. Li, V. Barreto, R. Li, G. Chen, and Y. P. Hsieh, *J Anal Appl Pyrolysis*, 133, 136, 2018.
56. R. Zhou, Y. Wang, M. Zhang, P. X. Yu, and J. Li, *Environ Monit Assess*, 191 2019.
57. T. Chen, L. Luo, S. Deng, G. Shi, S. Zhang, Y. Zhang, O. Deng, L. Wang, J. Zhang, and L. Wei, *Bioresour Technol*, 267, 431, 2018.
58. E. D. Revellame, D. L. Fortela, W. Sharp, R. Hernandez, and M. E. Zappi, *Clean Eng Technol*, 1, 100032, 2020.
59. D. Pandey, A. Daverey, K. Dutta, V. K. Yata, and K. Arunachalam, *Environ Technol Innov*, 25, 102200, 2022.
60. T. Józwiak, U. Filipkowska, P. Bugajska, and T. Kalkowski, *Journal of Ecological Engineering*, 19, 129, 2018.